The Pennsylvania State University

The Graduate School

Department or Mechanical and Nuclear Engineering

MODELING OF LARGE-FORMAT LI-ION CELL

PERFORMANCE AND SAFETY

A Dissertation in

Mechanical Engineering

by

Wei Zhao

Submitted in Partial Fulfillment
of the Requirements
for the Degree of

Doctor of Philosophy

May 2014

The dissertation of Wei Zhao was reviewed and approved* by the following:

Chao-Yang Wang
William E. Diefenderfer Chair of Mechanical Engineering
Dissertation Advisor
Chair of Committee

Michael Hickner
Associate Professor of Materials Science and Engineering

Chris Rahn
Professor of Mechanical Engineering

Donghai Wang
Assistant Professor of Mechanical Engineering

Daniel Haworth
Professor of Mechanical Engineering
Chair of Graduate Program

*Signatures are on file in the Graduate School

ABSTRACT

Small Li-ion batteries have been widely used for consumer electronics due to their high power and energy density. Large-format Li-ion batteries are believed to be essential for vehicle- and grid- energy storage enabling a sustainable energy future. Today, scale-up of Li-ion cells has not maximized the potential of available battery materials, leading to much lower energy density than their coin cell benchmarks. How to unlock the potential of existing Li battery materials and scale up Li-ion cells to 10-100 Ah sizes without substantially lowering the cell's energy density remains a key technological challenge.

Safety has become another pressing issue with the increasing interest in large-format Li-ion batteries for automotive applications due to the high energy density of Li-ion batteries and wide-ranging working conditions for electric vehicles compared with electronic applications. The highest specific energy available in today's commercial Li-ion rechargeable batteries is approximately 240 Wh/kg, almost 20% of the energy content of TNT at 4.61 MJ/kg. The release of the battery energy in an abnormal way could cause catastrophic consequences. Large-format Li-ion batteries are particularly vulnerable to abusive conditions because of their higher energy content.

Experimental study of large-format Li-ion batteries performance and safety is more expensive and dangerous to perform than that of small batteries, making modeling a valuable tool for this purpose. In this work, a 3D, multiscale and electrochemical-thermal coupled model is introduced to study the performance and safety issues uniquely presented in large-format Li-ion cells. Firstly, we study the scale-up of Li-ion cells from

coin cells to large-format cells. We show that significant performance penalty can be caused in large-format spirally wound cells if only one single pair of tabs is used for current collecting. The reason for the inferior performance is due to the in-plane electrons transport loss in the long current collector foils and non-uniform active material utilization. An effective design to mitigate the performance loss in large-format cells is to use multiple tabs minimizing the voltage loss and increasing the active material utilization uniformity. The effect of tab number and location is investigated using the 3D modeling tool. A quantitative relationship between the cell's useable energy density and the current density non-uniformity is established, for the first time, in the literature. Secondly, we use the 3D electrochemical-thermal coupled model to study the full nail penetration process of a large format cell. It is found that the thermal response of cell is closely coupled with its electrochemical performance after penetration. Two heating regimes, namely global heating and local heating are identified. The effect of various parameters such as shorting contact resistance, nail diameter, nail thermal conductivity, cell capacity, etc. is investigated using modeling. Finally, we use the model to study the internal short-circuit of a large-format Li-ion cell by a metal particle. Compared with nail penetration, tab heating becomes an important mechanism in internal short-circuit. The cell electrochemical and thermal behavior changes significantly with the metal particle size and shorting resistance. The model results provide explanations for the poor reproducibility of the present nail penetration and internal short-circuit experimental methods.

TABLE OF CONTENTS

LIST OF FIGURES

LIST OF TABLES

NOMENCLATURE

A total active area, cm^2

A_{tab} tab cross sectional area, cm^2

a_s specific active surface area for an electrode, cm^2/cm^3

C nominal cell capacity, Ah

c lithium concentration in phase, mol/cm^3

D diffusion coefficient of lithium species, cm^2/s

F faraday's constant, 96487 C/mol

$f_{\pm}$ mean molar activity coefficient of the electrolyte

I_{app} applied discharge current, A

i_0 exchange current density, A/cm^2

$iSOC$ local state of charge

j volumetric reaction current, A/cm^3

k rate constant for an electrode reaction

L length of the electrode, cm

R universal gas constant, 8.3143 J/mol K

r radial coordinate across a spherical particle, cm

SOC state of charge

T temperature, K

t time, s

t_+^0 transference number of lithium ion

U	equilibrium potential of an electrode reaction, V
W	width of the electrode, cm
x	coordinate along the electrode thickness, cm
y	coordinate along the electrode width, cm
z	coordinate along the electrode length, cm

Greek

α_a	anodic transfer coefficient
α_c	cathodic transfer coefficient
ε	volume fraction of a phase
ε_I	error of charge of balance
η	surface overpotential of an electrode reaction, V
κ	ionic conductivity of electrolyte, S/cm
κ_D	diffusional conductivity, A/cm
σ	electronic conductivity of an electrode, S/cm
$\sigma(\tau)$	instantaneous standard deviation of current density distribution, A/cm^2
$\bar{\sigma}$	time-averaged standard deviation of current density distribution, A/cm^2
ϕ	electrical potential in a phase, V

Subscripts

0	initial value
a	anode
c	cathode
e	electrolyte phase
s	solid phase

Superscripts

eff	effective
Li	lithium species

ACKNOWLEDGEMENTS

Chapter 1

Introduction

1.1 Li-ion rechargeable battery fundamentals

Rechargeable lithium-ion (Li-ion) batteries involve cells that employ lithium intercalation compounds as the positive and negative electrode materials. During the discharge/charge process, lithium ions exchange between the two electrodes through the electrolyte, accompanied by a reduction/oxidation (redox) reaction of the host materials. The electrons flow through the external circuit, generating/absorbing power during discharge/charge.

The positive electrode material is typically a metal oxide with a layered structure, such as lithium cobalt oxide ($LiCoO_2$), or a material with a tunneled structure, such as lithium manganese oxide ($LiMn_2O_4$). The negative electrode material is typically a graphitic carbon with a layered structure [1]. The negative and positive materials, together with some necessary binders and addictive materials, are coated on copper current collector and aluminum current collector, respectively. A porous separator is placed in between the two electrodes and serves as an insulator for the electrons and conductor for the lithium ions.

When a Li-ion cell is charged, the lithium ions are de-intercalated from the positive material and intercalated into the negative material, as illustrated in Fig. **1-1**. The reverse happens on discharge. The electrochemical reactions occurring in the positive and negative electrodes during charge and discharge are as follows.

Positive electrode

$$Li_yMO_2 \xrightleftharpoons[Discharge]{Charge} Li_{y-x}MO_2 + xLi^+ + xe^- \qquad (1\text{-}1)$$

Negative electrode

$$Li_0C_6 + xLi^+ + xe^- \xrightleftharpoons[Discharge]{Charge} Li_xC_6 \qquad (1\text{-}2)$$
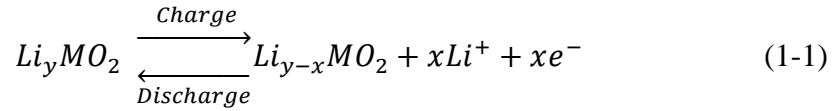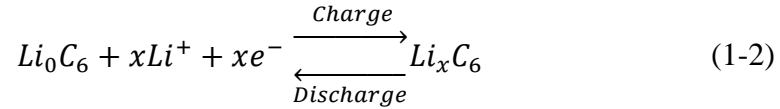
The development of secondary lithium batteries used to focus on the use of lithium metal as the negative electrode because of its high specific capacity, which is 3860 mAh/g. However, safety issues associated with lithium metal has been driving the industry to develop lithium intercalation materials instead of lithium metal. The first Li-ion batteries marketed by SONY utilized petroleum coke for the negative electrode, which has a specific capacity of 180 mAh/g [1]. Later on, graphitic materials, such as Mesocarbon Microbead (MCMB) carbon, having a higher specific capacity of 300 mAh/g, were developed and commercialized [2, 3]. More recently, a few oxides and metallic materials such as lithium titanium oxide [4, 5], and silicon [6], have also been investigated as negative hosts.

The earliest lithium metal based cells used a variety of chalcogenides(TiS_2, MoS_2, etc.) as the positive electrode material in several prototypes and commercial products. Later, manganese and vanadium oxides were utilized [7]. The discovery of lithium transition metal oxides with formula of $LiMO_2$ (M: Mn, Co and Ni) made the lithium metal batteries replaced by the lithium ion batteries, providing a step change in the approach to energy storage [8]. Almost all commercially available materials have one of two structure types. $LiCoO_2$, $LiNiO_2$ and related materials have layered structures while

$LiMn_2O_4$ materials have a three-dimensional spinel structures. However, recent years, research on other new positive electrode materials, such as $LiFePO_4$, have been promoted due to the concerns over safety and cost of lithium ion batteries. More recently, there is increasing interest in developing of Li-sulfur and Li-air batteries, which have the potential for vastly increased energy density that would satisfy the needs of large-scale energy storage applications.

Commercial lithium ion batteries typically use liquid electrolytes, which are solutions of a lithium salt in organic solvents, typically carbonates. Most Li-ion electrolytes in current use utilize $LiPF_6$ as the salt as its solution offer high ionic conductivity, $>10^{-3}$ S/cm, high lithium ion transference number (~0.35), and acceptable safety properties [1]. Some commonly used carbonates in electrolyte are ethylene carbonate (EC), dimethyl carbonate (DMC), ethyl methyl carbonate (EMC) and diethyl carbonate (DEC). Binary and ternary mixtures of these carbonates are usually used to obtain desired electrolyte properties.

The construction of a Li-ion cell consists of a positive and negative electrode, separated by a microporous polyethylene or polypropylene separator. Positive electrodes use 10 to 25 um Al foil for current collecting. Negative electrodes typically consist of 8 to 20 um Cu foils as current collectors. The positive and negative electrode sheets, together with the separator, form the electrode assembly, and the electrode assembly is wound or stacked to form a battery cell. A single or multiple pair of tabs is welded at the end of the wind of each electrode to connect the current collectors to the battery terminals. A typical cylindrical construction for small commercial cells is 18650 cell. Its construction is illustrated in Fig. **1-2**.

For specialized applications, such as satellites, stationary energy storage and electric and hybrid electric vehicles (EV/HEV), large-format cells (> 5Ah) have been developed. Large cells usually utilize prismatic configurations of either wound design or stacked-electrode design. Fig. **1-3(a)** and **1-3(b)** illustrates the two types of design for large-format Li-ion cells.

1.2 Safety mechanisms of Li-ion batteries

As the energy and power densities of Li-ion batteries become increasingly large to meet the requirement of advanced applications such as EV/HEV and grid energy storage, safety has become a primary concern as the failure of high energy/power batteries could cause catastrophic incidents. The highest specific energy available in today's commercial Li-ion rechargeable batteries is approximately 240 Wh/kg, almost 20% of the energy content of TNT at 4.61 MJ/kg **[9]**. The energy of a battery is stored in its active materials. Under normal discharge (charge), the chemical (electrical) energy is converted to electrical (chemical) energy with minimal heat generation. However, when the battery is under abusive conditions, large amount of heat could be generated due to unmanaged battery energy release or absorption. The large heat generation will trigger a series of exothermic reactions that generate more heat, eventually leading to a thermal runaway. Catastrophic consequences will usually be caused following a battery thermal runaway.

Several serious accidents that involve Li-ion batteries have gained a lot of publicity during the past several years. All these accidents were resulted from the failure of the batteries utilized, which caused fire and ultimate destruction of the whole system. In the Boeing 787 Dreamliner's first year of service, at least four aircraft suffered from

electrical system problems stemming from its Li-ion batteries. On January 7, 2013, a battery overheated and started a fire in an empty 787 operated by Japan Airlines (JAL) at Boston's Logan International Airport **[10]**. On January 16, 2013, an All Nippon Airways (ANA) 787 made an emergency landing at Takamatsu Airport on Shikoku Island after the flight crew received a computer warning that there was smoke inside one of the electrical compartments. Passengers and crew were evacuated using the emergency slides **[11]**. Although the investigators haven't been able to determine the original cause of the incidents, they believe that the fire was triggered by short-circuit of the Li-ion batteries **[12]**. Thermal runaway of the battery packs was triggered as a result of short-circuits, causing the fire of the battery packs (see Fig. **1-4 [13]**)

Several abusive conditions that cause battery accidents have been identified and studied. They include overheating, overcharge, and short-circuit. Heating tests such as Differential Scanning Calorimetry (DSC), Accelerating Rate Calorimetry (ARC) and thermal ramp test are used to characterize cell heat generation during off-normal conditions. Fig. **1-5** shows a typical cell thermal response during forced thermal ramp test **[14]**. An external source of heat is used to raise the cell temperature. Three heating stages can be identified as shown in the figure.

Overcharge can occur if the control electronics of the battery management system (BMS) malfunction. It can also occur if there is severe cell imbalance in a battery pack. The thermal response of Li-ion cells during overcharge is largely determined by the cathode chemistry **[15]**. Measurements of heat flow from the cells have shown that there is a rapid increase in heat generation when all of the lithium has been removed from the cathode (see Fig. **1-6**) **[15]**. Overcharge may also cause plating of lithium in the graphitic

anode, which not only leads to capacity loss but may also induce internal short-circuit due to the growth of lithium metal dendrite.

Among the various abusive conditions, short-circuit is the most common and most dangerous abusive condition and the cause of most field incidents involving Li-ion batteries. There are two types of short-circuit, namely external short-circuit and internal short-circuit. External short-circuit happens when the positive and negative terminals of the battery is connected with each other by an electronically conducting material with a small resistance. The battery then discharges at a very large current, resulting in large Joule heating (I^2R). Internal short-circuit, on the other hand, occurs when a current path develops within the battery cell. It is usually caused as a result of manufacture defect or physical damage to the battery cell. During internal short-circuit process, large and localized heat is generated within the cell and thermal runaway is most likely inevitable as a result. Fig. **1-7** illustrates a typical external short-circuit behavior of a 18650 Li-ion cell **[16]**. Some protection mechanisms such as separator shutdown and positive temperature coefficient device (PTC) can be effective in protecting the cell from going to thermal runaway under external short-circuits. However, these mechanisms usually fail when internal short-circuit occurs within the cells (see Fig. **1-8**).

For all the abovementioned failure modes of Li-ion cells, a common consequence is thermal runaway. Thermal runaway happens when the heat generation due to various exothermic reactions exceeds the heat dissipation, leading to rapid increase of cell temperature, which in turn triggers more exothermic reactions. The thermal runaway process can be broken down into several stages as shown in Fig. **1-9**. When the cell is heated up to around 80-100 ^{o}C, the solid electrolyte interface (SEI) layer begins to break

down resulting in low-rate heat generation [17, 18]. The breakdown of SEI layer increases the cell temperature and exposes the lithiated graphite to the electrolyte. At ~120 ^{o}C, the intercalated lithium in anode can react with the electrolyte following SEI layer breakdown [19]. Decomposition of the electrolyte begins in the 150 ^{o}C -160 ^{o}C range generating decomposition gases that result in cell venting [20]. At temperatures above ~200 ^{o}C, the cathode materials start to break down, releasing oxygen that reacts violently with the electrolyte. The high temperature and released oxygen could cause combustion of electrolyte and active materials resulting in flames, smoke and even cell explosion. Fig. **1-10** illustrates the estimated adiabatic maximum temperature rise due to each exothermic process in the cell. As can be seen, the electrical energy discharged by cell during short-circuit contributes most to the temperature rise. The electrical discharging is also the trigger of the subsequent exothermic reactions of battery material. Therefore, it is of paramount importance to study its effect on the battery safety behavior.

Evidence from investigations of field-failures involving Li-ion cells suggests that internal short-circuits are the predominant triggers to causing thermal runaway and catastrophic incidents. Therefore the following section will be focusing on the review of experimental and modeling works on internal short-circuits of Li-ion cells in the literature.

1.3 Experimental studies of Li-ion battery safety – literature review

Internal short circuit is usually caused by a manufacturing defect such as a small conductive particle wound in the jelly roll, a wrinkle in the separator, or the poor alignment of a winding [21]. It is also intrinsically more severe than other abusive

conditions. This is partially because that the protective devices in cells, battery packs and chargers cannot stop battery overheating induced by internal short circuit. Common protective devices on Li-ion cells include positive temperature coefficient of resistance (PTC), thermal and current fuse, pressure-release vent and electric circuit for protection against overcharging or forced discharge. None of these devices are able to protect the battery under internal short circuit condition. The active materials in batteries will continuously react until depletion.

Another reason for the internal short-circuit being more hazardous than other abuse conditions is that very high localized heating is generated due to current flow through the shorting conductor. This localized heat is difficult to be dissipated especially in large-format cells since it is likely to be trapped deep within the winding structure. The localized heating can easily trigger rapid temperature rising and thermal runway of batteries.

Nail penetration and crush test are two commonly adopted experimental methods for internal short-circuit test of Li-ion cells. In a nail penetration test, a nail is forced to pierce the battery at a prescribed speed, inducing a short-circuit inside the cell. Heat is generated by current flowing through the cell and by current flowing through the nail. There are not a lot of reports in the literature with regard to internal short-circuit study. Most of them focuses on cells with small capacity ($< 2Ah$). Ozawa **[22]** conducted nail penetration tests on small-scale Li-ion batteries with $LiCoO_2$ cathode and carbon anode. A sharp metal spike of 4 mm in diameter is used. The tests were performed on both fresh cells and cycled cells. The results showed that the cell temperature increased to the range of 77 ^{o}C to 105 ^{o}C and the cycled cells were safer compared with fresh cells. However, in

a more recently nail test by Wu et al. **[23]**, cells having been cycled 200 times failed to pass the test, while cells having 10 cycles had lower temperature increase during the test. Wu et al. also compared the safety performance of cells with different separators and concluded that PP separators are more vulnerable to thermal runaway due to the lack of shutting-down mechanism compared with PE and PP/PE/PP separators.

Tobishima and his coworkers did several nail penetration tests on Li-ion batteries **[21, 24]**. In **[21]** a 2.5mm diameter nail was used on commercially available prismatic Li-ion cells for internal short circuit study. The test results of standard charged cells with 835mAh capacity and slightly overcharged cells with 863 mAh capacity were compared. The result showed that overcharged cells smoked as a result of nail penetration while cell charged to the standard voltage was safe. Tobishima also studied the safety characteristics of Li-ion cells with different cathode materials in **[24]**. Cells with 500-600 mAh capacity and $LiCoO_2$ and $LiMn_2O_4$ as different cathodes were used for the nail tests. The results showed no distinct difference between these cathodes. Phosphate based cathode materials for Li-ion batteries have been pursued and recommended by some groups due to their better safety performance. Nguyen **[25]** conducted a nail penetration test on large-format battery packs, each having 3 cells connected in parallel. A nail was driven through the middle cell to induce internal short circuit. The result showed the shorted cell with cobalt based cathode quickly failed with smoke and burning and spread the thermal event to neighboring cells after one minute, while the cell with phosphate based cathode material had much lower temperature rising and did not have significant impact on the other cells. Recently, Takami **[4]** has reported a nail test on a 2-volt class Li-ion battery using lithium titanium oxide anode and cobalt oxide based cathode. It was

demonstrated that the LTO based battery was more abuse tolerant than $LiCoO_2$ based battery. The better safety performance of LTO based batteries was attributed to the lower voltage and transformation to the low electron-conductive LTO spine at shorting point to suppress the short-circuit discharge reaction.

Most of the research in literature regarding to battery safety using nail penetration test focuses on the study of material effects. Very few of them is from the battery design point of view. Maleki [26] investigated different nail penetration locations and cell capacities on the safety behavior of small Li-ion batteries for portable electronics applications. It was concluded that nail penetrated at the edge of the electrode was the least safe case because of the limited heat conduction to the cell-can. It also found that cells with large capacity are less abuse tolerant than those with smaller capacities.

Although nail penetration test is widely utilized as the method to mimicking the internal short-circuit event in Li-ion batteries, it has several limitations such as heat transfer through nails and treating equipment, gas pressure leakage and electrolyte escape [27]. The safety characteristics of batteries in a nail penetration test are also highly dependent on the nail piercing speed and depth [23, 27]. The deeper the penetration depth, the bigger the contact area and therefore the smaller the current density and heat production. This also makes the cells under high nail penetration speed more easily to pass the test.

In light of the limitation of nail penetrations test, there has been a trend of using forced internal short-circuit, such as crush test, to more accurately simulate the internal shorting event of Li-ion batteries. In a most recent version of UL 1642 standard, which is an authoritative safety testing and evaluate protocol for Li-ion batteries, the nail

penetration test is no longer described and is replaced by the crush test. In a crush test, external force is applied to a crushing apparatus, such as a round bar or two flat plates. The sample battery within the crushing apparatus is then under the applied crushing force. Depending on the crushing force and method, different anode and cathode layers may be forced to contact with each other, causing internal short-circuit. The most advantage of crust test compared with nail penetration is that the battery surface will not be damaged and the gas pressure build-up during the shorting can be maintained. An example of crush test was conducted by Santhanagopalan et al. [28] A nickel particle was inserted between different layers of Li-ion cells to create four types of short. The jelly roll after the first few initial cycles was unwound and a nickel particle sufficiently large to initiate internal short was placed in appropriate regions to create the desired type of short-circuit. The jelly roll was then crushed using a flat jig at the point where the nickel particle was inserted. The experiments showed that the shorting scenario where the cathode aluminum current collector contacts with the carbonate anode active material causes largest temperature rising. In almost all scenarios, the origin of the trouble during thermal runway was from the anode. In [26], surface indentation test and cell-pinch test were carried out and the result was compared with the nail penetration test. It was demonstrated that internal short-circuit produced by the former two methods caused more safety troubles than the nail penetration tests. Some other crush tests on Li-ion batteries using round bars were documented in [4, 25].

To date, various methods of testing thermal performance of Li-ion cells under internal short-circuit have been proposed. However, it is difficult to create a small, isolated mechanical short-circuit inside a finished cell that mimics the type of internal

short-circuit that may lead to a field incident. The common experimental methods that attempt to create an internal short-circuit distort the overall cell integrity, create shorts in multiple locations, or sink heat and current to the cell can. Thus, analyzing internal short-circuit in finished Li-ion cells is limited by imperfect experimental methods.

Various abuse testing protocols and procedures have been formulated in order to evaluate and improve the safety standards of Li-ion batteries. These standards were developed by the Underwriters Laboratories (UL1642), The Society of Automotive Engineers (SAE J2464), Japan Storage Battery Association (JBA), United Nations (UN 38.3).

1.4 Modeling studies of Li-ion battery performance – literature review

We begin by reviewing a few models with various complexities and capabilities that have been developed to study and simulate Li-ion cells under normal operations.

Equivalent circuit models – The equivalent circuit model uses electrical circuit components such as resistors, capacitors and voltage sources to form a circuit network to describe the dynamics characteristics of batteries **[29-31]**. The equivalent circuit models feature simple implementation and fast calculation and thus have been widely adopted for modeling and design of battery management systems (BMS). There are many different equivalent circuit models, each of which has different complexity and application. A typical example is the RC model developed by SAFT that has been widely used for EV BMS modeling **[32]**. It consists of several resistors and capacitors to account for the various battery dynamics. The resistance and capacitance of these components are the parameters of the model, which need to be determined from experimental data. In other

words, experimental data must be collected by testing specific battery cells in order to build the equivalent circuit model. To take into account of the SOC and temperature effect, many tests have to be conducted at different SOCs or temperatures. Lookup tables are then built for determining the model parameters at different SOCs and temperatures. Therefore, a major drawback of the equivalent circuit based model is that many experimental tests have to be performed in order to build a model with adequate fidelity and reliability. Another disadvantage is that the developed equivalent circuit model is only good for the specific cells used for building the model. No equivalent circuit model can be used to study battery safety.

Single particle model – The single particle model (SPM) is physics based model in contrast to the equivalent circuit model, which is an empirical model. The SPM incorporates the effects of transport phenomena in a simple manner. Each of the anode and cathode electrodes is considered as a single solid particle with the same surface area of the electrode. Solid state diffusion within particles and electrochemical reactions at the interface of electrode and electrolyte are considered whereas the potential and concentration gradient in the electrolyte is usually neglected. Due to these simplifications, this model is very fast to use but only valid for limited conditions, such as low rate discharge and charge. By completely neglecting the electrolyte which plays a major role in battery safety, SPM is inherently unsuitable for safety analysis.

Electrochemical-thermal coupled model – Electrochemical model is a physics-based model that utilize fundamental electrochemistry and transport principles to describe the various physical processes within a battery. Electrochemical models for Li-ion cells were pioneered by Newman and co-workers **[33-35]** under isothermal assumption and

without accounting for thermal dynamics. The models were based on concentrated solution and porous electrode theories. The governing equations for the solid and electrolyte potentials and lithium ion species in the solid particle and electrolyte were derived using conservation laws within the battery cell. The resulted coupled non-linear partial differential equations (PDEs) were solved using numerical methods. This model is generic enough to incorporate a wide range of electrode chemistries and cell geometries, leading to the development of a number of similar models **[36-42]**. The kind of electrochemical models developed by Newman and coworkers lacks the thermal coupling and multi-dimensionality features that are essential to describe a battery safety problem.

Temperature plays a profound role in cell safety. There have been a number of studies to incorporate temperature effect in the modeling of Li-ion batteries. They can be divided into two categories. The first one is decoupled method. In this method, the heat generation data is obtained from experiments, where overpotential and entropic heat coefficient are gathered to calculate the heat generation rate. A thermal energy equation is then solved with inserted heat generation data to predict the battery temperature. A number of studies fall into this category **[43-50]**. Most of these studies assume uniform current and heat generation throughout batteries. Because of the decoupled approach, the dramatic temperature effect on the battery electrochemical performance cannot be considered. Another group of models belong to the electrochemical-thermal coupled (ECT) models **[38, 51-60]**. Different from the decoupled models, the ECT models calculate the heat generation from the solution of electrochemical equations rather than from experiments. The heat generation can then be inserted into the energy equation to get the temperature output. Some of the physiochemical properties such as solid diffusion

coefficient, ionic conductivity, exchange current density, etc. in the model are made temperature dependent, enabling study of temperature effect on the cell's electrochemical performance. A general Arrhenius form is often used to describe the temperature dependence.

All of the aforementioned models are based on one-dimensional (1D) assumption. The model geometry usually consists of an electrode sandwich of anode, cathode and separator and only the thickness direction of the geometry is considered. This approach is valid for simulating small capacity cell, in which the temperature and current distribution gradient is relatively small. For large-format Li-ion cells, 3D models are needed to take into account the complex cell structure and non-uniform distributions of variables. Since such models are usually computationally expensive, many of the 3D models in the literature made some approximations to simplify the calculation [45, 61-64]. A truly 3D multi-scale electrochemical-thermal coupled model has been developed for predicting the behavior of large-format Li-ion cells [65].

1.5 Modeling studies of Li-ion battery safety – literature review

Compared with the experimental works, there are very few efforts on the modeling of Li-ion battery safety and particularly internal short-circuit process. Most of the work in the literature focuses on predicting the cell thermal response by exerting specific heat sources due to various exothermic reactions. Hatchard et al. [19] developed a 1D thermal model to study the cell temperature response under abuse test such as oven heating. The heat generation for the model due to various exothermic reactions was calculated using reaction kinetics functions. Accelerating rate calorimetry (ARC) and

differential scanning calorimetry (DSC) tests were conducted to obtain the reaction

kinetic parameters. Spotnitz et al. **[66]** gave a comprehensive summary of the various

exothermic reaction kinetics for different anode and cathode active materials and built a

1D model to study the cell thermal behavior under different abusive scenarios. Spotnitz

also extended his model to simulate battery packs **[67]**. Due to the 1D nature, Spotnitz's

work cannot analyze internal shorting problems. Kim et al. **[68]** developed a 3D model

based on Hatchard's work to capture the effectt of size and shape on the cell's thermal

runaway behavior. Maleki et al. **[26]** conducted both experiments and thermal modeling

to investigate internal short-circuit behavior of small-scale Li-ion cells for electronic

applications.

All the above mentioned models can be determined as isolated thermal models,

where only temperature field is solved on the Li-ion cell geometry (1D or 3D). No

information about the cell's electrochemical performance during the short-circuit process

can be obtained in these models. As a matter of fact, the heat generation due to Joule

effect and electrochemical overpotentials, which may initiate exothermic reactions and

thermal runaway, can only be accurately described from the solution of electrochemical

model. Yamauchi et al.**[69]** developed an internal short-circuit study with consideration

of solving current and species concentration distribution, but the geometry for the model

was simplified and cannot represent realistic thermal boundary conditions for typical Li-

ion cell designs. More recently, Santhanagopalan et al. **[28]** presented an electrochemical-

thermal coupled model to study the internal short-circuit on a real cell geometry.

However, the electrochemical behavior of the cell during internal short-circuit, and how it

connects to the cell's thermal behavior, was not illustrated.

1.6 Overview of the present work

The current work focuses on the study of various performance and safety issues that are uniquely presented in large-format Li-ion cells using advanced battery modeling tool. Performance wise, a critical problem is increasing the energy density of large-format Li-ion cells. We show that scale-up of Li-ion cells could cause tremendous performance penalty compared with the maximum available cell performance. With the aid of modeling tool, we demonstrate a cell design path to mitigate the performance penalty and significantly improve the energy density of large-format Li-ion cells. For the safety study, we are interested in understanding the fundamental mechanisms of the internal short-circuit process of Li-ion cells. We utilize modeling to explain the electrochemical and thermal behaviors and their coupling during the internal short-circuit process.

A successful battery model aiming at tackling the above problems must be able to possess the following features.

(i). Multi-dimension. Both normal cell operation and internal-short circuit are intrinsically three-dimensional in large-format cells. The electrochemical reaction rate, active material utilization and heat generation could be highly non-uniform under certain operating conditions.

(ii). Multi-scale. The cell discharging behavior under normal and abusive conditions is controlled by a number of electrochemical and physical processes that take place at different temporal and spatial scales.

(iii). Electrochemical-thermal coupling. The internal short-circuit process is accompanied with dramatic temperature, current and voltage changes. The

electrochemical and thermal processes are highly interacting with each other during such complex process.

The present dissertation is organized as follows.

In Chapter 2, a general purpose multidimensional multiscale battery model is introduced. The model is extended to deal with the internal short-circuit modeling.

In Chapter 3, the battery model is used to study the scale-up of Li-ion cells. It is demonstrated that significant energy density increase can be gained by optimizing large-format Li-ion cells using multiple tabs on current collectors.

Chapter 4 and Chapter 5 focus on safety issues of Li-ion cells. In Chapter 4, the nail penetration process of Li-ion cells is studied. The electrochemical and thermal behaviors of a Li-ion during nail penetration are simulated by the battery model. Comprehensive parametric studies are carried out. Chapter 5 investigates the internal short-circuit problem of Li-ion cell. The difference between internal short-circuit and nail penetration is elucidated.

In Chapter 6, summary of the present work is made and possible future work is discussed.

Electrolyte

− Current Collector (Cu)

discharge

Li⁺

charge

Current Collector (Al) +

Negative Electrode

Separator

Positive Electrode
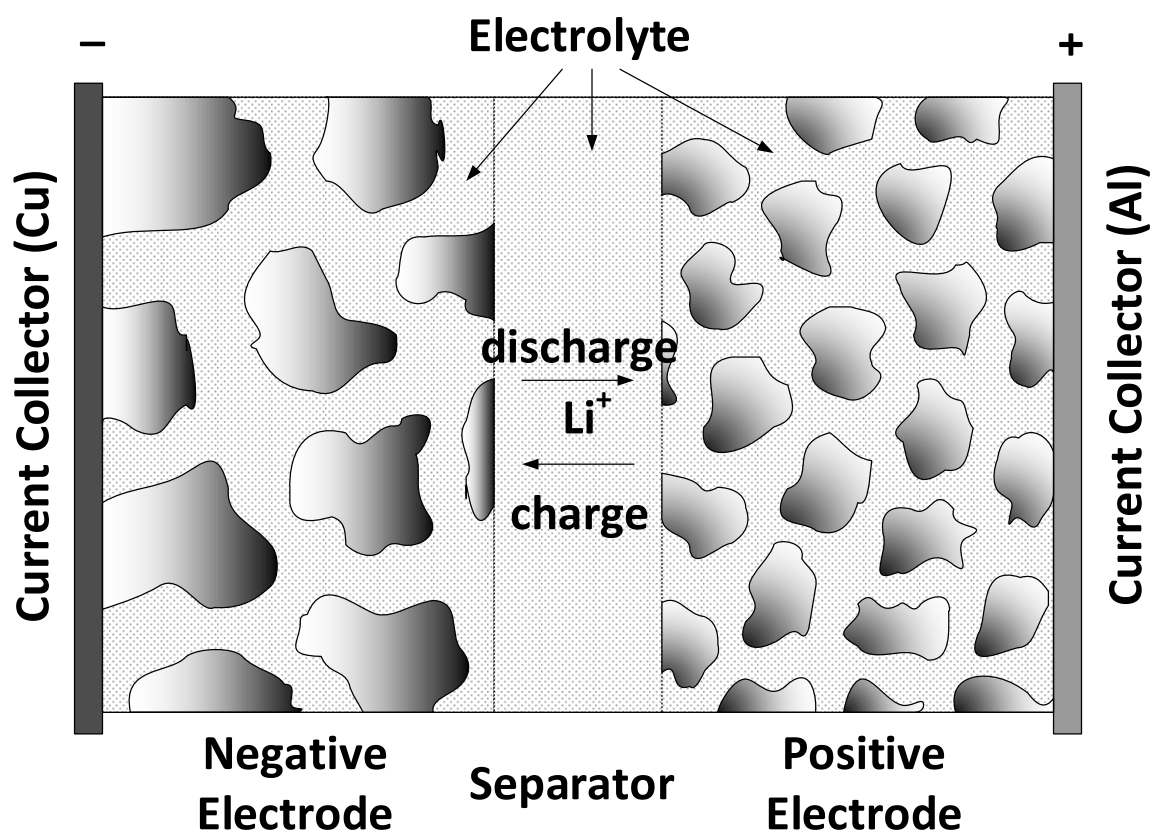
Figure 1-1: Schematic of the electrochemical process in a Li-ion cell
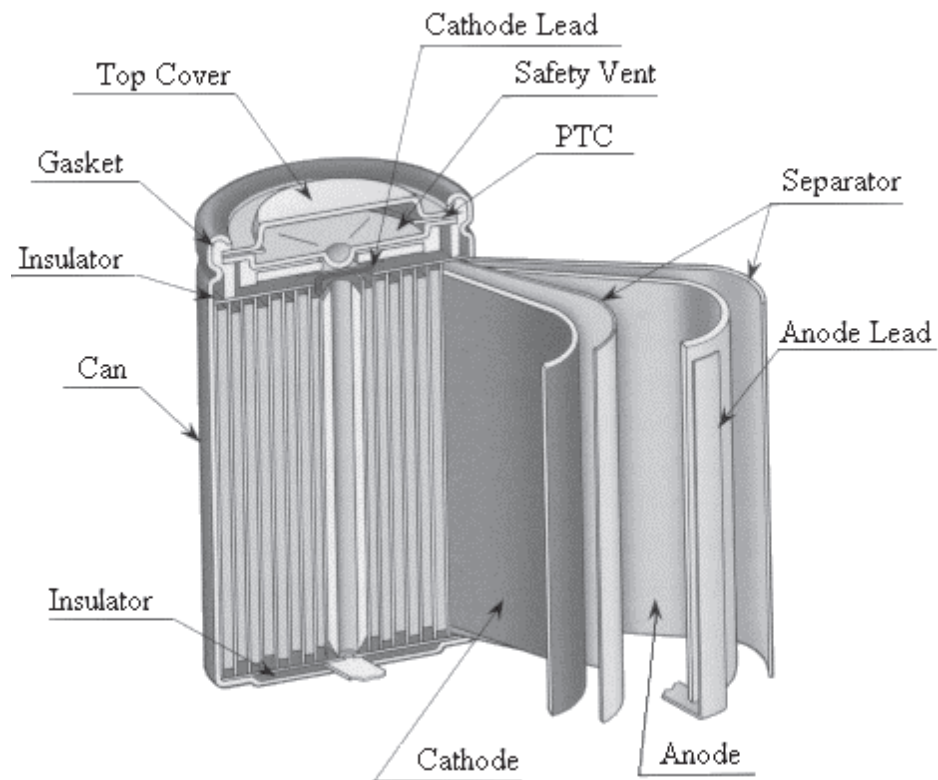
Figure 1-2: Cross-sectional view of a cylindrical Li-ion cell **[1]**
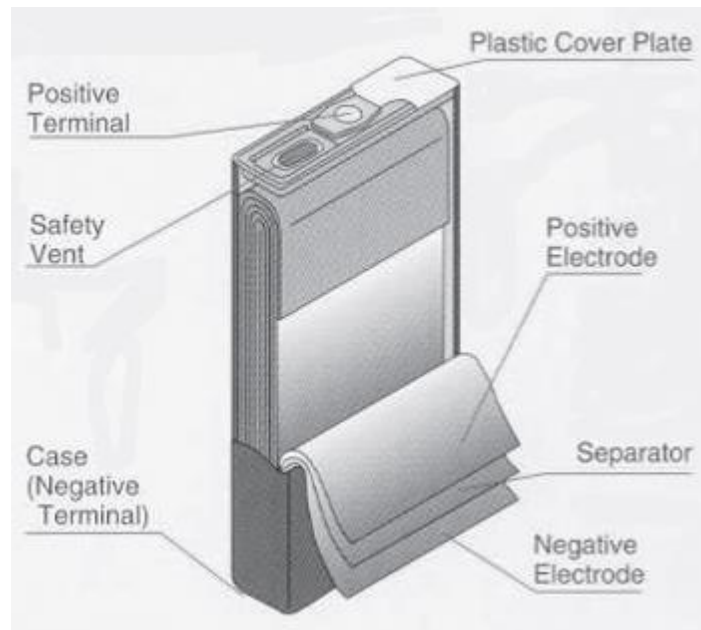
(a)
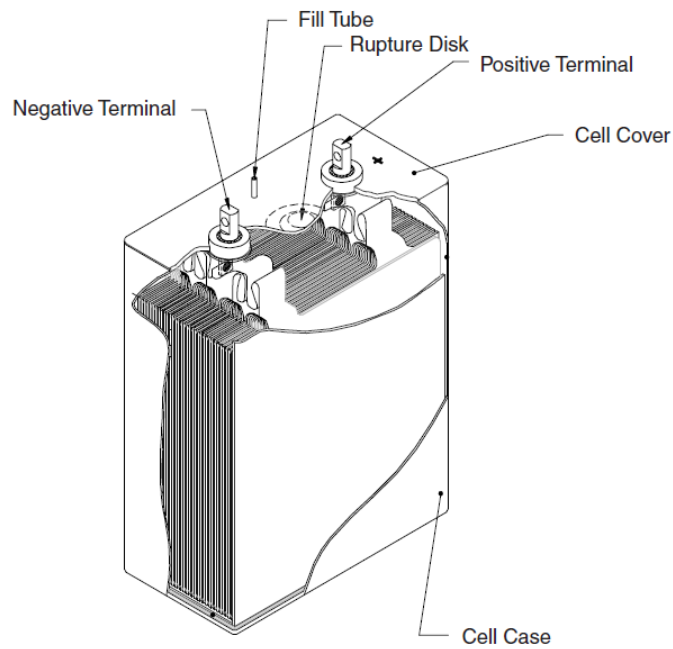
(b)

Figure 1-3: Schematic drawing of a prismatic cell with (a) wound electrode design, and (b) stacked-electrode design **[1]**

Figure 1-4 : The burned Li-ion battery (left) of the All Nippon Airways' Boeing 787. A new battery is shown on the right. **[13]**
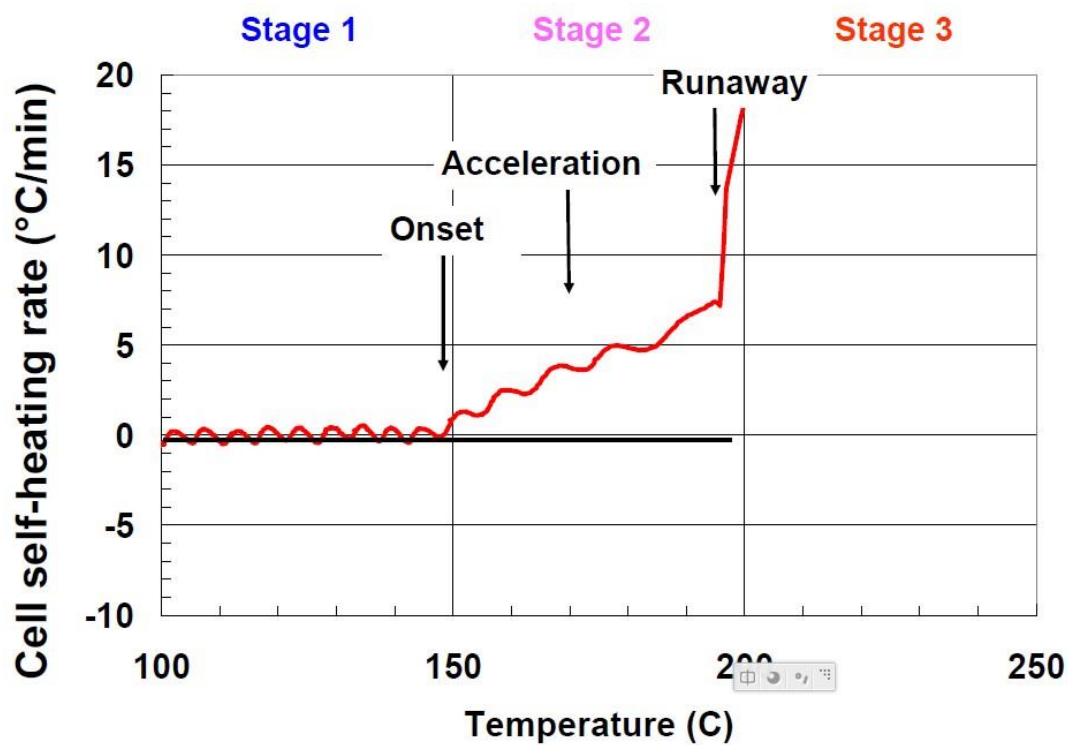
Figure **1-5**: Cell self-heating rate during forced thermal ramp test of Li-ion Gen 2 chemistry : anode = MCMB | electrolyte = 1.2 M LiPF6 in EC:PC:DMC | cathode = $LiNi_{0.8}Co_{0.05}Al_{0.05}O_2$ | separator = Celgard 2325 trilayer. **[14]**
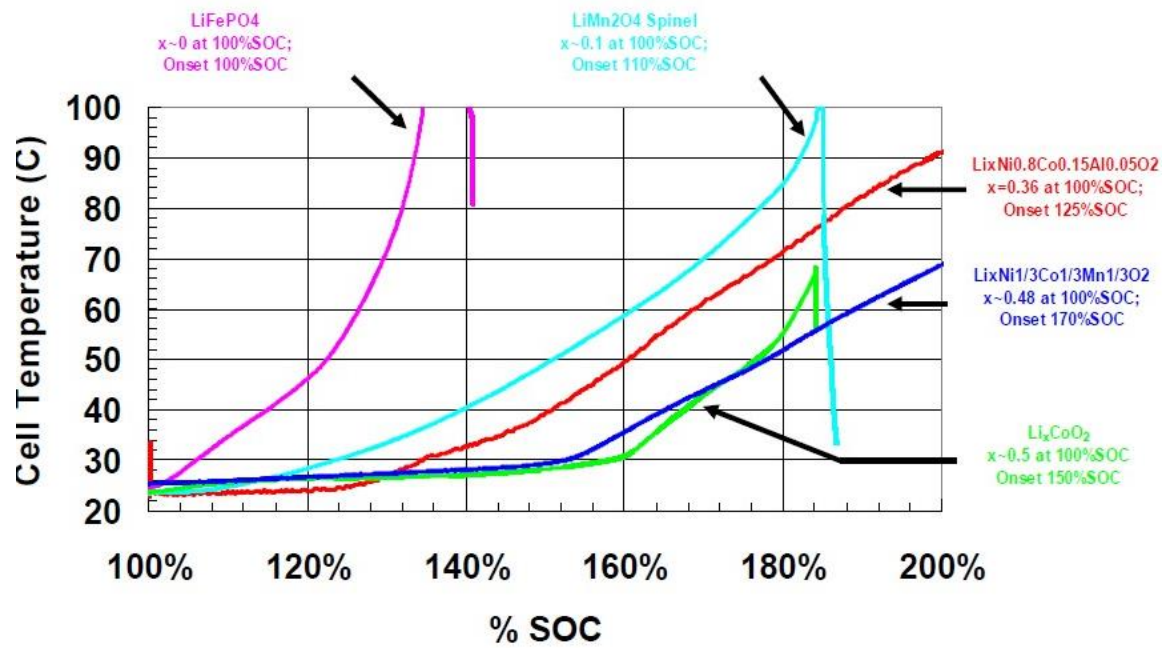
Figure **1-6**: Heat output during overcharge for different cathode oxide chemistries, showing a marked increase in heat output when final lithium is removed from cathode. **[15]**
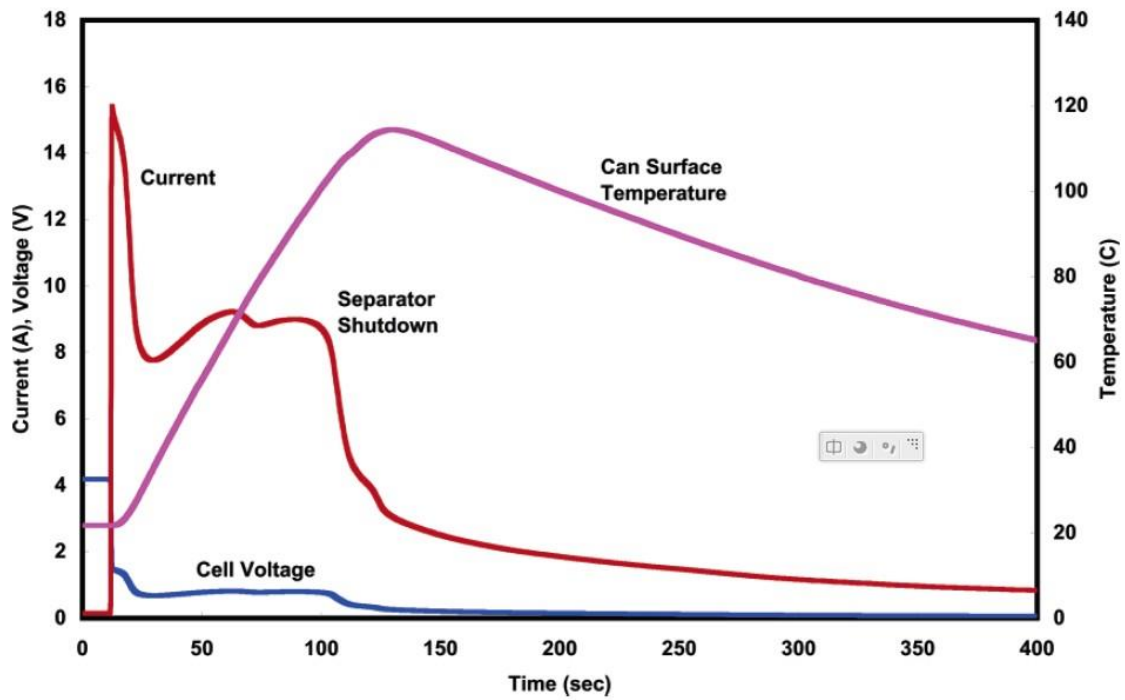
Figure 1-7: Typical external shorting behavior of a 18650 Li-ion cell with shutdown separator and without PTC (positive temperature coefficient) and CID (current interrupt device).**[16]**
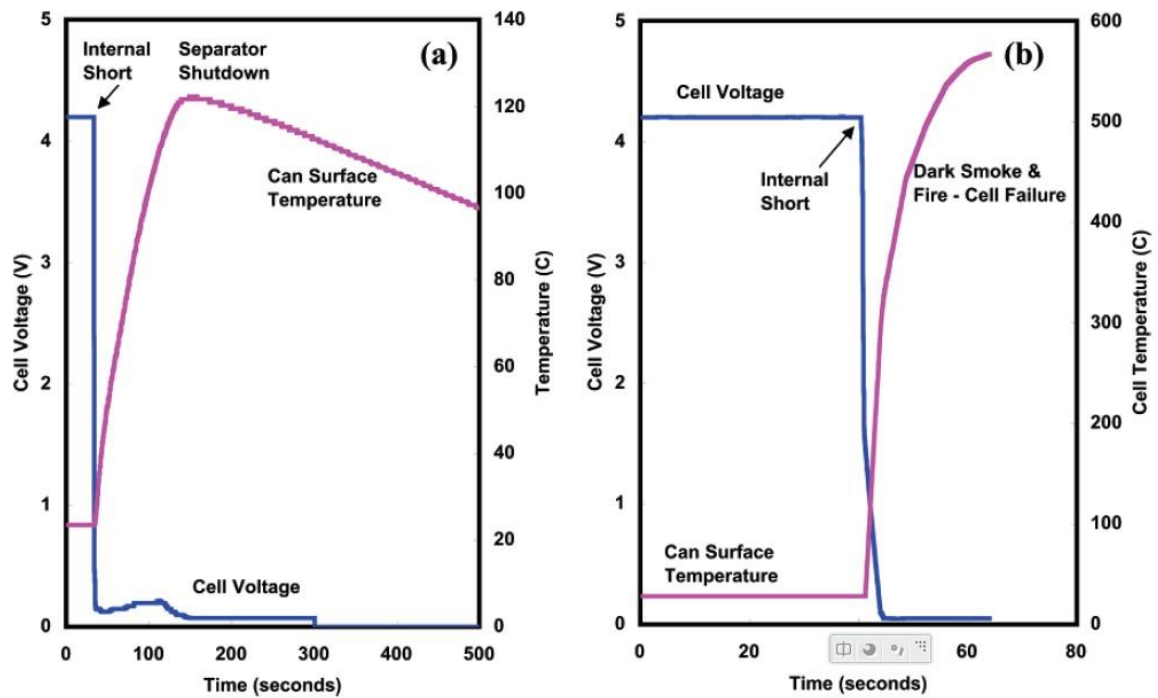
Figure 1-8: Typical nail penetration behavior of a 18650 Li-ion cell with shutdown separator (a) cell passed nail penetration test; (b) cell failed nail penetration test. **[16]**
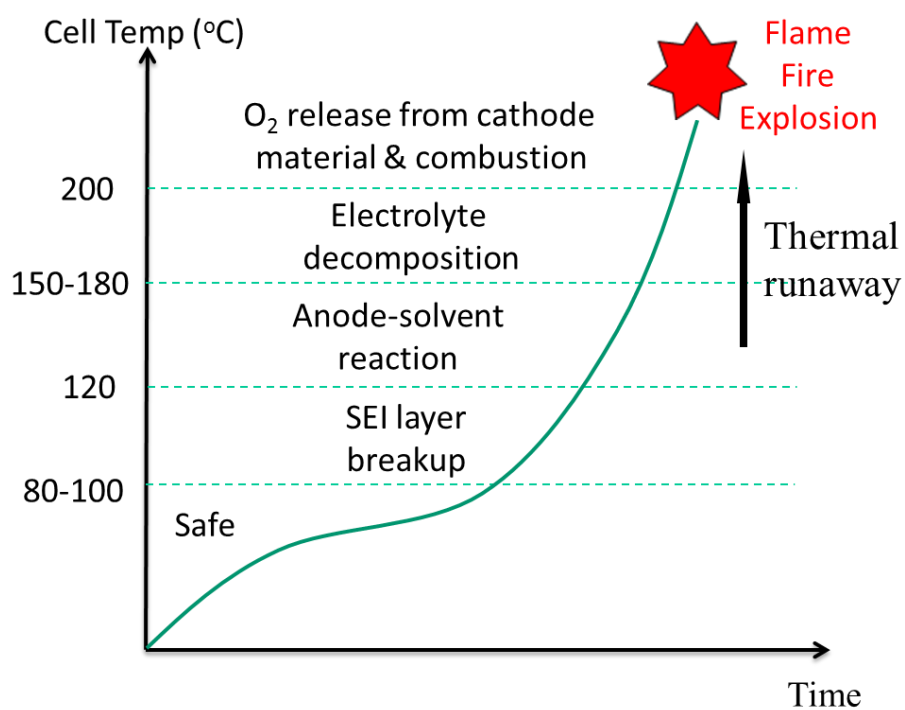
Figure 1-9: Schematics of the various exothermic reactions that lead to cell thermal runaway.
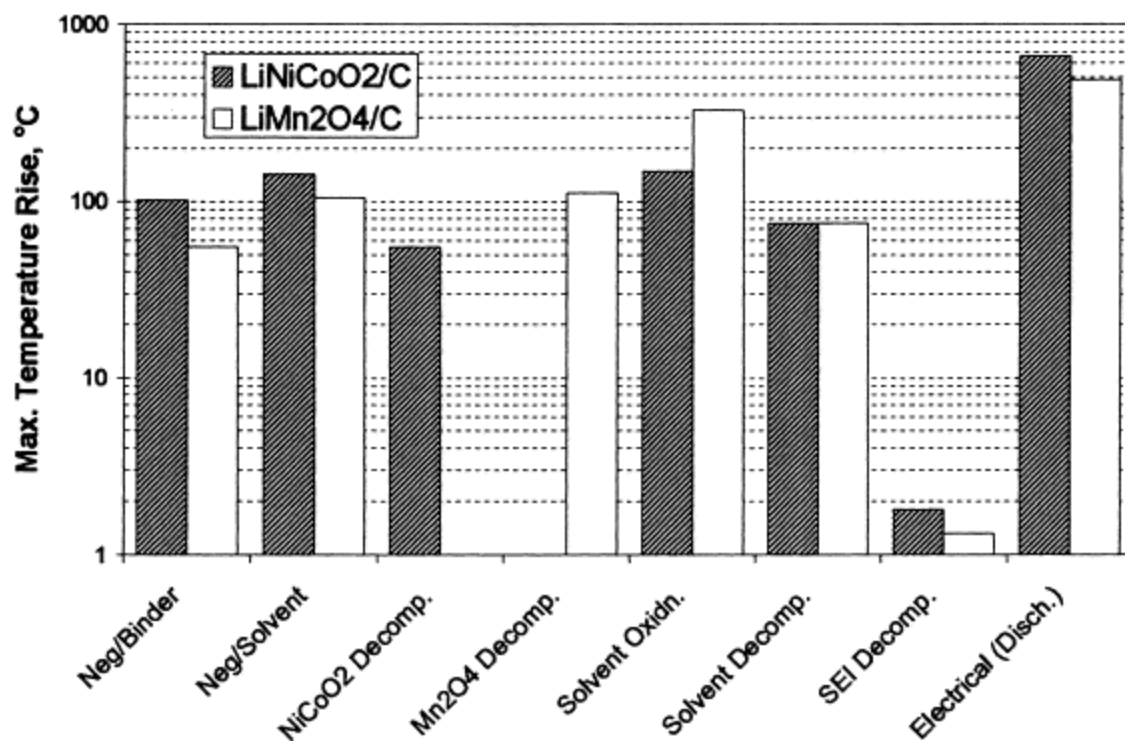
Figure 1-10: Estimated maximum temperature rise due to exothermic reactions during short-circuit. **[66]**

Chapter 2

Multi-dimensional Multi-scale Electrochemical-thermal Coupled model of Large-format Li-ion cells

Large-format Li-ion cells are expensive to make and the safety experiments on large-format Li-ion cells are very dangerous to perform. This makes modeling a valuable tool for studying large-format Li-ion cells. In this chapter, we describe a general-purpose battery modeling framework, developed based upon the work of Ref. **[33-35, 56, 58, 60, 65, 70]**. The key features of the current model includes multidimension, multiscale and electrochemical-thermal coupling (ECT). These functions of the model are essential for dealing with the various complex physical processes within batteries and for predicting the performance and safety of large-format batteries used in electric vehicles (EV) and hybrid electric vehicles (HEV).

2.1 Electrochemical and thermal coupling [56, 70]

Temperature has a strong influence on the battery performance, cycle life and safety. Some of the physiochemical properties in the model are made temperature dependent, enabling study of temperature effect on the cell's electrochemical performance. A general Arrhenius form for the physiochemical property Ψ is used to describe the temperature dependence.

$$\Psi = \Psi_{ref}\exp\left[\frac{E_{act}^{\Psi}}{R}\left(\frac{1}{T_{ref}} - \frac{1}{T}\right)\right] \qquad (2\text{-}1)$$

In this work, the physiochemical properties following Eq. **2-1** include solid and electrolyte diffusion coefficients, electrolyte conductivity and exchange current densities (D_s, D_e, κ, i_0). The activation energy, E_{act}^{Ψ} , controls the sensitivity of a property to temperature, and Ψ_{ref} is the property value defined at reference temperature, $T_{ref} = 298\ K$.

2.2 Multidimensional and multi-scale approach [65]

A successful battery model should be able to describe the various physical processes occurring over a wide range of time and spatial scales in batteries. The present modeling framework is constructed in a hierarchical structure to realize such need. The diagram in Fig. **2-1** illustrates the multiscale nature of the model. On the macro scale, large-format Li-ion cells are usually manufactured to have either stacked-electrode design or spirally wound design. A number of cells can also be connected in a string to form a battery pack. The macro-scale level of the model is able to take account all the detailed cell geometry, as well as all other components in battery packs, including terminal connections, can/enclosure, cooling configurations, etc. On the electrode level, the electrochemical reactions, species transport, and heat generations in the composite electrodes consisting of active material and electrolyte are modeled based on porous electrode theory and conservation laws. By solving the governing equations, detailed species distributions, such as Li^+ concentration in electrolyte, solid and liquid phase potentials, can be obtained. The lithium diffusion in the active material particles can determine the cell's rate capability. In practice, particle size in Li-ion cells is usually made on the order of several μms **[1]**. This particle level solid diffusion process needs to

be taken care of using an additional micro-scale model. In this work, all the active

material particles are considered to be spherical. A solid diffusion equation in spherical

coordinate is solved at each point of the anode and cathode electrodes.

2.3 Governing Equations

The complete set of governing equations is summarized in Table **2-1**. The

transport equations of charge and lithium concentration in both solid and liquid

electrolyte phases are coupled through volumetric current density j^{Li}, which quantifies

the reaction rate of lithium intercalation and de-intercalation reactions at the interface of

active material particles and electrolyte. Bulter-Volmer equation is generally assumed to

describe the reaction kinetics.

$$j^{Li} = a_s i_0 \left\{ \exp\left[\frac{\alpha_a F}{RT}\eta\right] - \exp\left[-\frac{\alpha_c F}{RT}\eta\right]\right\} \tag{2-2}$$

The local surface overpotential, η, which controls the kinetic reaction rate, is defined as

the difference between the electronic and electrolyte phase potential, with respect to the

open circuit potential (OCP).

$$\eta = \phi_s - \phi_e - U \tag{2-3}$$

The exchange current density, i_0, is a function as lithium concentration in both electrolyte

and solid active materials

$$i_0 = k(c_e)^{\alpha_a}\left(c_{s,max} - c_{s,e}\right)^{\alpha_a}\left(c_{s,e}\right)^{\alpha_c} \tag{2-4}$$

where c_e and c_s are the volume-averaged lithium concentration in the electrolyte and

solid phase, respectively, $c_{s,max}$ is the maximum lithium concentration that can be taken

by the active materials, and $c_{s,e}$ is the lithium concentration at the electrode/electrolyte

interface. The OCP value is a function of local surface stoichiometry, defined as $x =$

$c_{s,e}/c_{s,max}$. The OCP values for graphite in negative electrode and NCM for positive

electrode, respectively, are shown in Fig. **2-2 [71, 72]**. The diffusional conductivity

k_D^{eff} in Eq. **2-24** is defined by concentration solution theory **[34]** as

$$\kappa_D^{eff} = \frac{2RT\kappa^{eff}}{F}(t_+^0 - 1)\left(1 + \frac{d \ln f_\pm}{d \ln c_e}\right) \tag{2-5}$$

where $(t_+^0 - 1)\left(1 + \frac{d \ln f_\pm}{d \ln c_e}\right)$ is the thermodynamic factor and its value in electrolyte with

LiPF$_6$ is a function of lithium concentration in electrolyte, c_e, and temperature. The

lithium diffusion coefficient and ionic conductivity in electrode are also strong functions

of c_e, and temperature. The transport properties for LiPF$_6$ based electrolyte are plotted in

Fig **2-3 [73]**.

The temperature distribution can be obtained by solving the conservation of

energy equation (Eq. **2-27**). The heat generation is mainly from three sources, namely

Joule heat as a result of current flowing through solid and electrolyte phases, reaction

heat caused by charge transfer reaction at the electrolyte/electrode interface, and

reversible entropic heat as a function of OCP derivative with respect to temperature (Fig.

2-4 [74, 75]).

$$q_j = \sigma^{eff}\nabla\phi_s\nabla\phi_s + k^{eff}\nabla\phi_e\nabla\phi_e + k^{eff}\nabla\ln c_e\nabla\phi_e \tag{2-6}$$

$$q_r = j^{Li}(\phi_s - \phi_e - U_j) \tag{2-7}$$

$$q_e = T\frac{\partial U_j}{\partial T} \tag{2-8}$$

2.4 Boundary condition treatment

Boundary conditions are implemented by using the additional source term technique. The variables for the boundary nodes are not included and solved in the discretized algebraic equations. Instead, equivalent source term corresponding to the specific boundary condition is added to the control volume that is adjacent to the boundary node to ensure conservation of charge. The implementation theory is illustrated in Fig. **2-5**.

2.5 Numerical technique and convergence criterion

The governing equations (Eqs. **2-23** – **2-27**) are discretized using finite volume method (FVM). Explicit forward Euler method is used to treat the time-dependent terms. All the governing equations are solved sequentially at each time step and the calculation proceeds to the next time step if the convergence criteria are met. For constant rate charge/discharge condition, the charge balance over the entire cell is used as a critical convergence criterion.

$$\varepsilon_I = \min \left(\left| \frac{I_a - I_0}{I_0} \right|, \left| \frac{I_c - I_0}{I_0} \right| \right) \tag{2-14}$$

where I_a and I_c are the total output current of anode and cathode electrode, respectively.

$$I_a = \int_{anode} i_a dA \tag{2-15}$$

$$I_c = \int_{cathode} i_c dA \tag{2-16}$$

ε_I is chosen to be very small (<0.1%) to ensure physically meaningful results.

2.6 Extension of the model to simulate Li-ion battery safety

The above described multi-dimensional multi-scale Li-ion battery model is extended to model critical Li-ion battery safety problems. Specifically, in this work, we focus on two problems: nail penetration and internal short-circuit by a metal particle. They both belong to the short-circuit problem, which is the most dangerous abusive conditions for Li-ion batteries. Understanding the fundamental electrochemical and thermal mechanisms behind the problem is of paramount importance to improve the abuse tolerance of Li-ion batteries.

A short-circuit happens when the anode and cathode of the battery are connected by an electrically conductive object. If the object is outside of the battery cell, e.g. connecting the positive and negative terminals with a wire, it leads to external short-circuit. If the object is within the cell, internal short-circuit is induced. Fig **2-6** shows the electrical circuit diagram of the two short-circuit scenarios. It can be seen that in internal short-circuit, a close loop of current is formed inside the battery cell. All the cell electrochemical energy is released as the form of Joule heat (I^2R) through the cell internal resistance (R_i) and short-circuit resistance (R_s). On the other hand, in external short-circuit, the portion of the heat generation R_s is outside of the cell, having no contribution to the heating of the cell. Moreover, in internal short-circuit, the heat generation from R_s can be highly localized, which causes local hot spot that easily triggers exothermic reactions and thermal runaway. The heat generation due to the cell internal resistance, R_i, on the other hand, is globally distributed within the cell.

In order to simulate the internal short-circuit process, it is important that our model is able to deal with the close-loop current path presented during the process. Fig.

2-7 compares the electrons and lithium ions transport paths of internal short-circuit process with that of normal discharge operation. A small cell unit, consisting of a Cu foil, an anode, a separator, a cathode and an Al foil, in the vicinity of the short-circuit location is chosen for the illustration.

In an internal short-circuit, an electrically conductive object resides within the cell and connects the Cu foil and Al foil together. The lithium delithiation reaction occurs in the anode active materials releasing electrons and lithium ions. The electrons transport to the Cu foil and converge to short-circuit spot. The electrons are further conducted through the short-circuit object and spread out to the Al foil. The lithium ions, on the other hand, transport through the separator to the cathode. The lithium lithiation reaction happens in the cathode active material with the lithium ions from the separator and electrons from the Al foil. The converging and diverging electrons transport in the Cu and Al foils makes the current path 3D for internal short-circuit process. In comparison, the current path of a normal discharge process is much simpler and could be handled by using 1D assumption. Therefore, multidimensional model is essential to study the internal short-circuit problem.

The short-circuit boundary condition is implemented in the current model in such a way that it follows the same technique used for modeling normal operations. Instead of explicitly solving the solid potential equation within the short-circuit object, a constant resistance boundary condition is applied on the surface of Cu foil at the location of short-circuit spot, as shown in Fig. **2-8**. A fixed voltage (usually 0) boundary condition is applied on the Al surface at the location of short-circuit spot. In this way, the electrons

and lithium ions transport paths in the battery cell is equivalent to that shown in Fig. **2-7**

(a), but the implementation is greatly simplified.

Using the same source term addition technique described in Sec **2.4**, the short-

circuit boundary condition is implemented as follows.

Short-circuit B.C.:

$$q''_{N-1} = -\frac{\phi_{s,N-1}}{R_s \Delta As} = \sigma^{eff} \frac{\phi_{s,N-1} - \phi_{s,N}}{\Delta x_{1/2}}$$

$$S_c = 0 \tag{2-17}$$

$$S_P = -\Delta A \frac{1}{R_s \Delta As + \Delta x_{1/2}/\sigma^{eff}}$$

The short-circuit resistance is a combination of intrinsic resistance of the short-circuit

object and the contact resistance caused by imperfect contact of short-circuit object and

the cell components.

$$R_s = R_{sco} + R_{ct} \tag{2-18}$$

And

$$R_{sco} = \frac{l_{al} + l_{an} + l_{sp} + l_{ca} + l_{cu}}{\sigma_{sco} A_{sco}} \tag{2-19}$$

$$R_{ct} = \frac{\overline{R_{ct}}}{A_{ct}} \tag{2-20}$$

where l_{xx} is the thickness of the specific cell component, σ_{sco} the electrical conductivity

of the short-circuit object, and A_{sco} the cross-sectional area of the short-circuit object

(πr_s^2). $\overline{R_{ct}}$ is the area specific contact resistance and A_{ct} is the side area of the short-

circuit object ($\pi d_s(l_{al} + l_{an} + l_{sp} + l_{ca} + l_{cu})$).

The current passing through the short-circuit object can be calculated using

Ohm's law,

$$I_s = \frac{\phi_{s,N-1}}{R_s} \tag{2-21}$$

The volumetric heat generation within the short-circuit object is then calculated using Joule's law,

$$q_s = \frac{I_s^2 R_s}{V_s} \tag{2-22}$$

where V_s is the volume of the short-circuit object ($\pi r_s^2 (l_{al} + l_{an} + l_{sp} + l_{ca} + l_{cu})$).This heat generation is added as a source term to the cell volume occupied by the short-circuit object when solving the energy equation (Eq. **2-27**).

Due to the strong potential and temperature gradient in the vicinity of short-circuit location, the computational mesh is refined around the short-circuit location. In the region distant from the short-circuit location, relatively coarse mesh is used. Fig. **2-10** shows an example of the non-uniform mesh used in the current work.
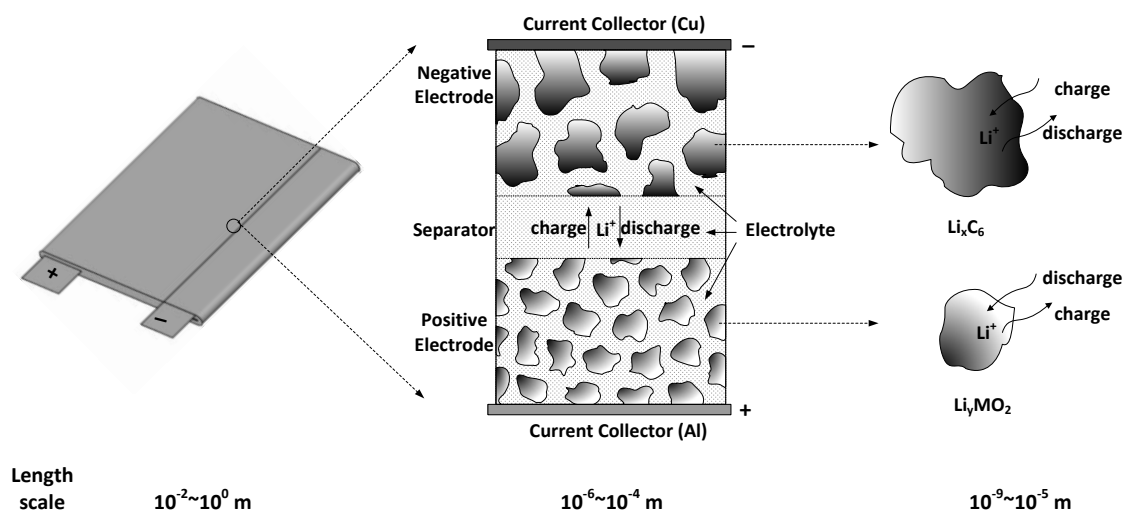
Figure 2-1: Schematic of a large-format Li-ion cell and the multiscale physical and electrochemical processes within cell during charge/discharge
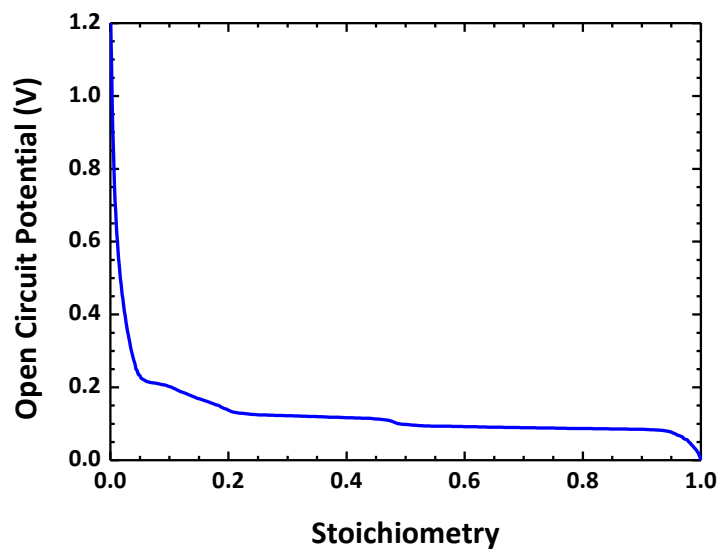
(a)
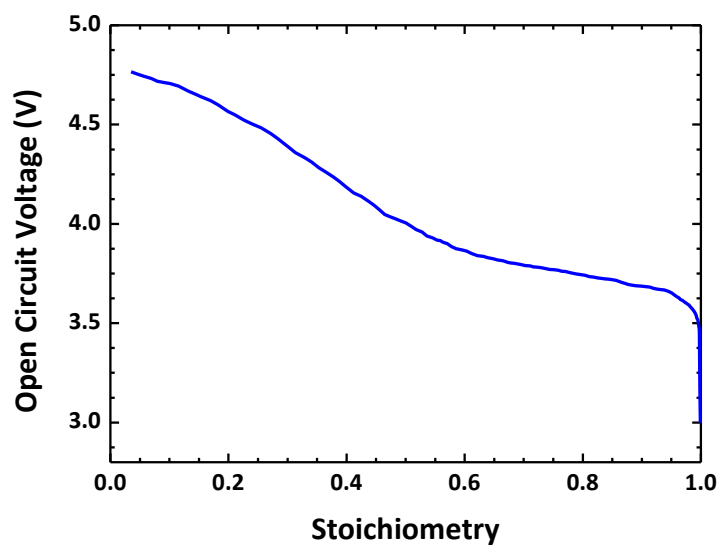
(b)

Figure 2-2: OCP (open circuit potential) of an electrode material (a) graphite (Li_xC_6) **[71]**; (b) NMC ($Li_xNi_{1/3}Mn_{1/3}Co_{1/3}O_2$) **[72]**.
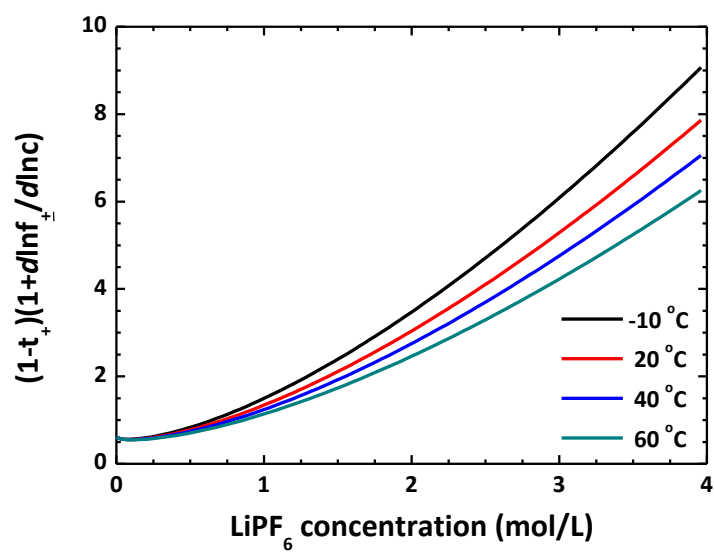
(a)
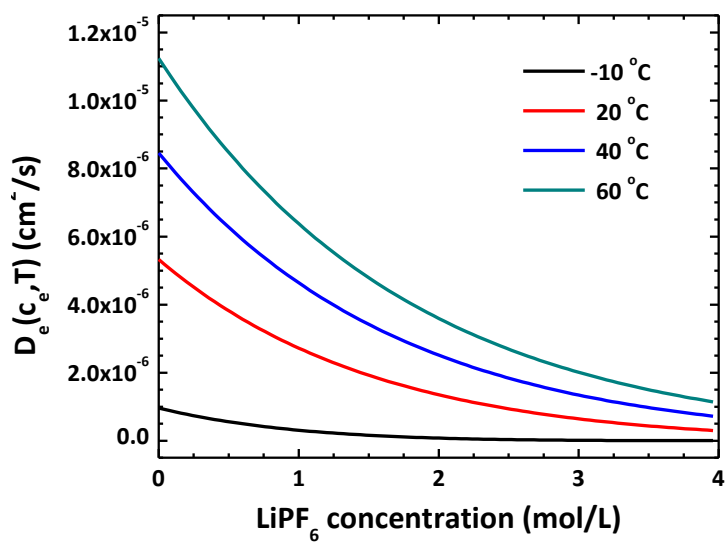
(b)
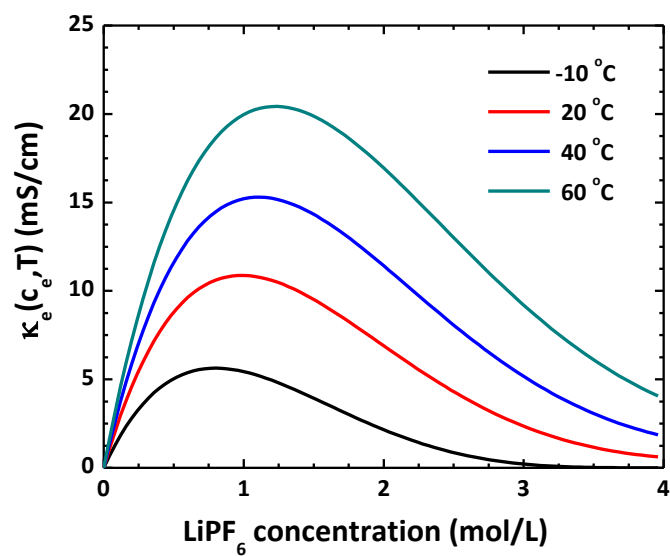
(c)

Figure 2-3: Transport properties of LiPF$_6$ based electrolyte (a) thermodynamic factor; (b) diffusion coefficient; (c) conductivity **[73]**
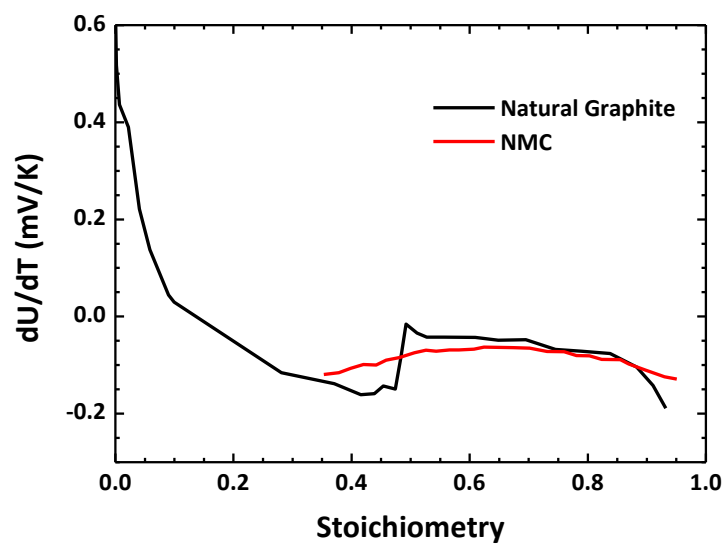
Figure 2-4: dU/dT data for graphite (Li_xC_6) anode and NMC ($Li_xNi_{1/3}Mn_{1/3}Co_{1/3}O_2$) cathode **[74, 75]**.
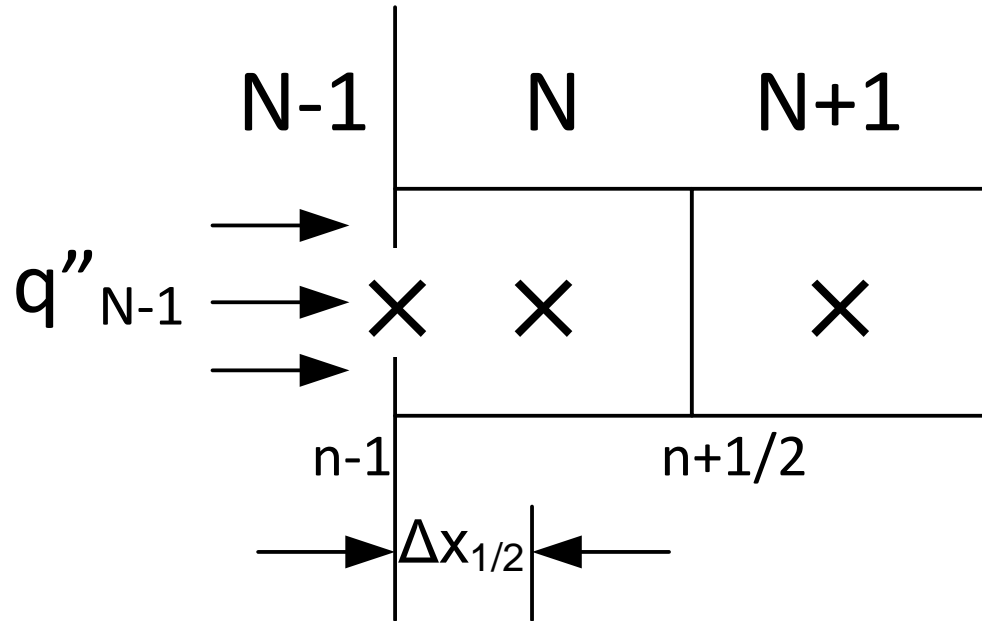
Figure 2-5: Boundary condition treatment in the model.
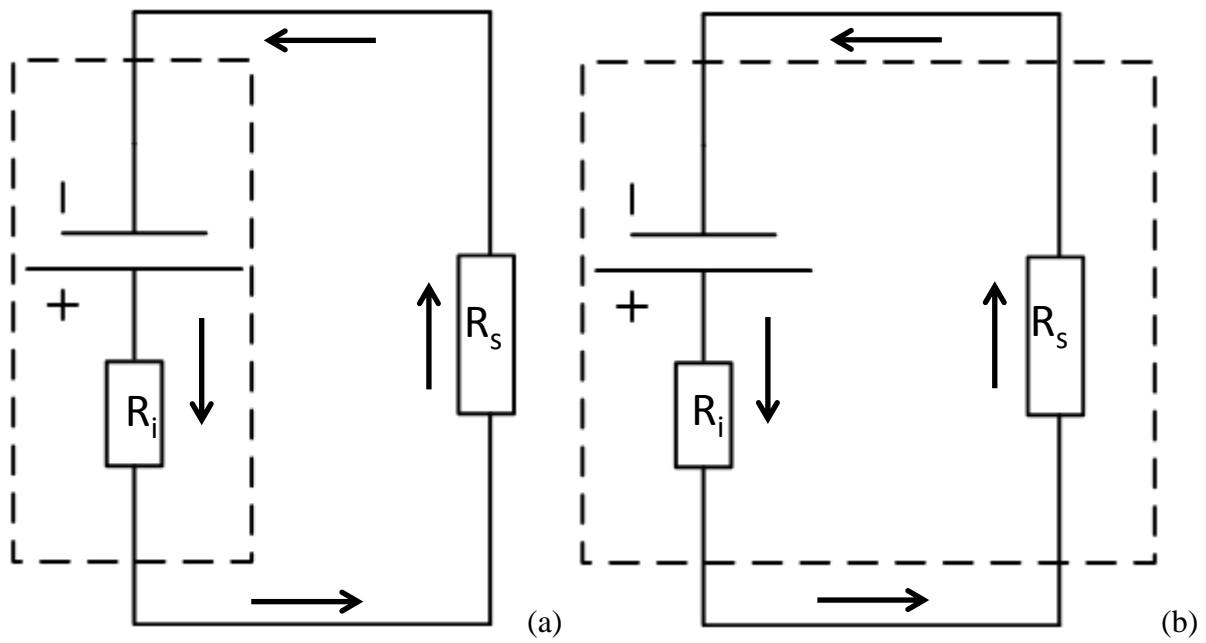
Figure 2-6: Electric circuit diagram of short-circuit of Li-ion cells (a) external short-circuit; (b) internal short-circuit.
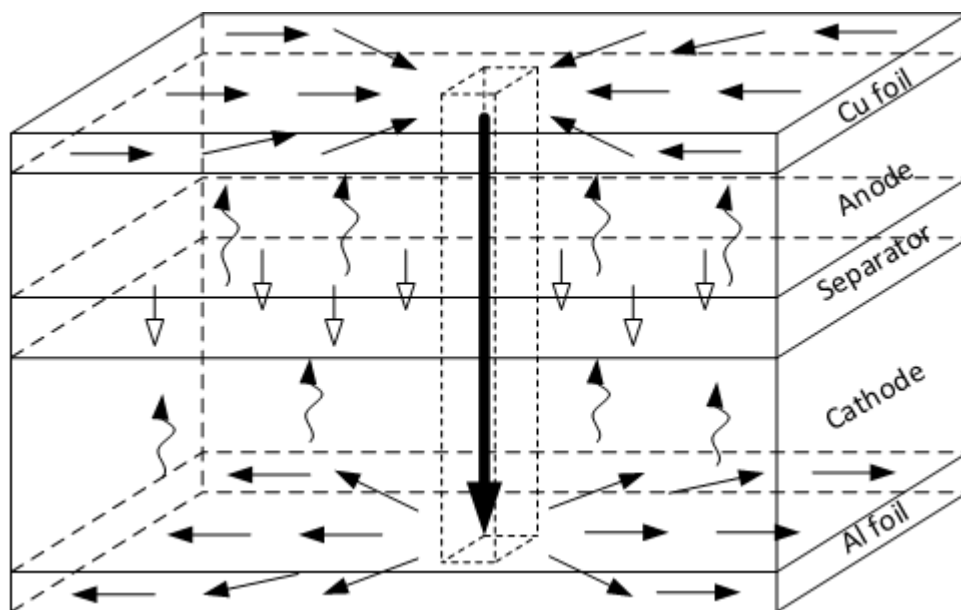
(a)
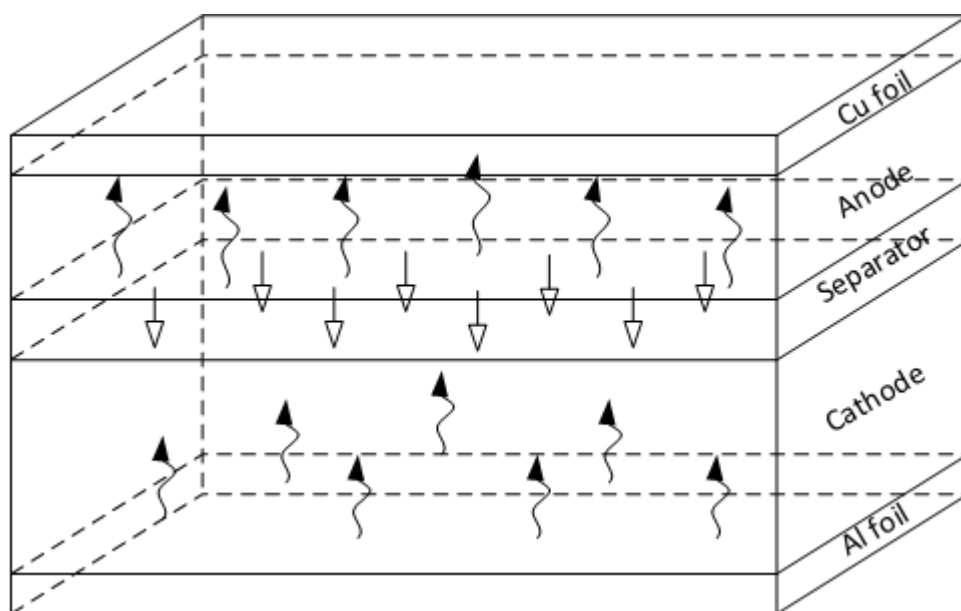
(b)

Figure 2-7: Schematic of the electrons and ions transport path in a Li-ion cell during (a) internal short-circuit process and (b) normal discharge process.
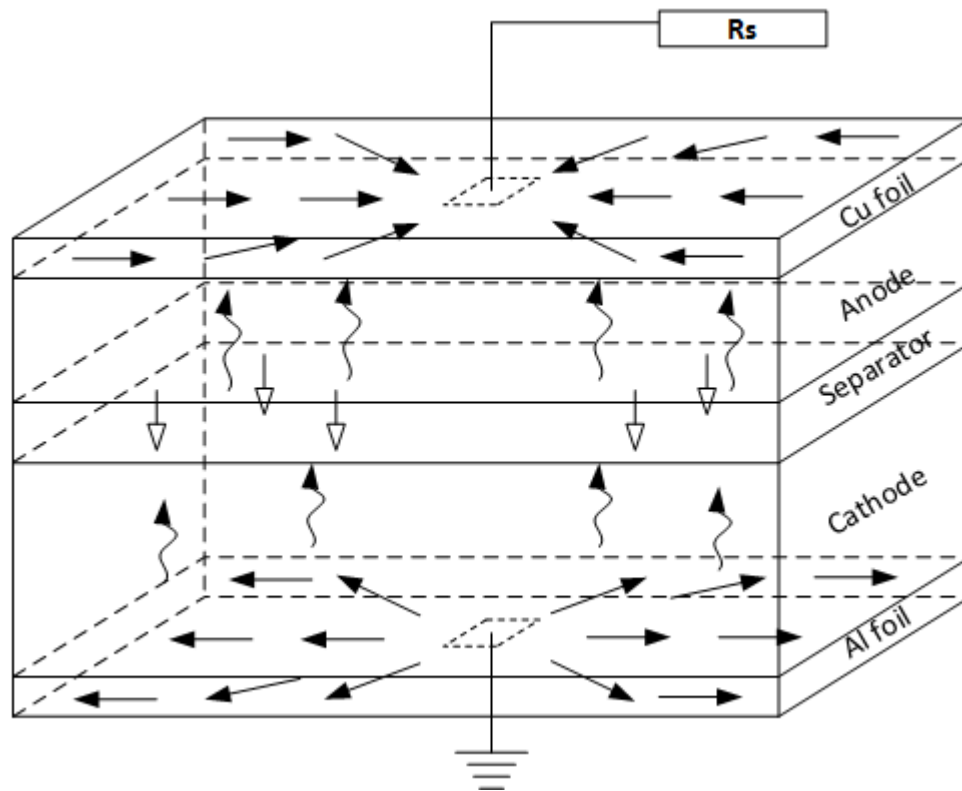
Figure 2-8: Applying constant resistance boundary condition at the short-circuit location to model the internal short-circuit problem.
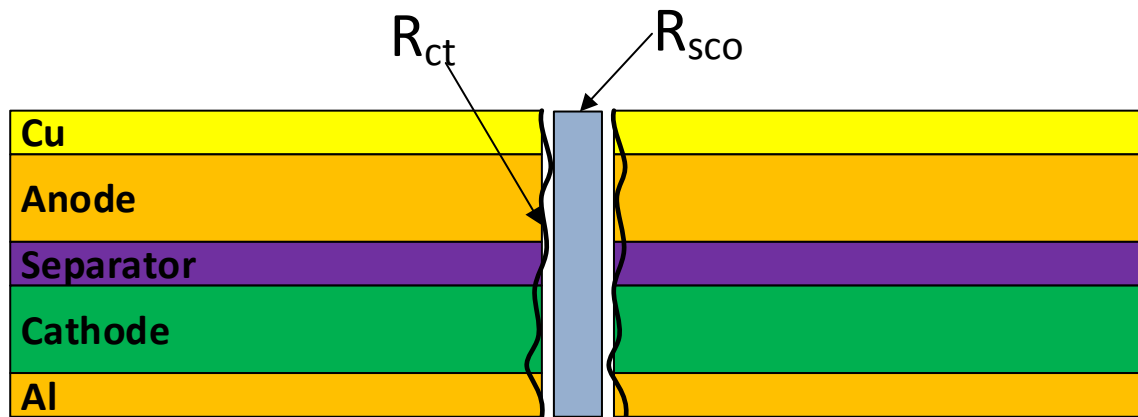
Figure 2-9: Schematic of intrinsic resistance of the short-circuit object and contact resistance.
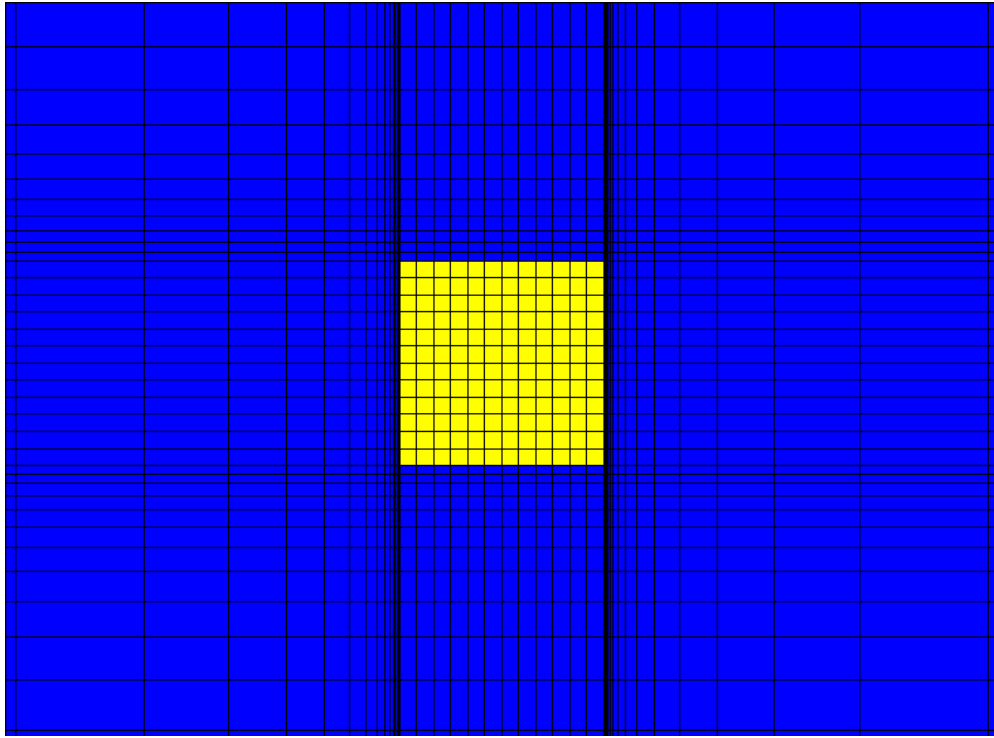
Figure 2-10: Non-uniform computation mesh in the vicinity of short-circuit location.

Table 2-1. Governing equations of the 3D Li-ion cell model

Conservation Equations:

Charge, Solid Phase

$$\nabla \cdot (\sigma^{eff} \nabla \phi_s) = j^{Li} \tag{2-23}$$

Charge, Electrolyte Phase

$$\nabla \cdot (k^{eff} \nabla \phi_e) + \nabla \cdot \left(k_D^{eff} \nabla \ln c_e\right) = -j^{Li} \tag{2-24}$$

Species, Electrolyte Phase

$$\frac{\partial(\varepsilon_e c_e)}{\partial t} = \nabla \cdot \left(D_e^{eff} \nabla c_e\right) + \frac{1 - t_+^0}{F} j^{Li} \tag{2-25}$$

Species, Solid Phase

$$\frac{\partial c_s}{\partial t} = \frac{D_s}{r^2} \frac{\partial}{\partial r}\left(r^2 \frac{\partial c_s}{\partial r}\right) \tag{2-26}$$

Heat

$$\frac{\partial(\rho c_p T)}{\partial t} = \nabla \cdot (k \nabla T) + q_e + q_r + q_j \tag{2-27}$$

Chapter 3

Effect of tab design on large-format Li-ion cell performance

3.1 Introduction

Small Li-ion batteries have been widely used for consumer electronics due to their high power and energy density. Large Li-based batteries are believed to be essential for vehicle- and grid- energy storage enabling a sustainable energy future. How to unlock the potential of existing Li battery materials and scale up Li-ion cells to 10-100 Ah sizes without substantially lowering the cell's energy density remains a key technological challenge.

The two typical designs for large-format Li-ion batteries are the spirally wound design and stacked-electrode design. Both involve very long electrodes. If only one pair of negative and positive current-collecting tabs is used, as illustrated in Fig. **3-1(a)**, electrons generated in the anode electrode must travel a long distance before being collected by the negative tab. Similarly, the electrons coming from the positive tab need to be spread out over a long distance to reach all areas of the cathode electrode. Consequently, severe voltage loss is caused due to the Ohmic resistance of electron transport through thin current-collecting foils. This Ohmic loss can be very significant when the electrodes are sufficiently long as naturally occurs in large-format Li-ion cells. This situation would be exacerbated when the cell is operated at high power, which is ubiquitous in HEV/EV applications.

In addition to the Ohmic loss through long current collector foils, another phenomenon that contributes to low performance in large cells is uneven current density

distribution and hence non-uniform utilization of active material as experimentally demonstrated recently [76]. Due to Ohmic resistances of the current collectors, a solid potential distribution forms along each of the electrode current collectors, reducing the local potential difference driving reaction current. Consequently, local current generation in regions distant from the two tabs is lower than that closer to the tabs that suffer less Ohmic loss in solid electrical potential. Such a non-uniform current distribution results in non-uniform utilization rate of active materials, making average utilization of active materials in a large cell far lower than that in a small coin cell. The non-uniform utilization of active materials causes not only lower energy density than what could be expected from battery materials but also localized overcharge and overdischarge situations. Therefore, both the power and energy are compromised in large-format cells.

One solution to the above-described issue in cell upscaling is to use a plurality of tabs on the current collectors, as illustrated in Fig. **3-1(b)**. This way, the large electrode area is divided into relatively small regions, each with its own tabs for current collection. The electron transport length is shortened and the current density distribution is more uniform, leading to more uniform active material utilization. As the tab number increases, it is expected that the cell performance will approach the coin cell benchmark. However, the outcome of using excessive tabs is increased manufacture cost and decreased reliability due to tabs welded together. An optimal number of tabs thus exist for large-format cell design. A design tool for large cell structures that enables full utilization of active materials and maximum potential of energy density is highly desired.

To date most of the battery models in the literature belong to 1D models. They are therefore inadequate to address the problem of spatially non-uniform potential and

current distribution in large-format Li-ion cells. In this work, we use the fully 3D model

described in Chapter 2 to study the behavior of large-format battery cells. The model has

the ability to deal with coupling processes, such as species transport and electrochemical

reactions during the dynamic operation of Li-ion cells. It can also take into account both

the 3D geometrical details of the cell, such as the cell shape, tab size, location and

number, and the cell winding structures, which are uniquely important for large-format

cells.

The purpose of the present work is three-fold. Firstly, we quantify the significant

performance loss in large-format cells relative to the coin cell benchmark. The

fundamental reasons for such a performance penalty will be elucidated. Secondly, we

demonstrate a possible 50% increase in energy density by optimizing designs of large Li-

ion cells using multiple tabs on current collectors. Thirdly, we assess the effect of tab

number on cell performance. The ultimate goal is to help battery manufacturers and

experimentalists find direction in boosting battery performance closest to its theoretical

material capacity.

3.2 Modeling approach

The model utilized here is the multidimensional multiscale Li-ion cell model developed

in Chapter 2. A 40Ah large-format Li-ion cell is chosen for the present study. The cell

has a graphite anode and a NMC cathode. Table **3-1** lists the cell design parameters. The

cell has a total electrode length of 512 cm and electrode width of 20.5 cm. Both the Cu

and Al current collectors are double-side coated with active materials. The separator is

placed between the two electrode sheets and the multilayer structure is wound to form a

prismatic cell. A computational mesh resolving the detailed cell winding structure and tab configuration is shown in Fig. **3-2**. Several important physiochemical parameters used in the model are listed in Table **3-2**.

3.3 Results and discussion

The baseline case has one pair of tabs welded outward from the end edges of the long sides of current collectors. Two types of tab arrangement are considered here, as illustrated in Fig. **3-3**. Depending on the relative positions of the positive and negative tabs, they are named as co-located (CO) tab design and counter-located (CU) tab design. The CO design has both positive and negative tabs located at the leading edge ($z = 0$) of the current collectors. In the CU design, the negative tab is located at the trailing edge ($z = L$) of the Cu current collector and the positive tab is located at the leading edge ($z = 0$) of the Al current collector.

Fig. **3-4** shows the calculated 1C discharge curves for the two cell designs. The corresponding discharge curve of a coin cell with the exact same electrode formulation and cell assembly in small surface area is depicted for comparison. It is evident that the performance of large-format cells, both CO and CU designs, is far inferior to the coin cell performance. Table **3-3** lists the energy density calculated from the modeling data for different cells at several C-rates. The data is normalized by the energy density of coin cells at 1C discharge for better comparison. At 1C discharge, the CO cell and CU cell can achieve only 39% and 52% of the energy density of coin cells, respectively. At higher C-rate operation, the performance loss is even more severe. For example, the CU cell cannot go to 2C or 3C discharge because the cell voltage will drop below 2.5V at the

beginning of discharge. This is the evidence that in scaling up Li-ion cells from coin cells or small cells to large-format cells, performance loss could be significant. Therefore, engineering optimization for the cell design must be carried out in addition to the material development in order to attain superior performance at large-format.

Besides the common fact that CO and CU cells both have significant performance penalty compared with the coin cell, their discharge curves behave very differently. At the beginning of discharge, the voltage loss relative to the coin cell is 0.163V in the CO cell and 0.824V in the CU cell, respectively. The CO cell thus has a higher power output than the cell with CU design. However, the discharge curve of the CO cell exhibits a much steeper slope, indicating a rapidly increased voltage loss during discharge. Thus, although having a better initial performance, the CO cell drops below 2.5V cut-off voltage at an earlier discharge stage (at $SOC = 58.2\%$), while the CU cell can reach the point where $SOC = 35.2\%$.

The source of performance loss in large-format cells and the difference in the behaviors of CO and CU cells can be explained by examining internal variables distributions predicted by the model. Since the large cell has a high aspect ratio ($L \gg W$), we are only interested in the variable distribution along the electrode length direction, i.e. z-direction defined in Fig. **3-2**. At each location along the z-direction, the variables of interest are averaged across the electrode width direction (y-direction). Here, solid potential , current density, and local SOC along the current collectors are the variables of interest, and their distributions are displayed in Figs. **3-5**, **3-6** and **3-7**, respectively. Three time instants, corresponding to the beginning, middle and end of discharge, are chosen for analysis.

Fig. **3-5(a)** shows the solid potential profile along Al and Cu current collectors of the CO cell. At the beginning of discharge (t = 1 s), the solid potential gradient in both current collectors is mainly confined in the region very near the two tabs. The local potential difference that drives the electrochemical reactions decreases along the electrode length direction. Therefore, a highly non-uniform current density distribution along the electrode length direction is formed, as shown in Fig. **3-6(a)**. Note that the local current density is normalized by the average current density, defined as the total discharge current divided by the electrode area. At t = 1 s, in the area near the tabs the current density is as high as ~10 times of the average current density, while the current density is almost zero at the electrode area near the trailing edge of the cell. This is the indication that the total current is mostly contributed from the reaction of electrode materials that are located close to the tabs. It can be estimated that the first 1/3 of the electrode contributes 98% of the total current at t = 1 s. The high current density concentrating near the tabs region results in a relatively small Ohmic loss in the current collectors, explaining the higher initial voltage of CO cell in Fig. **3-4**. The voltage loss along current collectors ($\Delta \phi_s = \phi_{s,z=L} - \phi_{s,z=0}$) is 0.07 V in the Al foil and 0.08 V in the Cu foil, respectively.

The highly non-uniform current density distribution of CO cell at the beginning of discharge is the root cause for the subsequent rapid voltage drop shown in Fig. **3-4**. The non-uniform initial current density distribution results in significant non-uniform utilization of active material. One can quantify the degree of active material utilization by local SOC ($iSOC$), which is defined by coulomb counting as,

$$iSOC(z,t) = 1 - \frac{\int_{t_0}^{t} i_a(z,\tau)d\tau / 3600}{C/A} \tag{3-1}$$

where i_a is the local current density. Fig. **3-7(a)** plots the $iSOC$ distribution for the CO

cell. Due to the very high current density near the tabs region, the active material in that

region is consumed faster and becomes depleted more quickly than the region far from

the tabs. The $iSOC$ is initially uniform everywhere and equal to the fully charged state. At

t = 750 s, $iSOC$ $(z = 0) = 28\%$ and $iSOC$ $(z = L) = 96\%$. At the end of discharge, where t

= 1500 s, $iSOC$ $(z = 0) = 5\%$ and $iSOC$ $(z = L) = 89\%$, respectively. This means the

majority of the active material near the trailing edge of the electrode has not been used

when the discharge process is terminated. This non-uniform utilization of active material

brings down the cell voltage by two mechanisms. Firstly, as the active material near the

tabs area becomes depleted, the current has to be supplied by the active material

downstream. As shown in Fig. **3-6(a)**, the current density peak propagates toward the

downstream of electrodes as the discharge goes on. This increases the electrons transport

length and therefore the Ohmic loss through the current collectors. Secondly, the local

OCP decreases with the consumption of active material. In Fig. **3-5(a)**, it can be observed

that as the discharge proceeds, the solid potential gradient penetrates towards the

downstream of electrodes and the voltage loss in the current collectors becomes larger. At

t = 750 s, $\Delta\phi_s$ = 0.37 V and 0.44 V in Al and Cu current collectors, respectively. At the

end of discharge, where t = 1500 s, $\Delta\phi_s$ = 0.64 V and 0.54 V, in Al and Cu current

collectors, respectively. Consequently, although the CO cell has a higher initial discharge

voltage, this higher voltage cannot be sustained and it drops more quickly than the CU

cell and hits the cut-off voltage earlier.

The CU cell has a unique tab configuration in which the positive tab is located at the leading edge ($z = 0$), and the negative tab is at the trailing edge ($z = L$). Thus, the electrons transport length for any local section of the cell remains constant and equal to the total electrode length L. Consequently, different solid potential distribution evolves in contrast to the CO cell, as shown in Fig. **3-5(b)**. The local potential difference is more evenly distributed along the electrode length, compared with that of CO cell, leading to more uniform current density distribution, as illustrated in Fig. **3-6(b)**. In addition, the current density of the CU cell exhibits almost symmetric distribution. At the beginning of discharge (t = 1 s), the current density is higher at the two ends of the electrode and smaller in the cell center. The current density peak propagates from both ends towards the center as the discharge proceeds. Due to the symmetric and more uniform current density distribution, the local *SOC* also is lowered symmetrically and more uniformly than that of CO cell, as shown in Fig. **3-7(b)**. The total discharge time of CU cell is therefore longer than the CO cell because of more uniform utilization of active materials. However, at the beginning of discharge, due to the longer electrons transport length and hence higher Ohmic loss than the CO cell, the CU cell has a lower output voltage than that of CO cell.

The above analysis demonstrates that large-format Li-ion cells, fabricated in spirally wound structures and equipped with only a single pair of tabs, exhibit significant power and energy loss. It is imperative to explore ways to improving cell design in order to regain the performance corresponding to a coin cell made of the same materials. One solution is to use a plurality of tabs placed strategically on the current collectors in the electrode length direction. This will reduce the Ohmic loss along the current collectors

and promote the uniformity of reaction current distribution, thereby improving the cell performance. The number of tabs, however, should be kept minimal so as to reduce manufacture cost and increase reliability. In practice, however, it is largely based on battery designers' empirical experience to determine how many tabs would be necessary to mitigate the performance loss. Trial and error has been widely adopted for battery design, which becomes more expensive and time consuming when used for the design of large-format cells. The 3D battery model described in the present work is then a powerful tool for this purpose.

Fig. **3-8** sketches various multi-tab configurations for CO cell and CU cell. In the current study, the tabs are evenly spaced on the current collectors along the electrode length direction. The resulting effect is dividing a long electrode into small sections that are connected in parallel by tabs. Specifically, for the CU design, the total electrode is divided into (N-1) sections, where N is the total tab number. The total electrode of the CO design is divided into (N-2) sections. Fig. **3-9** shows the effect of tab number on the 1C discharge performance of CO and CU cell. It is evident that adding multiple tabs effectively boosts the performance for both CO and CU cell. The cell energy densities of the different designs are compared and listed in Table. **3-3**. It is noteworthy that by adding only one positive tab in the CU cell and two tabs in the CO cell, the performance for both cell designs can be greatly improved from the baseline cases. For example, at 1C discharge, the energy density is increased from 52% to 89% for the CU cell and from 39% to 80% for the CO cell, respectively. The same trend holds true for higher C-rate discharge. Further increasing the tab number would make the cell performance approach

the coin cell benchmark. Generally speaking, an average of 50% gain in energy density can be achieved for large-format cells by utilizing effective multi-tab design.

It is argued earlier and generally believed that maintaining uniform current density distribution is critical for boosting the performance of large-format Li-ion cells. Therefore it is of great interest to develop a quantitative relationship between the uniformity of current density distribution and cell's overall energy density.

A quantitative measure of current density uniformity must take account of the spatial variation of current density along the electrode length. It should also consider the change of the variation with respect to time, given the fact that discharge/charge of battery is an intrinsically transient process. In statistics and probability theory, standard deviation is used to show how much variation exists from the mean value. Here we define a time-averaged standard deviation as an index to evaluate the current density distribution uniformity during a discharge/charge process, i.e.

$$\overline{\sigma} = \sqrt{\frac{\int_{t_0}^{t} \sigma(\tau)^2 d\tau}{\int_{t_0}^{t} d\tau}} \qquad (3\text{-}2)$$

where $\sigma(\tau)$ is the instantaneous standard deviation of the local current density distribution, which can be calculated by

$$\sigma(\tau) = \sqrt{\frac{1}{N}\sum_{i=1}^{N}(i_i(\tau) - i_{avg})^2} \qquad (3\text{-}3)$$

where the subscript i represents each control volume discretized in the computational mesh and N denotes the number of total control volumes. In practice, the battery model uses finite time steps. Eq. **3-3** then becomes,

$$\overline{\sigma} = \sqrt{\frac{\sum_{i=1}^{N_t} \sigma_i^2 \cdot \Delta t_i}{\sum_{i=1}^{N_t} \Delta t_i}} \qquad\qquad (3\text{-}4)$$

where Δt_i is the ith time step and N_t is the total number of time steps. Noting that $\overline{\sigma}$ has the same unit as that of current density, one can normalize $\overline{\sigma}$ by the average current density for better comparison, which is termed as the current density non-uniformity factor in later discussions.

Fig. **3-10** shows such a direct link of the cell's energy density with the current density non-uniformity factor for CO cells and CU cells with different tab numbers. It is clearly demonstrated that the current density uniformity strongly affects the cell's energy density. For both designs, as the tab number increases, the current density distribution becomes more uniform (indicated by the decrease of $\overline{\sigma}$) and the cell performance, i.e. the energy density, improves substantially.

Another observation from Fig. **3-10** is that while the both curves for the CO cell and CU cell indicate strong correlation between the cell's energy density and current density non-uniformity factor, they quantitatively differ. Therefore caution must be taken when comparing cells with vastly different structure designs. Finally it is worth noting that for cells with current density non-uniformity factor between 0.1 and 0.2, the cell's energy density could be lowered by 10% from its maximum realizable by a coin cell.

The significance of these quantitative results, shown in Fig. **3-10** for the first time in the literature, is that they point out new ways to increase the cell's energy density besides material innovations. The potential through cell architecture innovation is great, amounting to 50%-level improvement. In addition, Fig. **3-10** quantifies the importance of achieving uniform current distribution in large-format Li-ion cells, an engineering topic

that has been largely overlooked. Only recently Zhang et al. **[77]** began the measurements of local current density distribution as part of large-format battery diagnostics.

Efforts are currently underway to experimentally validate the quantitative relationship between the cell's energy density and current distribution non-uniformity as discovered in Fig. **3-10**. Other interesting questions await further research and clarification. Do the two curves depicted in Fig. **3-10** for the two extreme cell structures represent the upper and lower bounds of all cell designs? Does a fan-shaped correlation between energy density and current density non-uniformity factor exist universally for other battery materials? What are parameters or mechanisms controlling the curve slope and how one can achieve the smallest slope possible?

3.4 Conclusion

Engineering optimization is imperative to boost performance of large-format Li-ion cells in order to achieve the full potential of existing battery materials. A multidimensional, electrochemical and transport coupled model has been applied, for the first time, to address current density distribution uniquely present in large-format Li-ion cells. It is shown that for a large-format cell with spirally wound structure, significant performance loss is induced compared with the coin cell having the same active materials and electrode formulation. It is found that the performance loss results from the electrons transport through long current collectors, which not only causes large Ohmic resistance, but also creates non-uniform utilization of active materials. It is further shown that the tab number and location can mitigate the Ohmic loss, thereby significantly improving the cell performance. Two tab configurations, namely counter-located (CU) design and co-

located (CO) design, have been proposed and their impact on the cell performance has been quantified. An average of 50% gain in energy density can be achieved through innovative placement of tabs. We also presented a quantitative correlation between the cell's energy density and current distribution non-uniformity for the first time in the literature.

Table 3-1 Design parameters of the 40Ah Li-ion cell

	Positive Electrode	Negative Electrode
Chemistry	$Li_yCo_{1/3}Ni_{1/3}Mn_{1/3}O_2$	Li_xC_6
Loading amount	27 mg/ cm^2	12.0 mg/ cm^2
Electrode thickness	120 μm	110 μm
Foil thickness	20 μm	10 μm
Separator thickness	40 μm	
Electrolyte	PC/EC/DMC 1M LiPF$_6$	
NP ratio	1.13	
Electrode width	20.5cm	
Electrode length	512 cm	
Total active area	20992 cm^2	
Nominal capacity	40 Ah	

Table 3-2 Physiochemical parameters used in the model

Parameter	Unit	Cu foil	Negative electrode	Separator	Positive electrode	Al foil
Density	kg/cm^3	8960×10^{-6}	1200×10^{-6}	525×10^{-6}	2860×10^{-6}	2700×10^{-6}
Electron conductivity	S/cm	5.8×10^5	1.0		0.1	3.538×10^5
Maximum Li capacity	mol/cm^3		0.031		0.0518	
Stoichiometry at 0%/100% SOC			0.042/1.0		0.98/0.39	
Charge transfer coefficient			0.5		0.5	
Reference exchange current density	A/m^2		26		2.0	
Diffusion coefficient – solid phase	cm^2/s		9.0×10^{-10}		1.5×10^{-10}	
Bruggeman tortuosity exponent			1.5	1.5	1.5	
Transference number				0.363		
Porosity			0.46	0.4	0.29	
Particle radius	cm		10×10^{-4}		3×10^{-4}	
Initial electrolyte concentration	mol/cm^3			0.001		
Cell temperature	°C			25		

Table 3-3 Comparison of calculated energy density of various cell designs

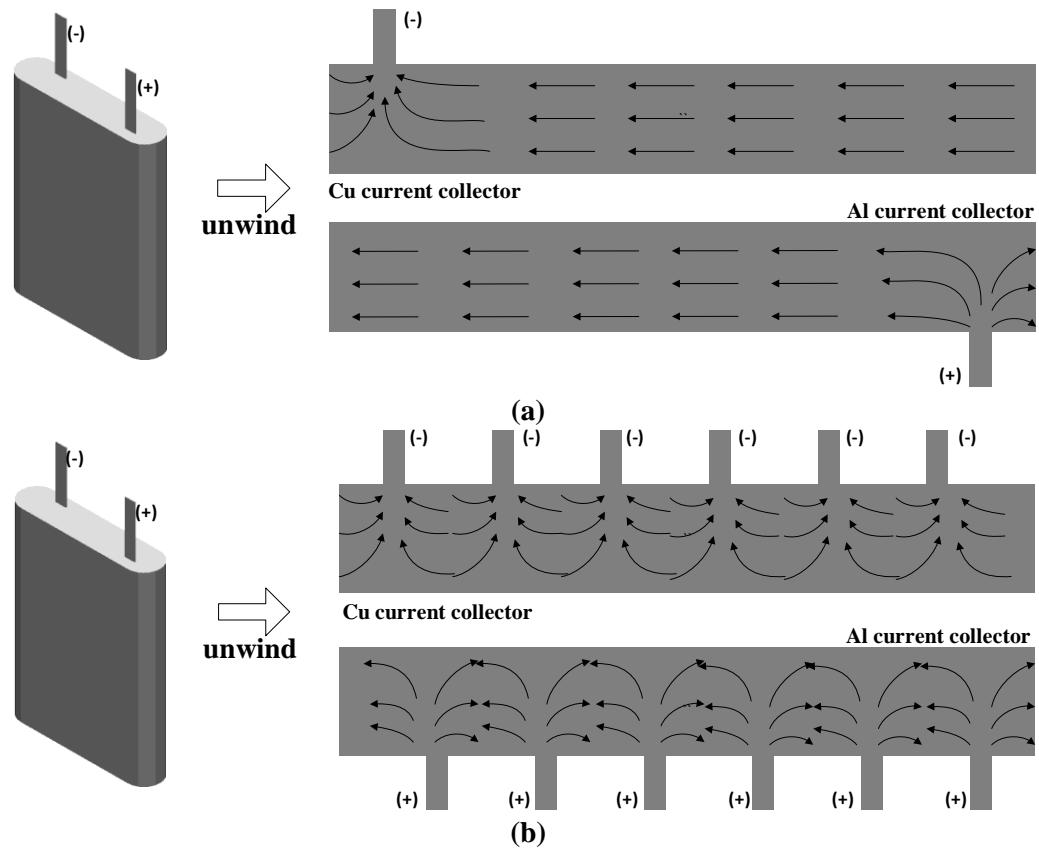|	1C discharge	2C discharge	3C discharge
Coin Cell	100%	87%	75%
Baseline cell			
2 tabs (CO)	39%	10%	3.3%
2 tabs (CU)	52%	N/A	N/A
Multi-tab cell			
3 tabs (CU)	89%	68%	62%
4 tabs (CO)	80%	62%	44%
5 tabs (CU)	96%	84%	71%
6 tabs (CO)	97%	84%	71%
7 tabs (CU)	98%	85%	73%
8 tabs (CO)	99%	85%	73%

Figure 3-1: Electrons transport path in the current collectors of a spirally wound cell: (a) cell with a single pair of tabs; (b) cell with multiple pairs of tabs
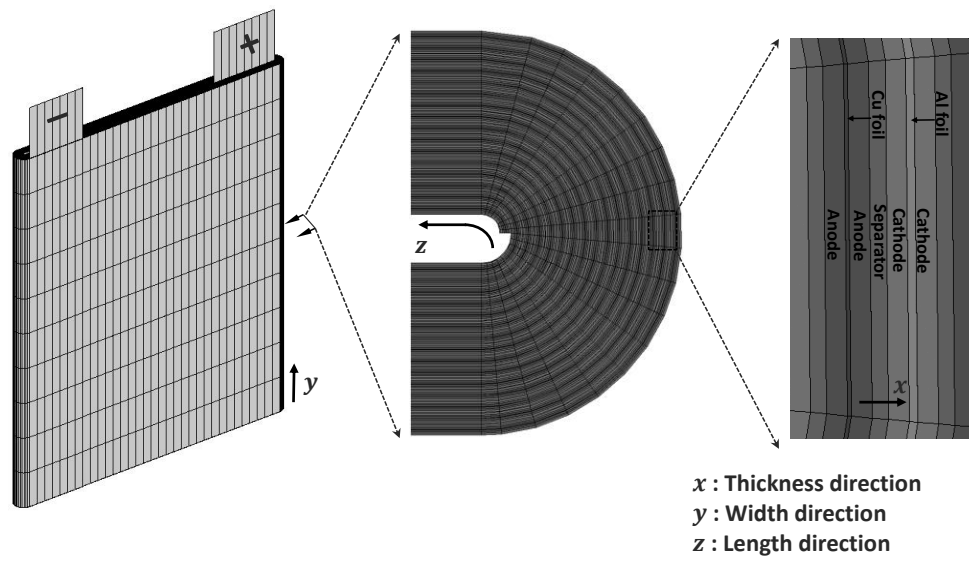
x : Thickness direction
y : Width direction
z : Length direction

Figure 3-2: Computational mesh of a large-format spirally wound cell
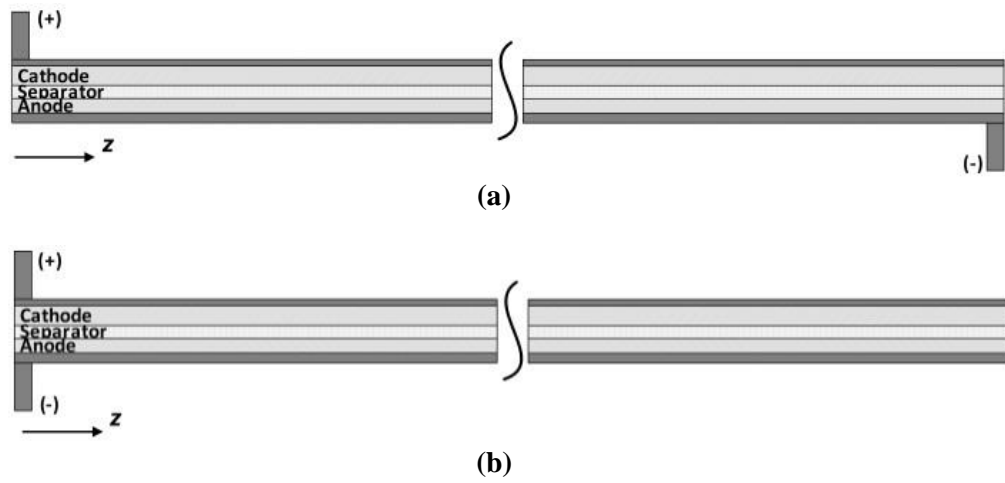
Figure 3-3: Schematic of the unwound Li-ion cell with one pair of tabs: (a) Counter-located tab design (CU-design); (b) Co-located tab design (CO-design) (The drawing is not to scale.)
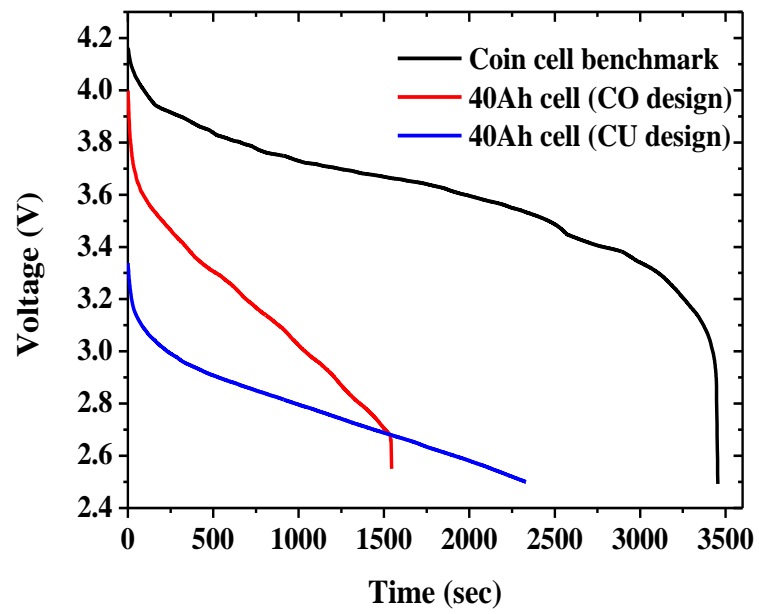
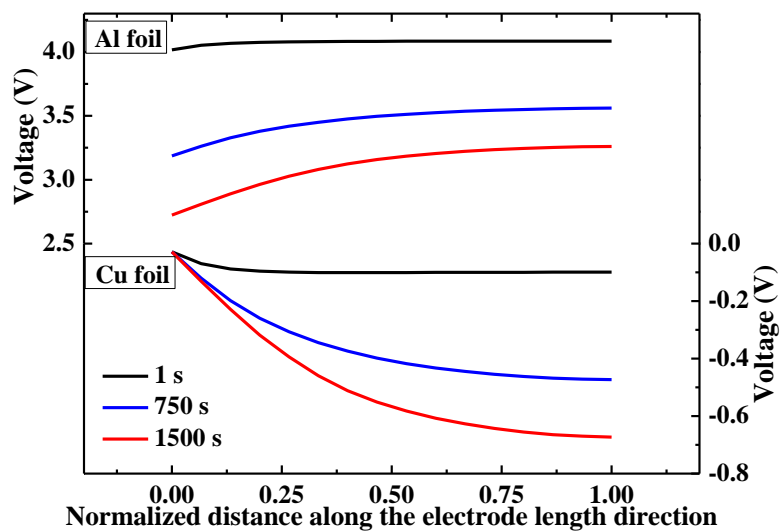**Figure 3-4**: Simulated 1C discharge curves of baseline cases and the comparison with coin cell benchmark.

(a)
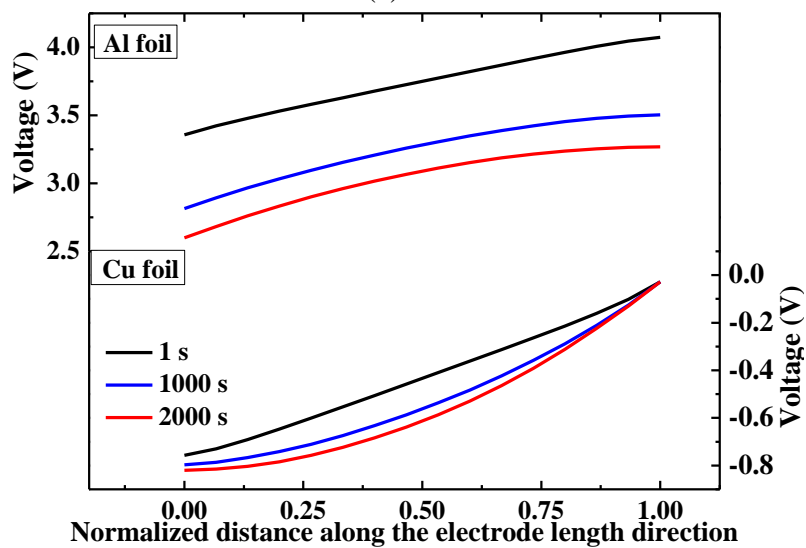
(b)

Figure 3-5: Solid potential distribution on current collectors along the electrode length direction: (a) CO design cell; (b) CU design cell.
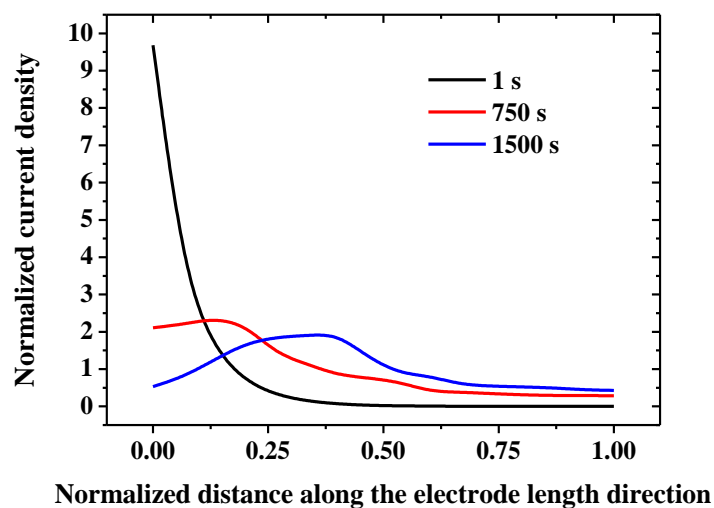
(a)
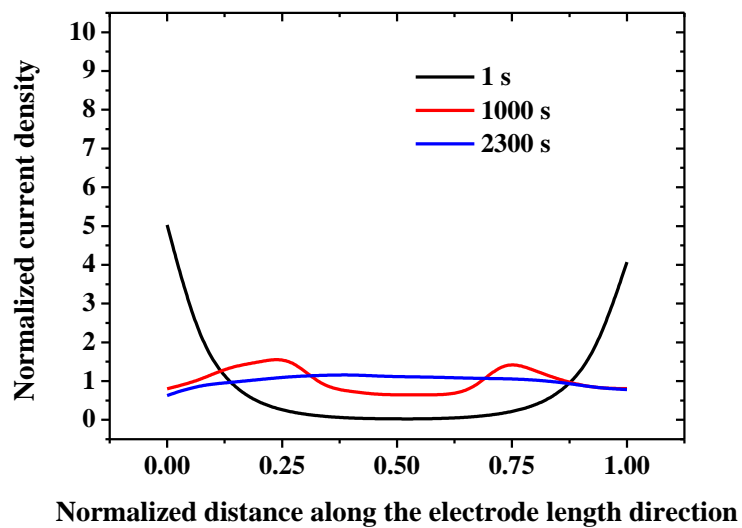
(b)

Figure 3-6: Current density distribution on current collectors along the electrode length direction: (a) CO design cell; (b) CU design cell.
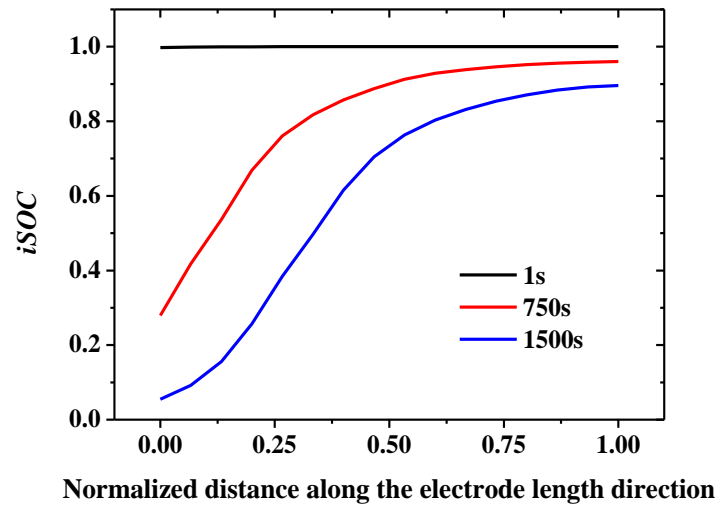
(a)
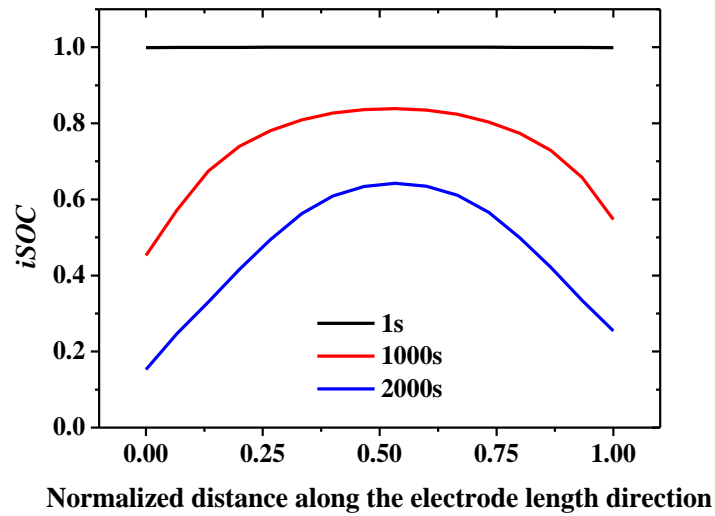
(b)

Figure 3-7: Local **SOC** distribution along the electrode length direction: (a) CO design cell; (b) CU design cell.
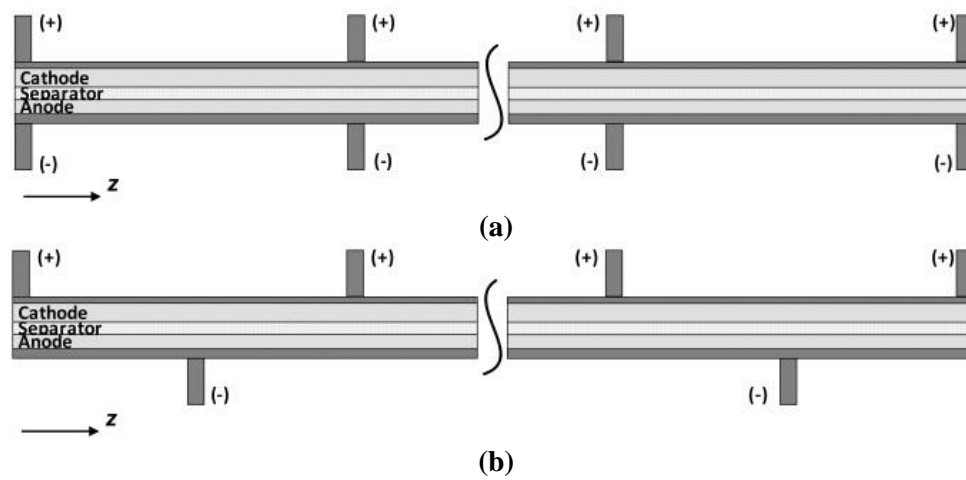
Figure 3-8: Multiple-tab configuration for the large-format Li-ion cell: (a) CO-design; (b) CU-design. (The drawing is not to scale.)

(a)

(b)
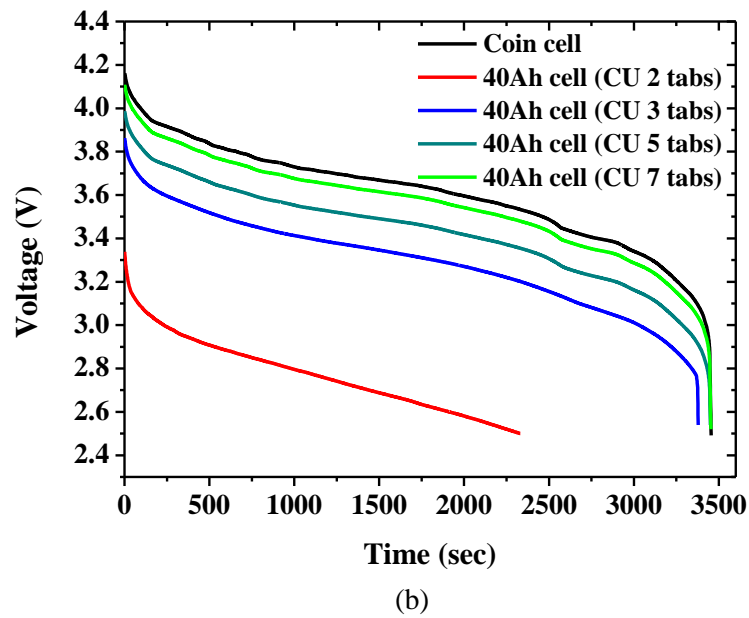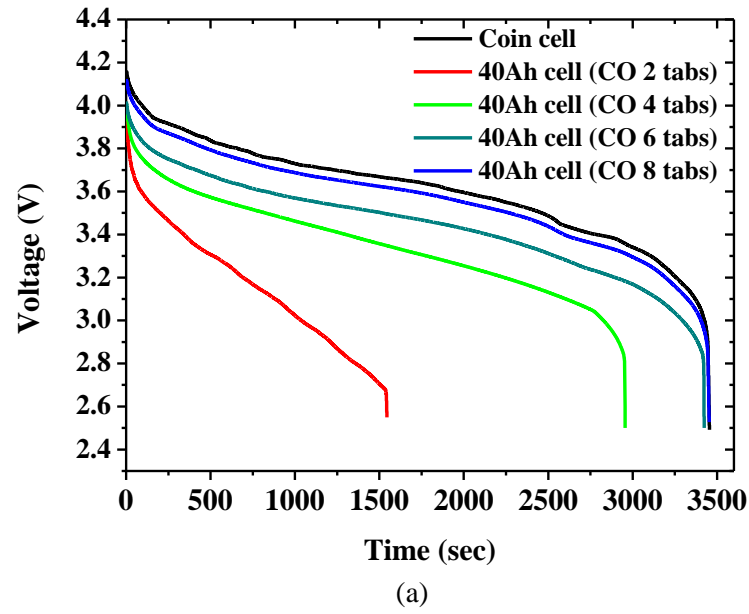
Figure 3-9: Comparison of discharge performance among different cell designs: (a) CO design cell; (b) CU design cell.
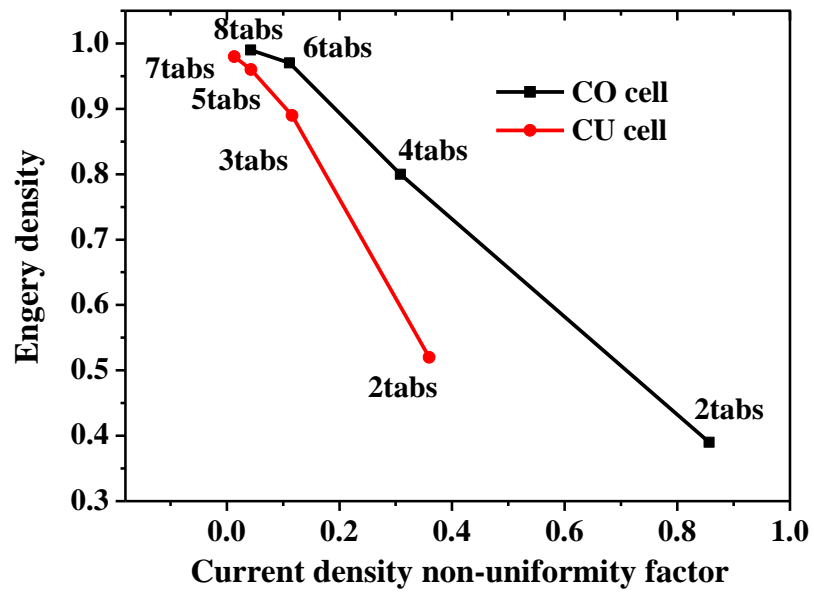
Figure 3-10: Relationship between cell's energy density and the current density non-uniformity. The energy density is for 1C discharge process and is normalized by the coin cell energy density, i.e. the maximum achievable energy density with the battery materials used.

Chapter 4

Modeling of nail penetration process in large-format Li-ion cells

4.1 Introduction

With the increasing interest in large-format Li-ion batteries for automotive applications, safety has become a primary concern due to the high energy density of Li-ion batteries and wide-ranging working conditions for electric vehicles compared with electronic applications. Safety must be maintained for electric vehicles. Even a single accident due to battery failure could turn public opinion against electric mobility and set back industry development for months or years [78].

Several abusive conditions having the potential to cause safety issues for Li-ion batteries have been reviewed in Chapter 1. Typical examples of battery abusive conditions are: internal short-circuit, external short-circuit, over-charging and over-heating. Internal short-circuit in Li-ion batteries is usually caused by manufacturing defect and is intrinsically more hazardous than other abusive conditions.

Nail penetration tests have been widely adopted by battery manufacturers to emulate the internal short-circuit process in Li-ion cells. In a nail penetration test, an electrically conductive rod (e.g. stainless steel rod) with its end tapered to a sharp point is used to pierce through the testing cell. The typical nail diameters range from 3 mm to 20 mm and the penetration speed is typically 8 cm/s [79]. The orientation of the penetration should be perpendicular to the cell electrodes. Several important variables including cell voltage, cell surface and internal temperatures and video monitoring for the duration of the test should be measured and recorded.

The result of several nail penetration tests have been documented in literature. The details about these tests are reviewed in Chapter 1. During the nail penetration process, large amount of current passing through the cell and the nail produces enormous amount of heat generation, easily triggering exothermic reactions of active materials and electrolyte and leading to thermal runaway. Large-format batteries are more vulnerable to thermal runaway because of its high energy content.

A common problem of those experimental investigations involving nail penetration tests is the poor reproducibility of the test results. A main reason is lack of basic understanding of electrochemical and thermal transport processes during nail penetration. Another reason may be that it is difficult to control the effective shorting resistance induced during the process of nail piercing through the cell. The effective shorting resistance is determined by the intrinsic resistance of the nail material and the contact resistance created by the imperfect contact of the nail and cell body, as illustrated in Fig. **2-9**. The intrinsic nail resistance is easy to calculate according to the nail diameter and conductivity. However, the contact resistance is difficult to quantify and is a complex function of nail diameter, penetration speed, cell and nail surface properties, etc.. To date, there hasn't been any experimental study in the literature trying to measure the contact resistance or provide clues on how to precisely control the contact resistance during the nail penetration process.

Another problem with nail penetration tests is that the experimental observations provide few insights into the fundamental mechanisms, such as the heating mode, internal species distribution, electrochemical and thermal coupling, etc., of the problem. Also, it is expensive and dangerous to perform experimental parametric studies by nail penetration.

Therefore, it is imperative that fundamental models are developed and utilized to explore the physics of nail penetration in a Li-ion cell and study the problem in tandem with the experimental investigations.

4.2 Approach

As mentioned above, in nail penetration tests, the typical penetration speed is 8 cm/s. Since most Li-ion cells have a thickness less than several centimeters, this means the nail will penetrate through the cell in less than 1s for most of the cases. Therefore, in the current study, we only consider the full penetration scenario.

There are two types of design for large-format Li-ion cells, namely spirally wound design and prismatic stacked-electrode design. In this work, we focus on the stacked-electrode design cells since they feature high performance and have become more popular in the automotive applications. In these cells, a number of electrode plates consisting of Cu foils coated with anode electrode material, Al foils coated with cathode material and separators are stacked together to achieve the desired cell capacity. Each plate in the cell has a positive tab and a negative tab, and the tabs are bundled and welded to their respective terminals or to the cell case.

When the stacked-electrode design cell is fully penetrated by the nail, each electrode plate is shorted independently by a part of the nail, as shown in Fig. **4-1**. No current flows through the tabs between different electrode plates. Since the cell thickness is much smaller than the cell length and cell width, we can assume that all electrode plates are identical in terms of electrochemical behavior. Therefore, only one electrode plate is used for solving the electrochemical model (Eq. **2-23** – Eq. **2-26**). The short-

circuit boundary condition is applied at the location of nail penetration, as described in **2.6**. The thermal calculation, on the other hand, uses full 3D geometry. The heat generation obtained from the electrochemical calculation is applied to all electrode plates.

4.3 Results and discussion

Fig. **4-2** illustrates the computational mesh for the baseline large-format cell. The cell is 13 cm in height (y-dir) and 8 cm in width (z-dir). It consists of 26 electrode plates, stacking together in the cell thickness direction (x-dir). The total cell thickness is 2.6 cm. Each plate has a Cu foil, an anode electrode, a separator, a cathode electrode, and an Al foil. The Cu and Al foils are double-side coated with anode material and cathode material, respectively. The tabs are welded outward on foils at the top edge of the cell and are clamped together. The anode and cathode tabs have the same size, which is 2 cm in width and 1 cm in height. The cell has a graphite based anode and NCM based cathode. The cell nominal capacity is 5 Ah. Other parameters of the cell are listed in Table. **4-1**. For the baseline case, the nail is penetrated at the center of the y-z plane. The mesh is refined in the region near the nail to capture the large variable gradients. Mesh-independent study has been carried out and the total mesh number is 419,464.

4.3.1 Model validation

Experimental validation of the nail penetration modeling is extremely difficult, largely due to the imperfect testing techniques currently used in the nail penetration experiments. Also, in the literature, a lot nail penetration tests are performed on

commercial Li-ion cells from different manufacturers. The different cells usually have different design parameters, including the form factor, enclosure material, terminal shape and arrangement, safety devices. The influence of these design parameters on the cell thermal and electrochemical behaviors during nail penetration process is largely unknown, which makes quantitative comparison between modeling results and experimental data almost impossible. As an initial effort, in this work, we only qualitatively validate our modeling results against some typical short-circuit experimental results.

Fig. **4-3** shows some of the typical short-circuit experimental results from literature. Although the cell parameters and the short-circuit scenarios are different among these experiments, a common condition is that the short-circuit resistance is much smaller than the cell internal resistance in all of these tests. Under such condition, the electrochemical and thermal responses of the nail penetration process become similar to that of external short-circuit process, because the heat generation in the nail is negligible compared with the heat generation in the cell ($I^2 R_s \ll I^2 R_i$). The external short-circuit test results can then be used to calibrate the nail penetration modeling results.

It can be seen from Fig. **4-3** that a common trend in terms of the current and voltage profiles for these short-circuit test is that there is a very high in-rush current (~30-70 C-rate) upon the beginning of short-circuit, followed by a rapid decrease of the current and voltage in the first tens of seconds period of time, and a much slower decay of the current and voltage in the subsequent few minutes of the short-circuit. Since for all cases, the short-circuit resistance is much smaller than the cell internal resistance, the current and voltage responses are solely determined by the cell internal processes, including

reaction kinetics, ohmic resistance, Li+ transport in the electrolyte and Li+ transport in the active material particles.

Fig. **4-4** shows the comparison of model and experimental results for the short-circuit of Li-ion cell. The experiment was performed by externally shorting a 40 mAh coin cell with a small shut resistor. The resistance of the shut resistor is 26 mΩ. The detailed description of the experimental techniques and configurations can be found in Ref. **[80]**. For the modeling case, the geometry of the 5 Ah cell was used. To make the 5Ah cell case equivalent to the 40 mAh cell experiment, a 0.208 mΩ shorting resistance was used in the simulation (5 Ah / 40 mAh = 26 mΩ / 0.208 mΩ). All other modeling parameters are the same as those listed in Table. **4-1**

Fig. **4-4** illustrates that the modeled current profile is qualitatively comparable to the experimental data. Specifically, a large in-rush current is induced upon the start of short-circuit. This large current cannot be sustained and will decrease rapidly to a lower current within ~20 s after the shorting. The cell then discharges at this limiting current until the depletion of its electrochemical energy and the discharge current gradually decreases to zero. The figure demonstrates that the current model is capable of capturing the highly non-linear electrochemical dynamics of the short-circuit process.

4.3.2 Parametric study

4.3.2.1 Effect of shorting resistance

As discussed previously in 2.6, the effective shorting resistance is controlled by the shorting contact resistance, which is caused by the imperfect contact between the

penetrated nail and the cell material. Its value should be a complex function of material

properties of nail and cell, penetration speed, nail diameter, nail surface properties, etc..

To date, there has not been an effective method developed to precisely control the

shorting contact resistance during the nail penetration process. Therefore, it is necessary

to conduct numerical simulations to study the effect of a wide range of shorting contact

resistance.

For full nail penetration scenario, the effective shorting resistance is calculated by

$$R_s = R_{ct} = \frac{\overline{R_{ct}}}{\pi d H} \tag{4-1}$$

where $\overline{R_{ct}}$ is the area specific contact resistance, d the diameter of the nail, and H the

length of the nail inside the cell (equals to the cell thickness). In the following

simulations, the nail diameter is fixed at 4 mm. By varying the $\overline{R_{ct}}$, we can obtain a

wide range of effective shorting resistance. Other parameters are listed in Table **4-2**. The

parameter studies in the following sections are all based on the baseline parameters listed

in Table **4-2**.

Fig. **4-5** shows the current and voltage responses during the nail penetration

process. Four levels of effective shoring resistance are chosen for comparison. It can be

seen from Fig. **4-5(a)** that the cell responses are very different for different effective

shorting resistances. At small resistance, i.e. Rs = 0.2 mΩ, the discharge process has three

stages. In the first stage, the in-rush current jumps to 87.4 C at the beginning of shorting.

However, the cell cannot hold up this high in-rush current and the current rapidly

decreases to ~20 C in about 20 s. The second stage features a steady discharge of the cell

at ~20 C from 20 s to 180 s. At this stage the discharge current gradually decreases due to

the reduction of cell electrochemical energy. After 180 s, the discharge enters the third

stage, where a more rapidly current drop occurs. The current eventually drops to around zero indicating the full discharge of the cell.

The in-rush current decreases as larger effective shorting resistance is used. The in-rush current is 14 C, 3.8 C, and 0.8 C for R_s = 50 mΩ, 0.2 Ω, and 1.0 Ω, respectively. As shown in Fig. **4-5(a)**, the lower the in-rush current, the more the discharge process resembles the constant rate discharge. Therefore, at large shorting resistance, the discharge of the cell is controlled by the load, which is the penetrated nail in this case.

The cell voltage profiles are shown in Fig. **4-5(b)**. The cell voltage is measured between the positive and negative terminals. As can be seen in the figure, the cell voltage has an instantaneous drop from the OCV to a lower value at the beginning of shorting. The smaller of the effective shorting resistance, the larger of the drop. The initial voltage drop for R_s = 0.2 mΩ, 50 mΩ, 0.2 Ω and 1.0 Ω is 3.28 V, 1.34 V, 0.55 V and 0.22 V, respectively. After the initial drop, the voltage profile follows the similar trend of the current profile. It gradually decreases as the discharge process goes on. Since the cell voltage can be measured during nail penetration experiments, one may be able to quantify the effective shorting resistance from the cell voltage response during the experiment. For example, if the cell voltage drops to very small value immediately after shorting, it means a very small shorting resistance is caused by the penetration process. On the other hand, if the cell voltage does not change much from the OCV, the shorting resistance must be relatively large. This definitive relationship between nail contact resistance and cell voltage response during nail penetration, as discovered in the present simulation work for the first time, could provide an excellent means to measure the short contact resistance.

Fig. **4-6** shows the Li+ concentration distribution along the cell thickness direction in the electrolyte, for the case of R_s = 0.2 mΩ. At t=0 s, the cell is at equilibrium state and uniform distribution of Li+ concentration is assumed. As the cell begins to discharge as a result of nail penetration, Li+ is released from the carbon material into the electrolyte at the anode, and Li+ is inserted to the metal oxide material from the electrolyte in the cathode. A Li+ concentration gradient begins to form across the cell thickness direction. The Li+ generation and consumption rate is proportional to the reaction current density, as shown in Eq. **2-25**. The high in-rush current makes the Li+ in the cathode electrolyte consumed very quickly and become depleted. As shown in Fig. **4-6**, after 20 s of shorting, Li+ concentration in the cathode electrolyte drops to almost zero. The reduction of Li+ concentration in electrolyte will restrain the shorting current by two mechanisms. Firstly, the ionic conductivity is a strong function of Li+ concentration in electrolyte. As illustrated in Fig. **2-3(c)**, the ionic conductivity decreases as the decrease of Li+ concentration. Therefore, as the Li+ becomes depleted in the cathode electrolyte, the ohmic loss becomes larger. Secondly, the exchange current density for the Li+ intercalation reaction decreases as the decrease of Li+ concentration in electrolyte, as shown in Eq. **2-4**. As a result, the cell internal resistance increases rapidly and the shorting current decreases sharply to match the increased internal resistance.

Fig. **4-7(a)** and Fig. **4-7(b)** show the Li+ concentration distribution in the active material particles of anode and cathode, respectively. The plot is normalized so that the non-dimensional concentration varies between 0.0 and 1.0, indicating fully discharged and fully charged states, respectively. When the cell discharges, Li+ is de-intercalated from the anode particles and intercalated into the cathode particles. It is shown that in the

case of Rs=0.2 mΩ, within the 300s time frame, the Li+ is almost fully extracted from the anode particles and inserted to the cathode particles. This means the cell is almost fully discharged in 300 s, releasing all of its energy in the form of heat.

Fig. **4-8** and Fig. **4-9** show Li+ distribution for the large shorting resistance case, Rs = 0.2 Ω. Compared with the small resistance case, no Li+ transport limitation is found in electrolyte or active material particles. Specifically, Fig. **4-8** shows that the Li+ concentration gradient is much smaller than that shown in Fig**. 4-6**. The Li+ distribution in the solid particles shown in Fig. **4-9** also indicates that the cell only discharges a small portion of its energy within the 300 s time frame.

The above analysis reveals that the effective shorting resistance of the nail penetration process has a strong impact on the cell discharge behavior. Since the cell electrochemical performance and thermal response are closely coupled, the effective shorting resistance also has a significant influence on the cell thermal behavior. In the present simulation, both the cell surface temperature (T_{surf}) and the temperature at the cell and nail interface ($T_{cell/nail}$)) are monitored. Fig. **4-10** shows the $T_{cell/nail}$ during the nail penetration process as a function of effective shorting resistance. This temperature is an indication of the maximum temperature in the cell and can be used to check whether exothermic reactions have already occurred inside the cell. From Fig. **4-10**, two regimes can be distinguished in terms of heating modes. At small shorting resistance ($R_s < R_i$), the cell discharge is controlled by the internal processes such as Li+ transport in the electrolyte and interfacial electrochemical kinetics. This results in global heating in cell because the internal processes occur everywhere of the electrode. In this regime, as the shorting resistance decreases, the $T_{cell/nail}$ also decreases. But when the shorting

resistance is smaller after certain value, the $T_{cell/nail}$ cannot be reduced anymore. This is because that the shorting resistance is negligible compared with cell internal resistance, and has no influence on the heat generation. At large shorting resistance ($R_s > R_i$), on the other hand, the cell discharge is dominated by the ohmic resistance of the nail. As the effective shorting resistance becomes larger, the shorting current reduces and the resulting heating rate decreases. Therefore, the $T_{cell/nail}$ decreases linearly in this regime. Also, because $R_s > R_i$, the heat generation is mainly contributed from the localized ohmic heating from the nail. The $T_{cell/nail}$ reaches its peak value when the effective shorting resistance is close to the cell internal resistance. This corresponds to the most dangerous scenario. The cell will undoubtedly go into thermal runaway at this condition.

Fig. **4-11** and Fig. **4-12** display the 3D temperature distribution at different time instants for the small shorting resistance case and large shorting resistance case, respectively. The difference between global and local heating modes can be clearly seen by comparing the two figures.

The temperature profiles for the three cases, i.e. R_s = 0.2 mΩ, R_s = 50 mΩ and R_s = 0.2 Ω, are displayed in Fig. **4-13**. On each figure, both the $T_{cell/nail}$ and T_{surf} are plotted. It can be seen from Fig. **4-13 (a)** that at small shorting resistance, the $T_{cell/nail}$ and T_{surf} are close, indicating global heating. For the medium shorting resistance case as shown in Fig. **4-13 (b)**, the $T_{cell/nail}$ jumps to very high value at the beginning of penetration, while the T_{surf} is still very low. As the penetration proceeds, $T_{cell/nail}$ quickly decreases due to the reduction of heat generation and heat dissipation through the nail and cell surface. The heating mode transitions from local heating to global heating,

indicated by the fact that the difference between $T_{cell/nail}$ and T_{surf} gets smaller. In comparison, **Fig. 4-13(c)** illustrates the local heating case, where $T_{cell/nail}$ is always much higher than T_{surf}.

4.3.2.2 Effect of nail diameter

Eq. **4-1** shows that the effective shorting resistance is not only a function of area specific contact resistance, but also a function of nail diameter. The nail diameter also influences the nail thermal mass. Therefore, it is necessary to explore the nail diameter effect on the penetration process.

Fig. **4-14** shows the effective shorting resistance as a function of nail diameter. Apparently, increasing the nail diameter will reduce the shorting resistance, as the contact area increases with the nail diameter. As a result, the in-rush current increases as the increase of nail diameter, as displayed in Fig. **4-15**. It is worth noting that the increase of the in-rush current is not a linear function of nail diameter. This is because as the shorting resistance drops with the nail diameter increase, the cell internal resistance becomes more important in affecting the in-rush current.

Fig. **4-16** illustrates the $T_{cell/nail}$ profiles for different nail diameters. It is evident that the nail diameter has a significant effect on the cell thermal response during the nail penetration process. For all cases, the $T_{cell/nail}$ has a sharp increase at the beginning of shorting. Smaller nail diameter results in higher temperature jump and vice versa. Although the in-rush current reduces as the decrease of nail diameter, small diameter nail is less efficient in terms of dissipating heat as compared to large diameter nails.

Therefore, using nail with smaller diameter in penetration tests is more likely to cause thermal runaway.

Fig. **4-17** shows the variation of $T_{cell/nail}$ rise as a function of nail diameter. From the figure, it is evident that using large diameter nail will decrease $T_{cell/nail}$ rise during the nail penetration process. Since the lowest onset temperature of the various exothermic reactions is around 120 ^{o}C, the onset temperature for the SEI layer decomposition reaction in anode, we can safely draw the conclusion that if $T_{cell/nail}$ is below 120 ^{o}C during the penetration, the cell will be absolutely safe and not go to thermal runaway.

Similar to the shorting resistance effect, the nail diameter also has a significant influence on the heating mode. Fig. **4-18** displays $T_{cell/nail} - T_{surf}$ versus the nail diameter. $T_{cell/nail} - T_{surf}$ is used to characterize the heating mode. If the value is small, it means all parts of the cell are heated up uniformly, which indicates global heating. If small value of $T_{cell/nail} - T_{surf}$ is presented, there should be some locally concentrated hot spot within the cell. Here we define 200 ^{o}C as the threshold temperature to differentiate global and local heating regime. As indicated in Fig. **4-18**, $T_{cell/nail} - T_{surf}$ decreases as the increase of nail diameter and vice versa. The switch from local heating to global heating occurs when the nail diameter is around 9 mm.

Fig. **4-17** and Fig. **4-18** tell us that using large diameter nail will induce global heating and reduce the $T_{cell/nail}$ rise, which makes the cell more likely to pass the nail penetration test. Fig. **4-19** shows the 3D temperature contour for cells with different nail diameters. The difference between global and local heating can be clearly observed.

4.3.2.3 Effect of nail thermal conductivity

In most nail penetration tests, stainless steel is the typical material used for nails. As mentioned above, the electrical conductivity of the nail material has negligible effect on the effective shorting resistance. However, the nail thermal properties, particularly the nail thermal conductivity, will play an important role in the cell thermal response during the penetration process.

Fig. **4-20** illustrates the $T_{cell/nail}$ profile for nails with different thermal conductivities. The shorting resistance is kept constant for all cases. Therefore the cell electrochemical behavior is identical for all cases. It is obvious that the nail thermal conductivity is a critical parameter to impact the cell thermal response. The higher the thermal conductivity, the lower the $T_{cell/nail}$ rise and vice versa. Using nails with high thermal conductivity will therefore facilitate the cell to pass the nail penetration test.

4.3.2.4 Effect of nail penetration location

All above simulation cases are carried out with the nail penetration located at the center of the cell plane. It is necessary to explore whether the nail penetration location will influence the results significantly.

Fig. **4-21** shows the computational mesh for the three cases with the nail penetration located at center, top and corner of the cell, respectively. All other parameters remain the same as the baseline case. Fig. **4-22** displays the $T_{cell/nail}$ profiles for the three cases. It can be seen from the figure that there is not much difference between the case of penetrating at the center and at the top edge. The $T_{cell/nail}$ profiles are very close

for these two cases. However, for the case of penetrating at the corner, the temperature rise is much higher than the other two cases. These modeling results are in line with the experimental observations reported in Ref. **[26]**. The reason for the penetration at the corner being more dangerous is that the in-plane heat dissipation is less efficient than the other two cases.

4.3.2.5 Effect of cell capacity

The above parameter studies use 5 Ah prismatic Li-ion cell, which is typical cell size used in plug-in hybrid electric vehicles (PHEV). As hybrid electric and electric vehicles (HEV/EV) become more and more popular, cells with larger capacity are being developed and utilized in these applications. In this section, cells with different capacities are studied to explore the capacity effect on the nail penetration process. We change the cell capacity based on the 5 Ah cell. The cell footprint area (8 cm $\times$ 13 cm) and electrode/separator/foil thickness are kept unchanged, and we change the number of electrode plates to get the desired cell capacity. For example, the baseline case 5 Ah cell has 26 electrode plates. The 10 Ah cell is therefore made of 52 electrode plates that are same as those used in the 5 Ah cell.

Fig. **4-23** shows the $T_{cell/nail}$ profiles for different capacity cells. It is evident that cell with larger capacity has higher temperature increase and will be more likely to go to thermal runaway. Fig. **4-24** displays the $T_{cell/nail}$ as a function of cell capacity. It is obvious that large capacity cells are less tolerable to the short-circuit condition and are therefore more dangerous to use in real applications.

4.4 Conclusion

Nail penetration is a widely used method to emulate the internal short-circuits process in Li-ion cells. A common problem of those experimental investigations involving nail penetration tests is the poor reproducibility of the test results. The experimental observations also provide few insights into the fundamental mechanisms that govern the cell behavior during the nail penetration process. In this chapter, a comprehensive modeling study is carried out to explore the fundamental electrochemical and thermal behavior of a large-format Li-ion cell undergoing nail penetration process. Parametric study finds out that the shorting resistance has a significant influence on the cell electrochemical performance and heating mechanism during the penetration process. With small shorting resistance, the discharge rate is limited by the cell internal processes, such as the Li+ transport in the electrolyte. The heat generation from these internal processes contributes most of the total heat generation, which leads to global heating of the cell. When large shorting resistance is presented, the shorting current and voltage are controlled by the shorting resistance. The total heat generation is mainly from the ohmic heat and concentrated at the nail. Within a wide range of effective shorting resistance, it is found that the $T_{cell/nail}$ rise reaches its peak when the cell internal resistance is close to the shorting resistance. The effect of other parameters, including the nail diameter, nail thermal conductivity, penetration location, and cell capacity is also studied.

The modeling study provides clues to explain the fundamental mechanisms of the nail penetration process. It also partially explains the poor reproducibility of the nail penetration experiments results reported in literature. The shorting of the cell resulted from the nail penetration process is a highly dynamic process with strong electrochemical

and thermal coupling. The modeling shows this process is very sensitive to the various parameters of experiment. The current nail penetration testing techniques are not able to precisely control the value of these parameters, which is the main reason for the irreproducibility of the experimental results.

Table 4-1 Design parameters for the 5Ah cell

	Positive electrode	Negative electrode
Chemistry	$Li_yCo_{1/3}Ni_{1/3}Mn_{1/3}O_2$	Li_xC_6
Loading amount	12.5 mg/cm^2	6.05 mg/cm^2
Electrode thickness	78 μm	82 μm
Electrode height	13 cm	13 cm
Electrode width	8 cm	8 cm
Foil thickness	15 μm	8 μm
Separator thickness		20 μm
Electrolyte		PC-EC-DMC 1.2 M LiPF$_6$
NP ratio		1.14
No. of plates		26
Total active area		2704 cm^2
Nominal capacity		5 Ah

Table 4-2 Parameters of the baseline nail penetration case

Parameter	Value
Cell capacity	5 Ah
Penetration depth	Full penetration
Nail length outside of cell	10 cm
Nail diameter	4 mm
Area specific contact resistance	16.3 mΩ cm^2
Effective shorting resistance	50 mΩ
Nail material	Stainless steel
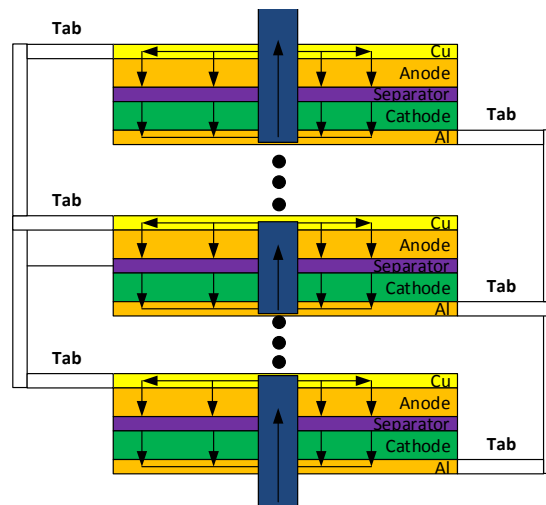
Figure 4-1: Schematic of the current flow path in the penetrated cell
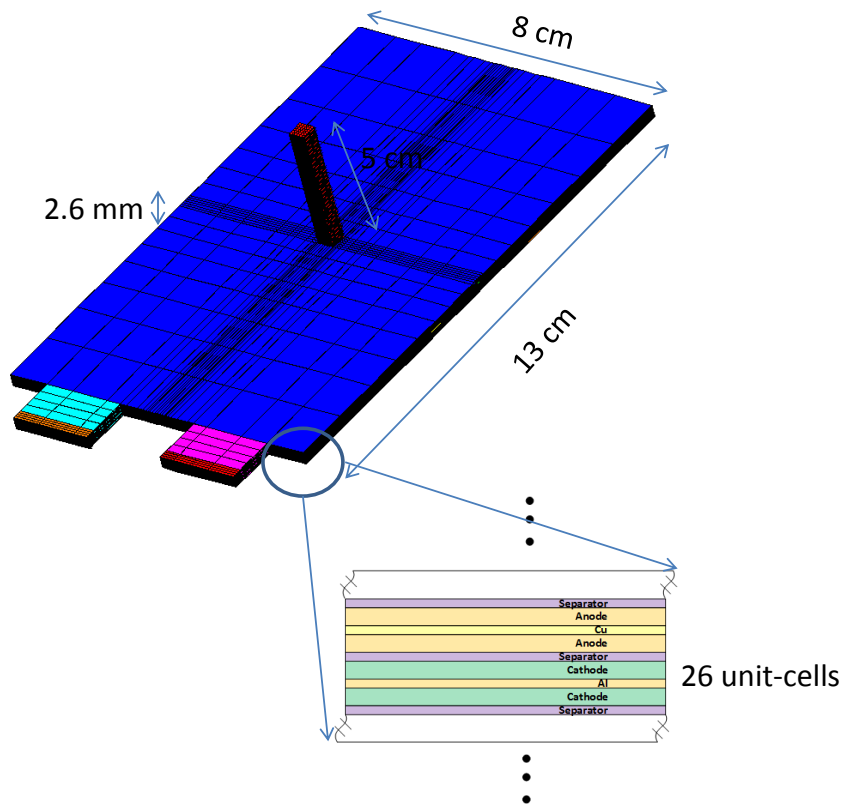
Figure 4-2: Computational mesh for the 5 Ah cell used in the nail penetration simulation
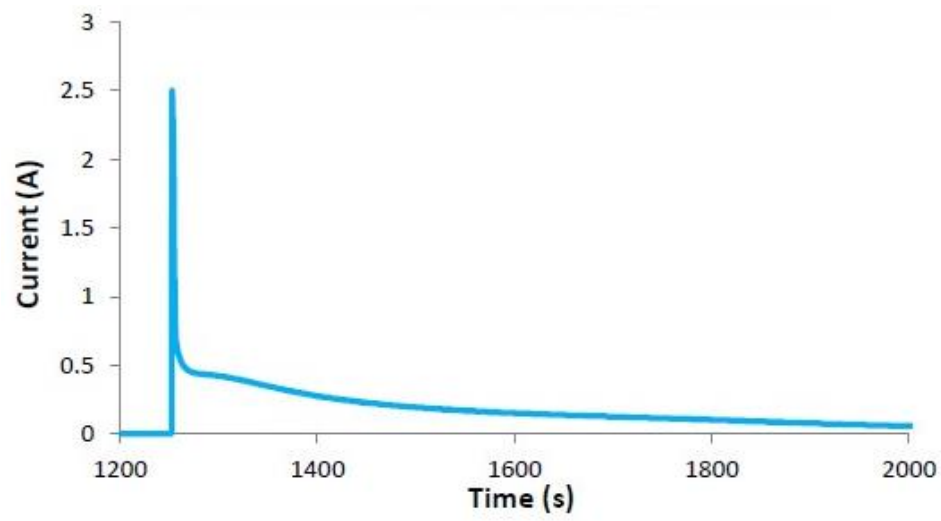
(a)
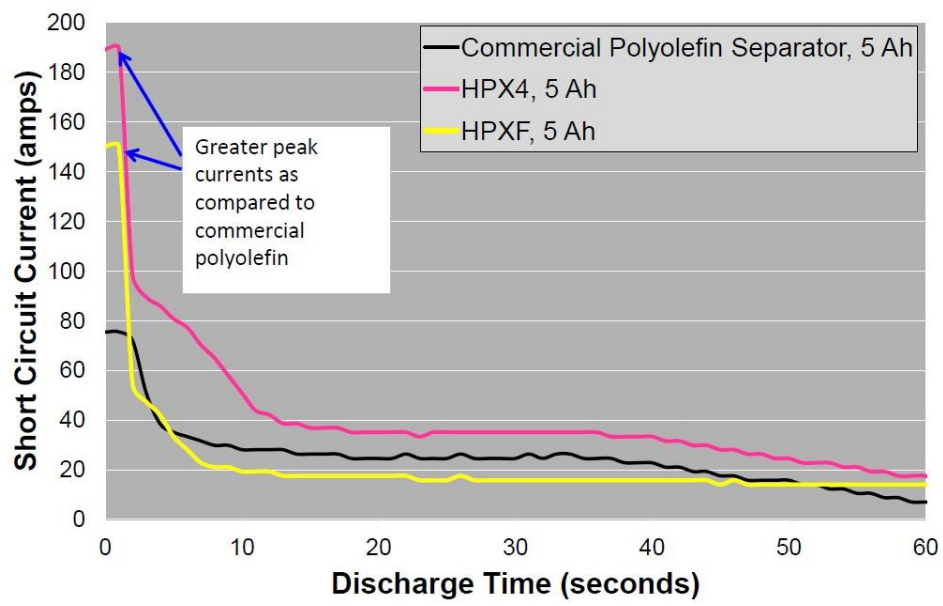
(b)
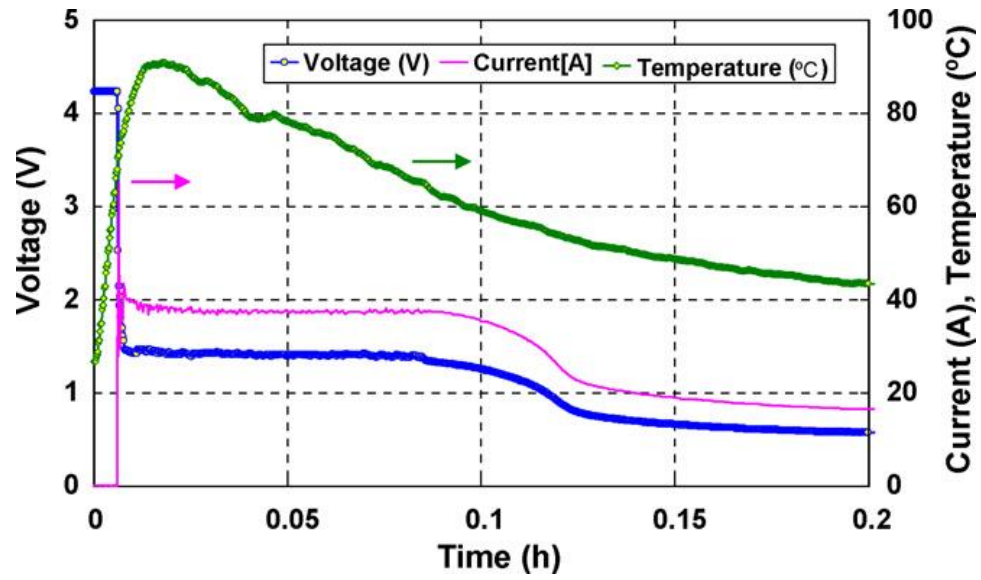
(c)
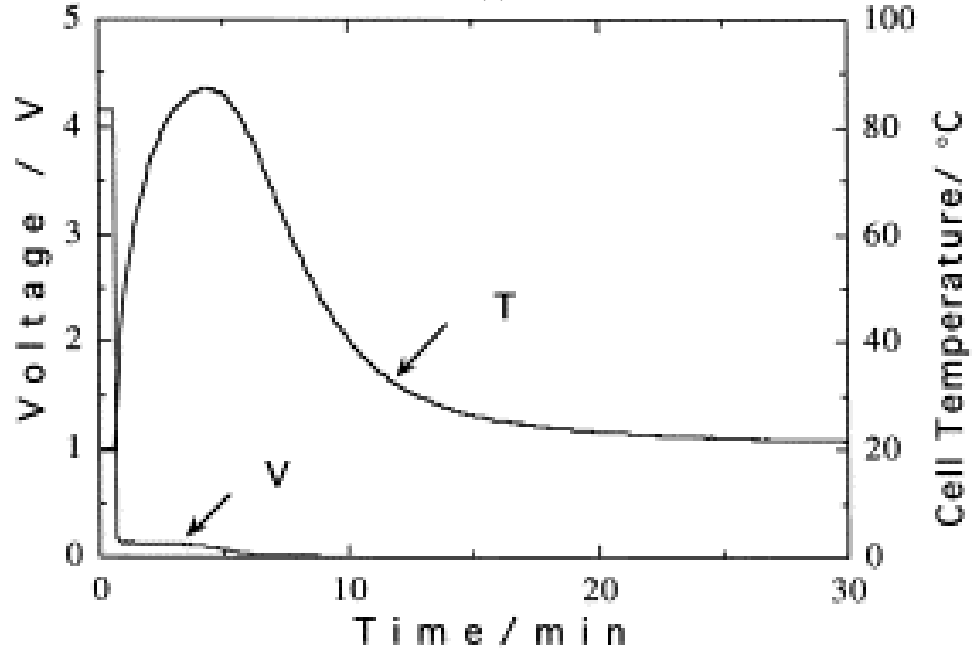
(d)

Figure 4-3: Examples of some short-circuit experimental results. (a) external short-circuit test of a 40 mAh coin cell **[80]**; (b) external short-circuit test of 5 Ah cells **[81]**; (c) external short-circuit test of a 1 Ah cell **[82]**;(d) Nail penetration test of a 500 mAh cell **[24]**.
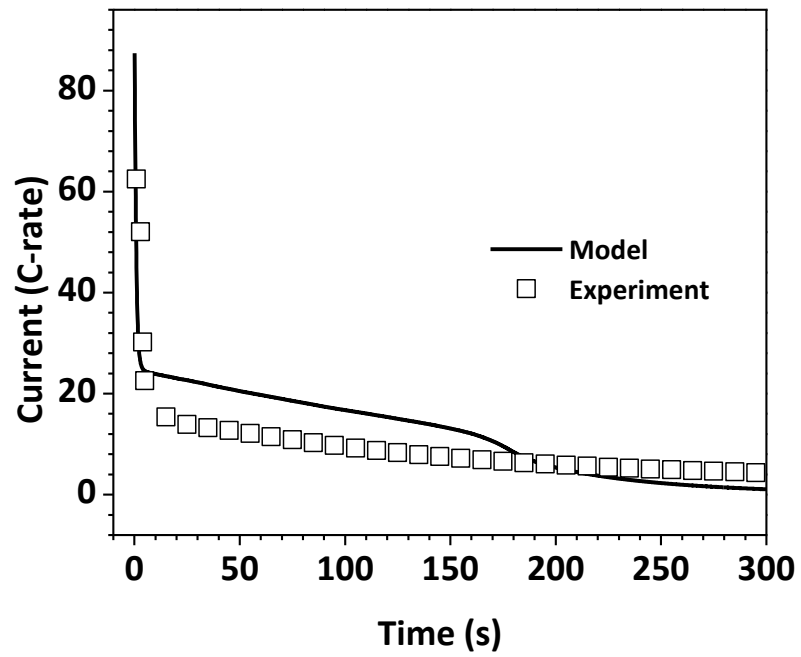
Figure 4-4: Comparison of modeling results and experimental data.

(a)

(b)
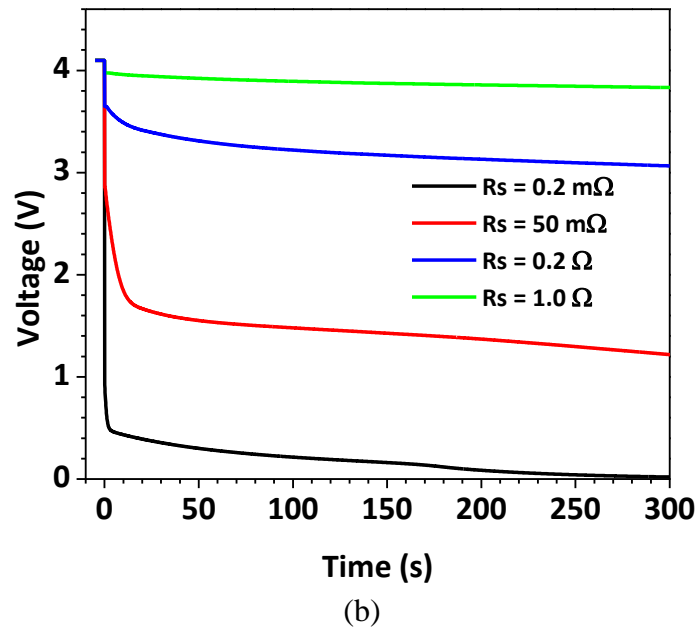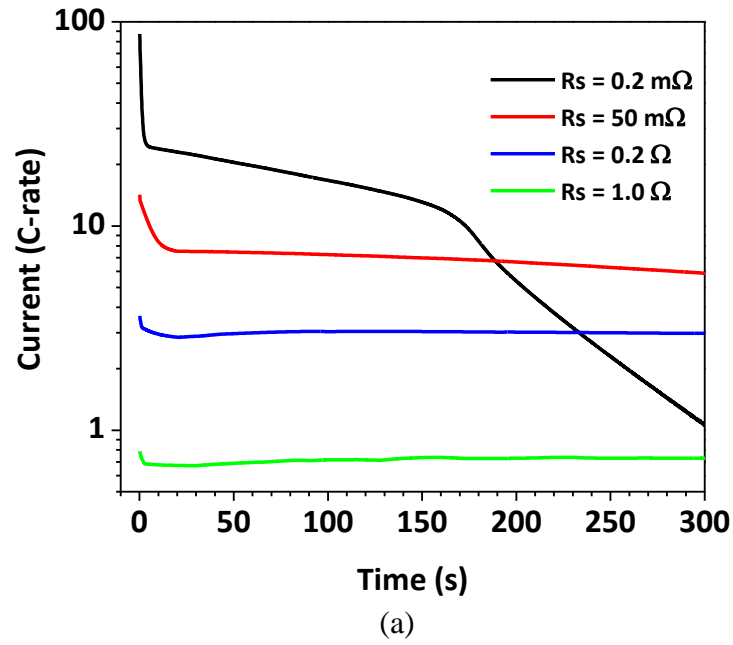
Figure 4-5: Shoring current and voltage profiles for different effective shorting resistance (a) current profiles; (b) voltage profiles.
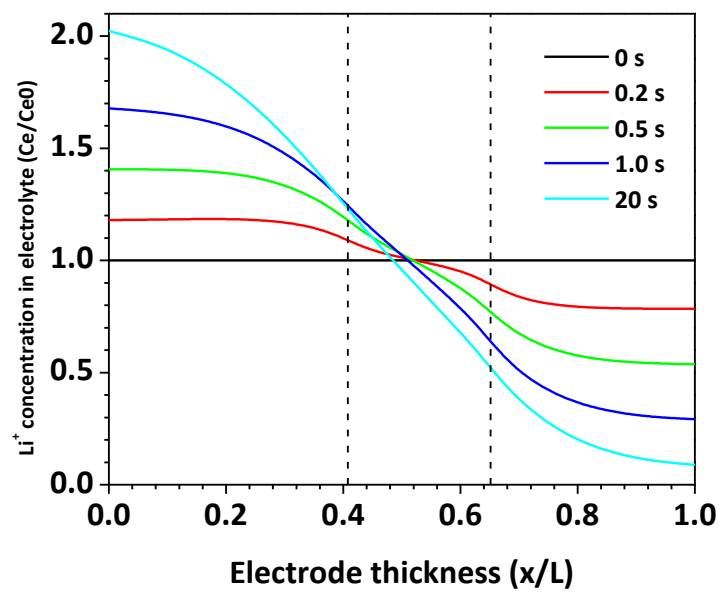
Figure 4-6: Li+ concentration distribution in electrolyte, $R_s = 0.2$ mΩ.
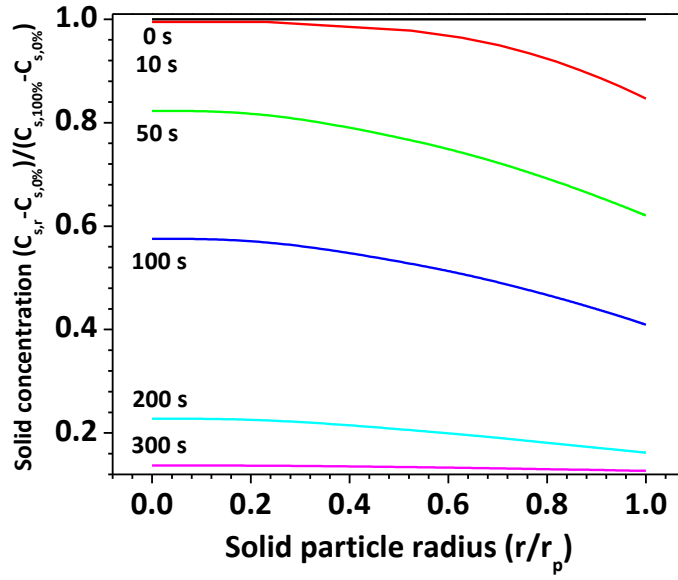
(a)
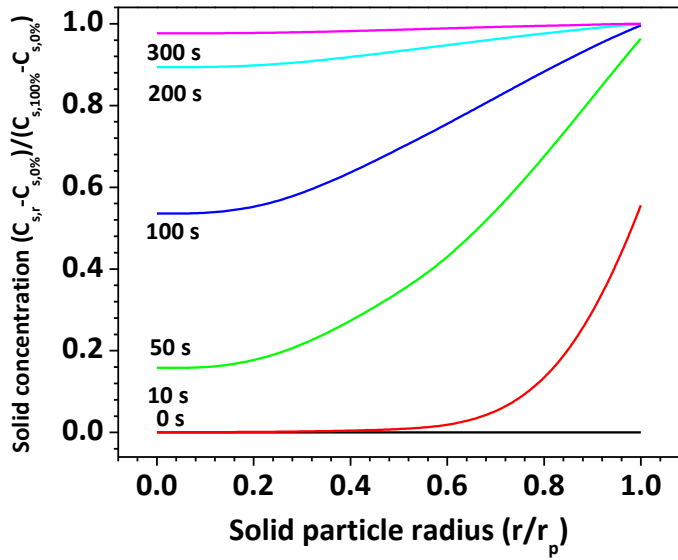
(b)

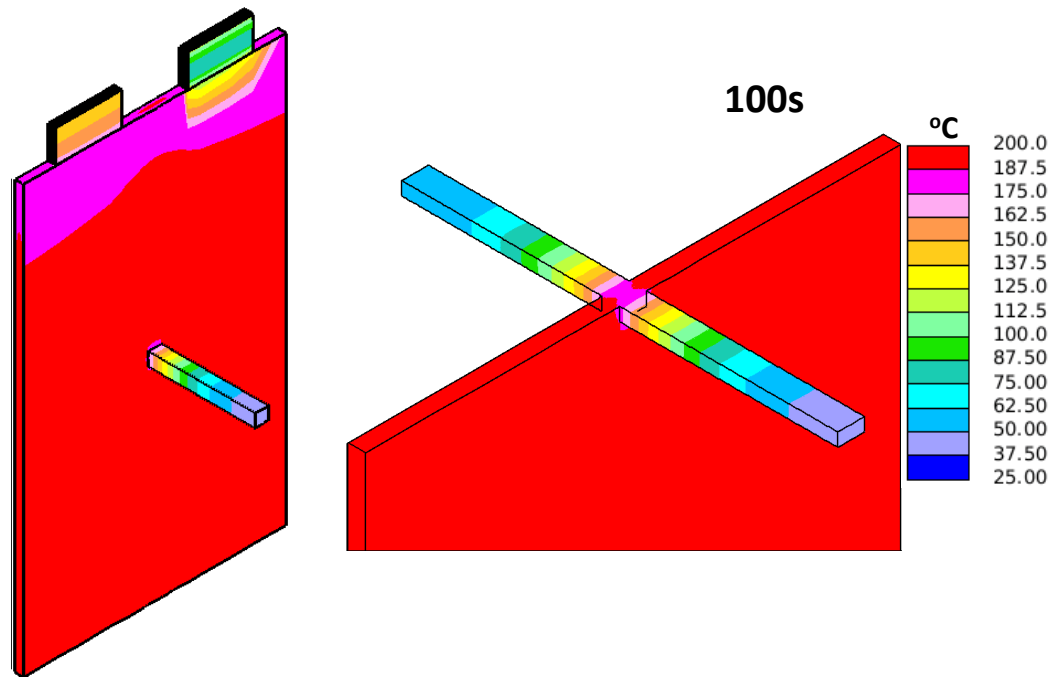**Figure 4-7**: Li+ concentration in solid material particles, $R_s = 0.2$ mΩ (a) anode; (b) cathode.
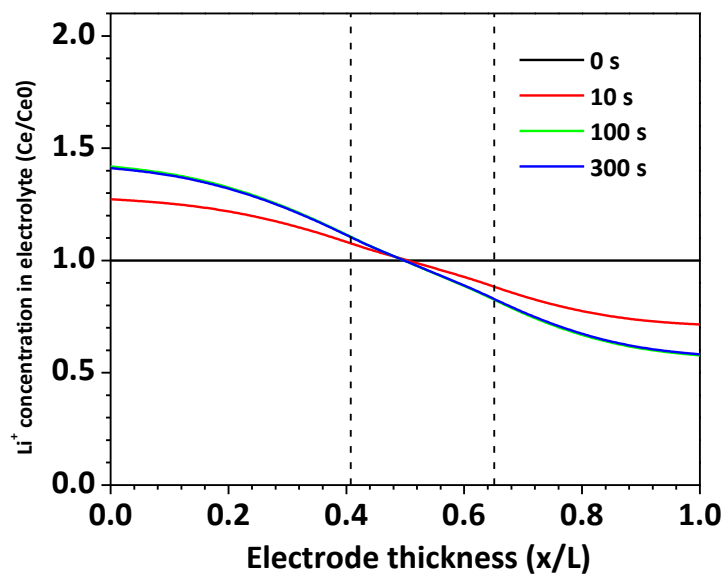
Figure 4-8: Li+ concentration distribution in electrolyte, Rs = 0.2 Ω.
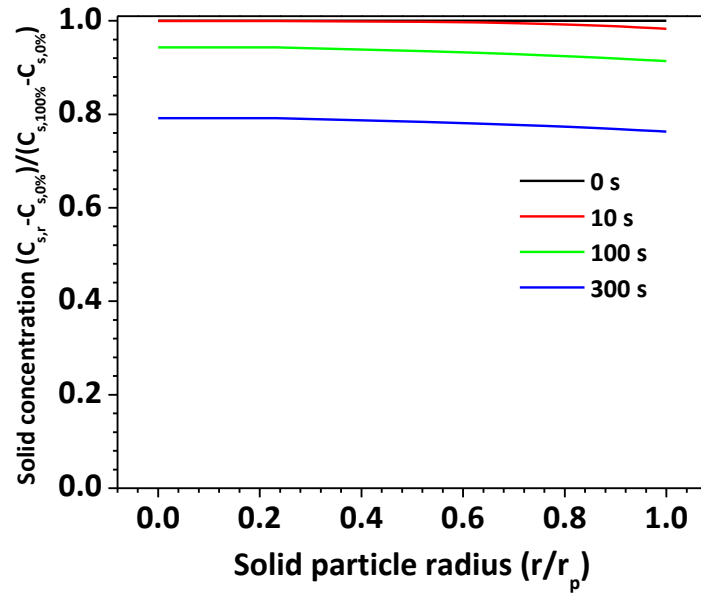
(a)
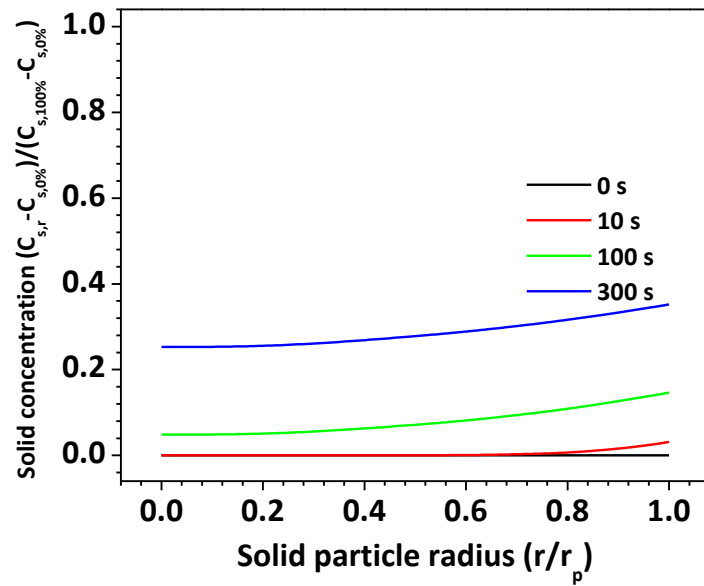
(b)

Figure 4-9: Li+ concentration in solid material particles, Rs = 0.2 Ω (a) anode; (b) cathode.
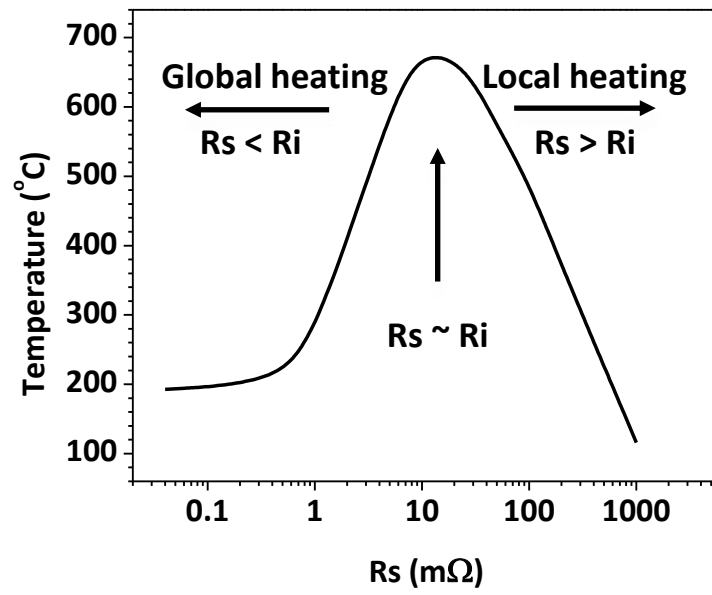
Figure 4-10: $T_{cell/nail}$ during penetration as a function of effective shorting resistance.

(a)

(b)

100s

(c)
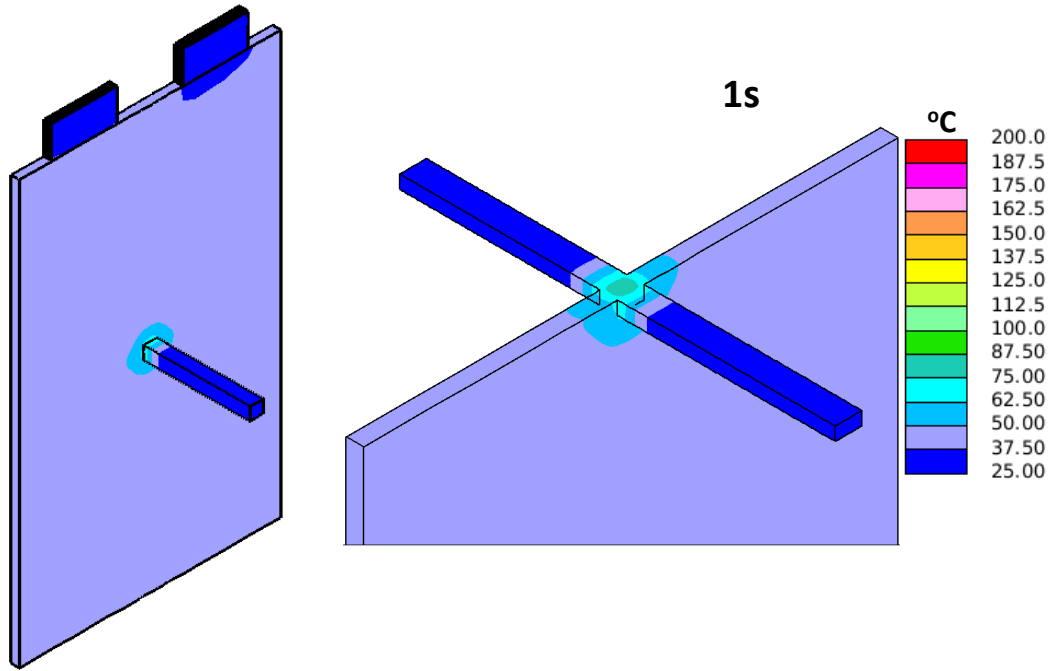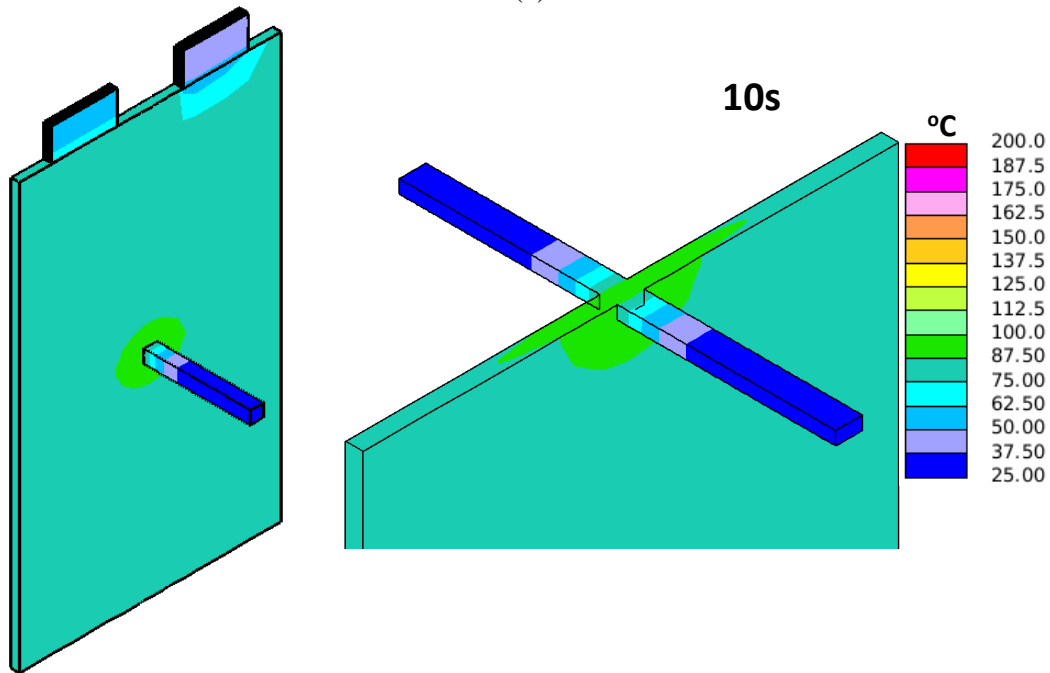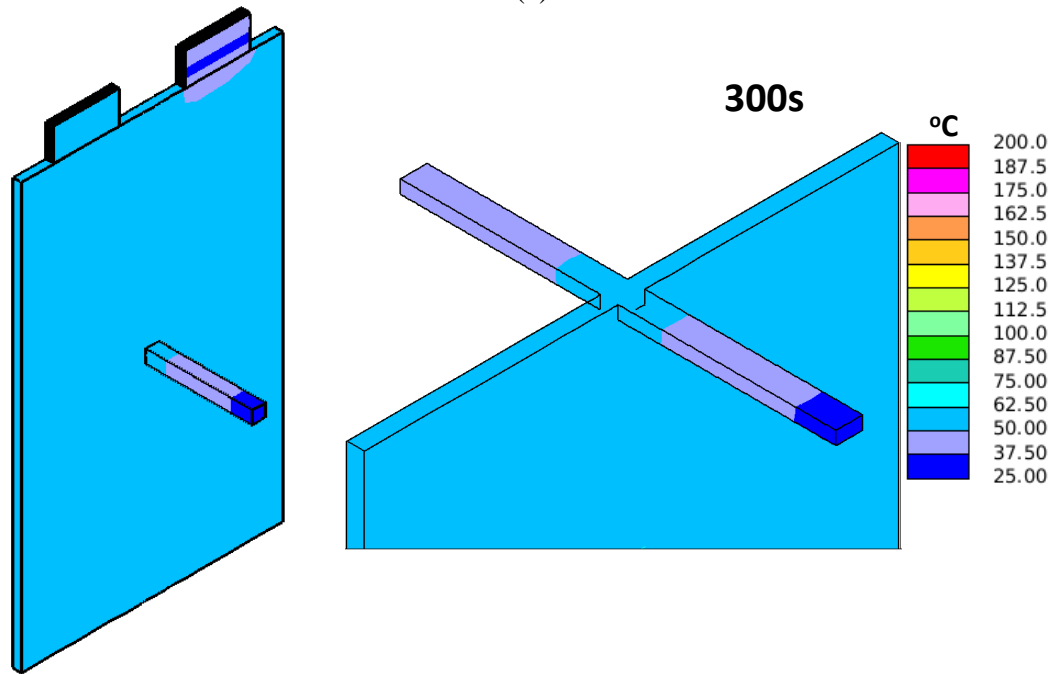
300s

(d)

Figure 4-11: 3D temperature distribution, Rs = 0.2 mΩ (a) 1s; (b) 10s; (c) 100s; (d) 300s.

(a)

(b)

(c)

(d)
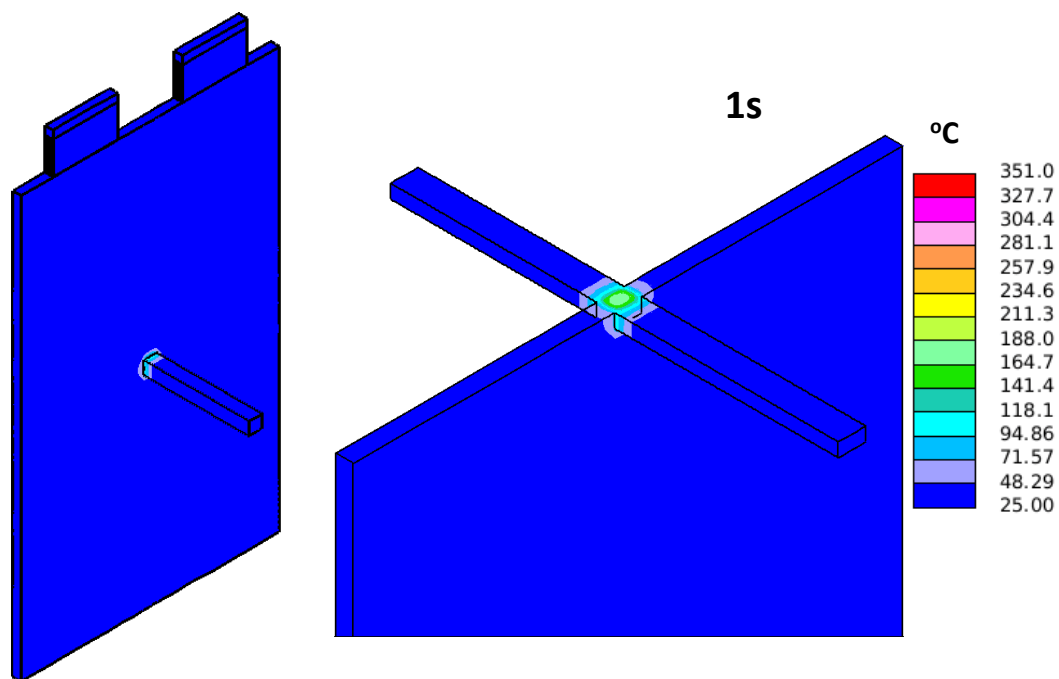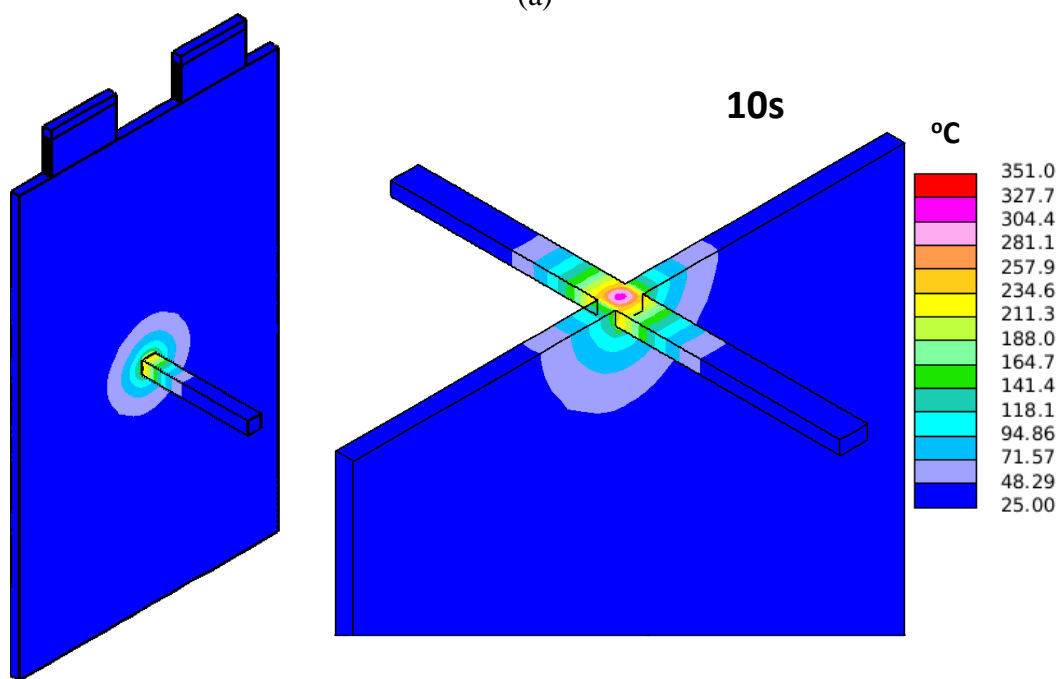
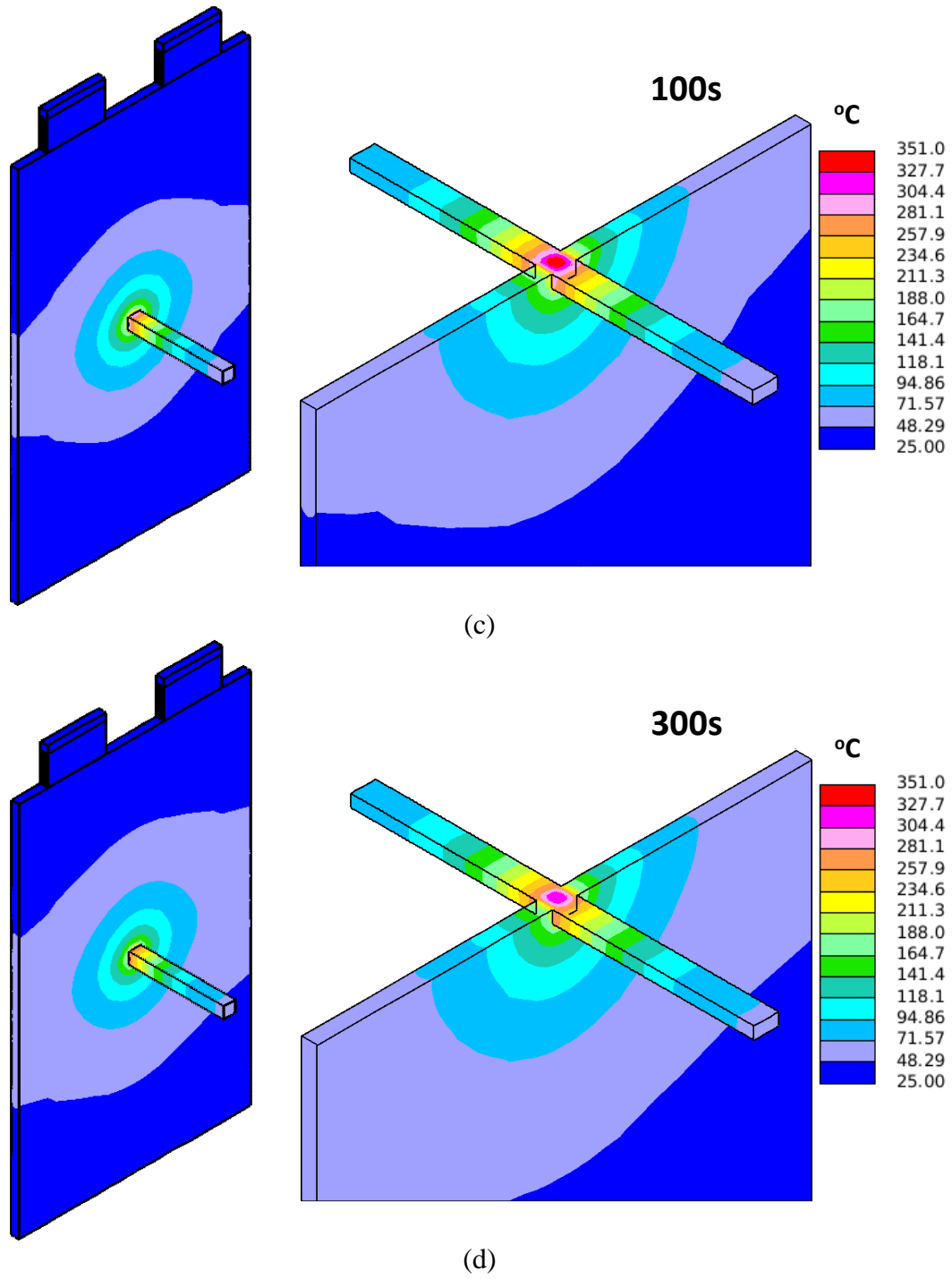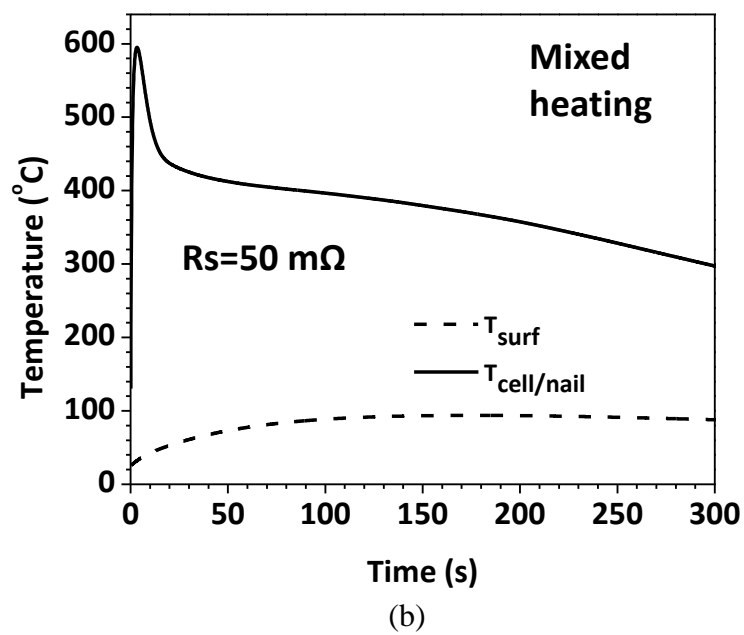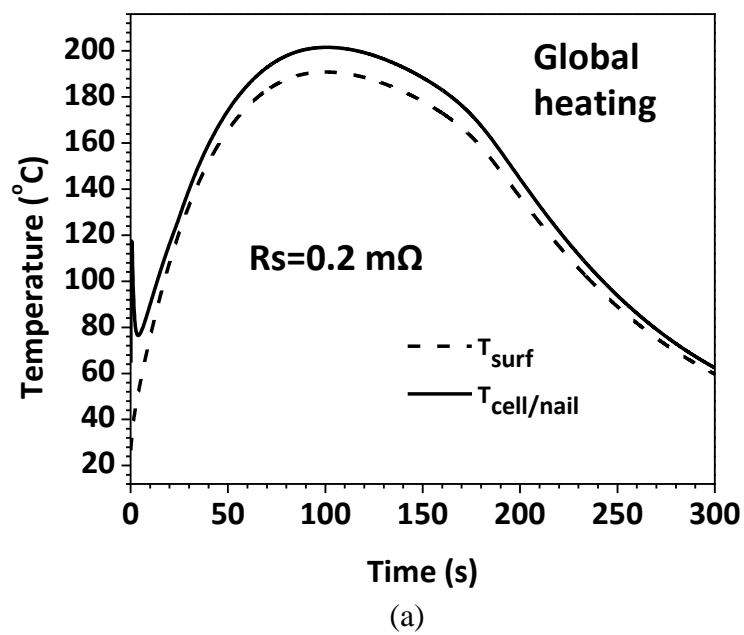**Figure 4-12**: 3D temperature distribution, Rs = 0.2 Ω (a) 1s; (b) 10s; (c) 100s; (d) 300s

(a)

(b)

(c)

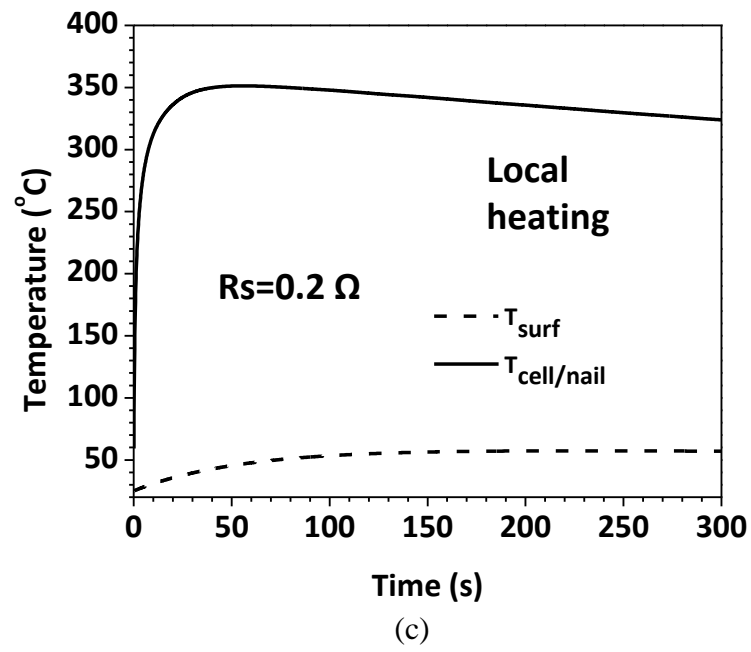**Figure 4-13**: $T_{cell/nail}$ and T_{surf} profiles (a) Rs = 0.2 mΩ; (b) Rs = 50 mΩ; (c) Rs = 0.2 Ω.
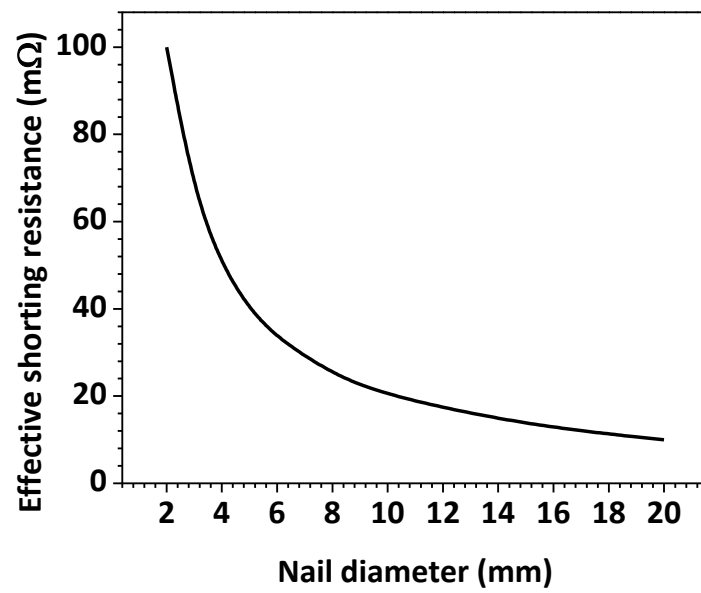
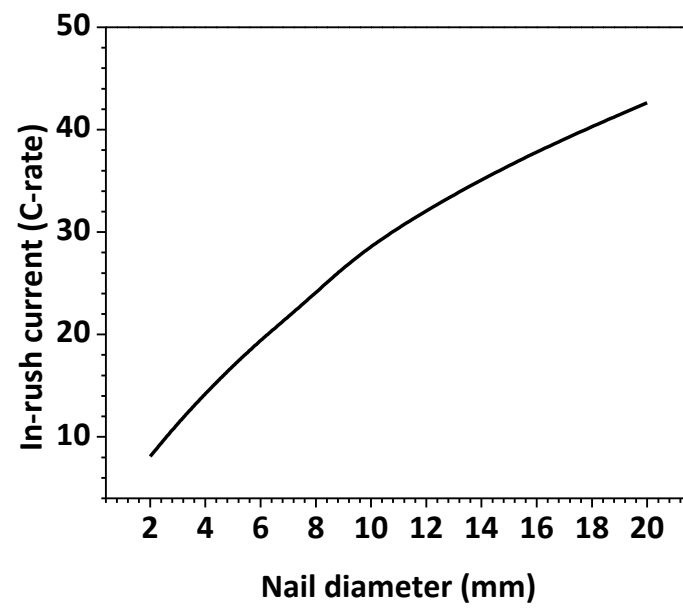**Figure 4-14**: Effective shorting resistance as a function of nail diameter.

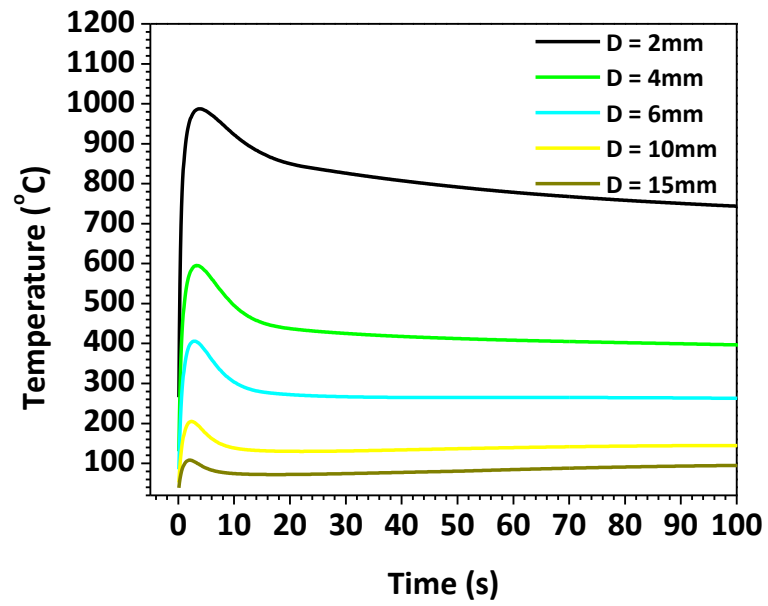**Figure 4-15**: In-rush current as a function of nail diameter.

Figure 4-16: $T_{cell/nail}$ profiles for different nail diameters
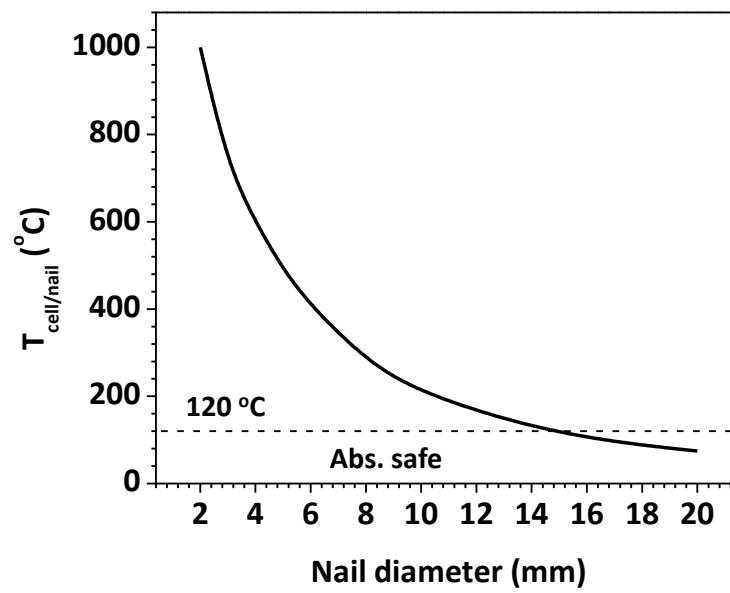
Figure 4-17: $T_{cell/nail}$ rise during penetration as a function of nail diameter.
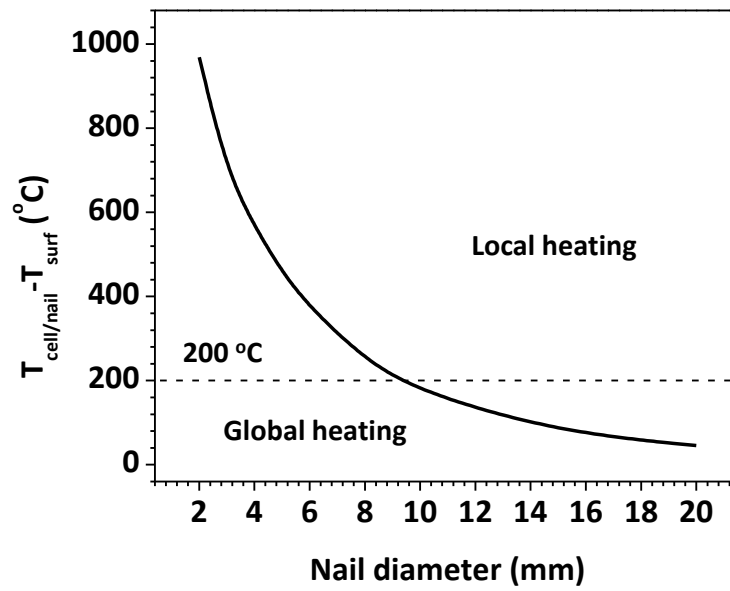
Figure 4-18: Difference between $T_{cell/nail}$ and T_{surf} as a function of nail diameter.

D=2 mm

°C

| 867.3 |
| 807.1 |
| 747.0 |
| 686.8 |
| 626.6 |
| 566.5 |
| 506.3 |
| 446.1 |
| 386.0 |
| 325.8 |
| 265.7 |
| 205.5 |
| 145.3 |
| 85.16 |
| 25.00 |

(a)

D=4 mm

°C

| 495.3 |
| 461.7 |
| 428.1 |
| 394.5 |
| 360.9 |
| 327.3 |
| 293.7 |
| 260.1 |
| 226.6 |
| 193.0 |
| 159.4 |
| 125.8 |
| 92.19 |
| 58.59 |
| 25.00 |

(b)

D=8 mm

(c)

D=20 mm

(d)
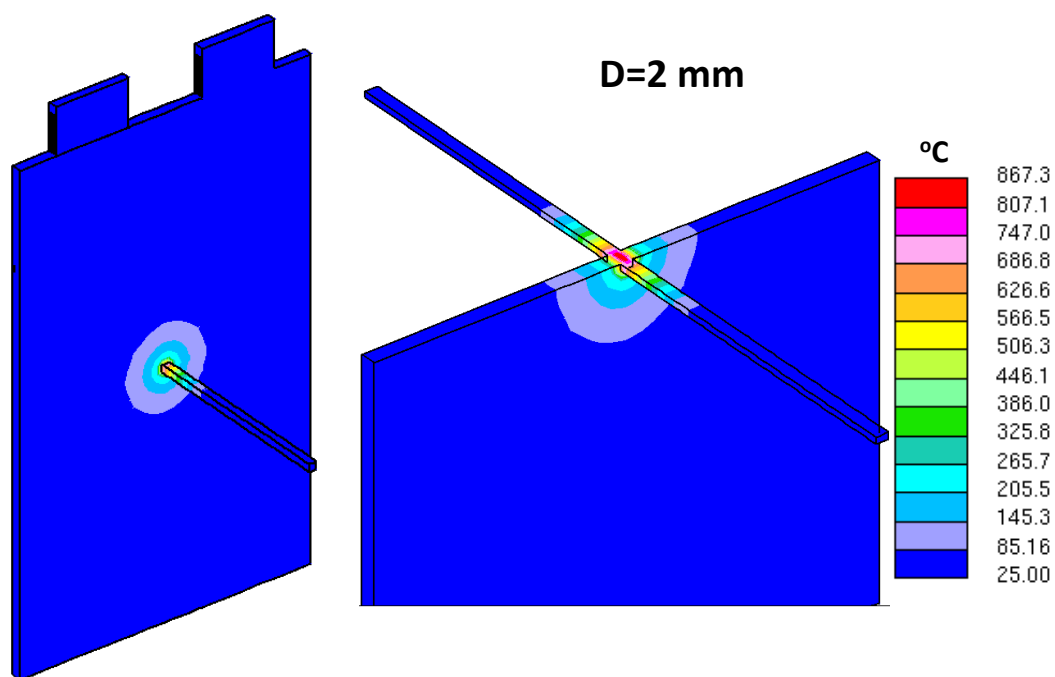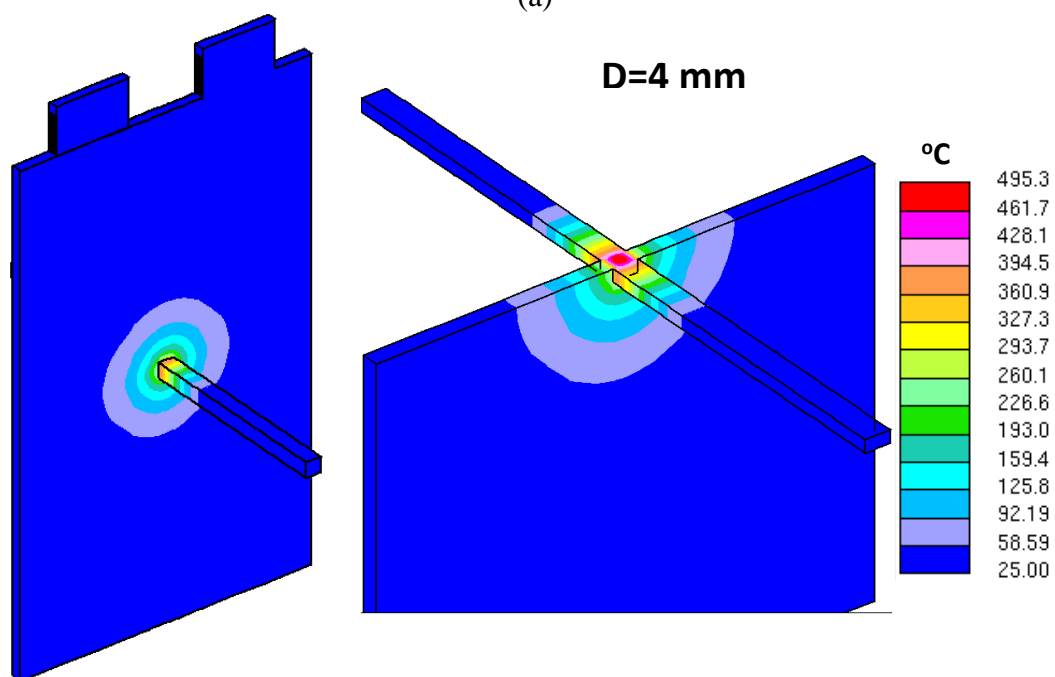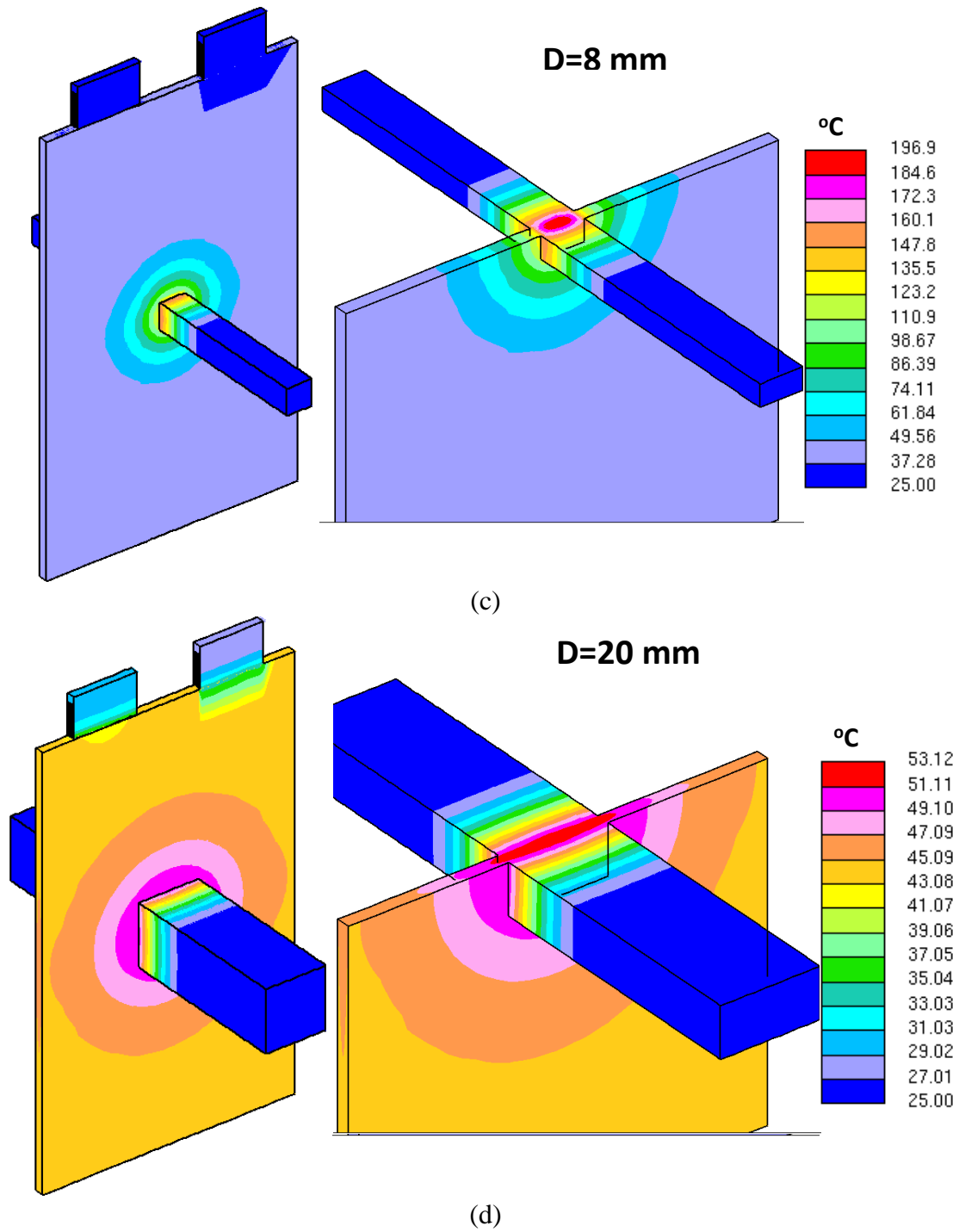
Figure 4-19: 3D temperature distribution Rs = 50 mΩ (a) D = 2mm; (b) D = 4mm; (c) D = 8mm; (d) D = 20mm.

Figure 4-20: $T_{cell/nail}$ profile for different nail thermal conductivities.

Figure 4-21: Computational mesh for cells penetrated at center, corner and top edge.

Figure 4-22: $T_{cell/nail}$ profile for different nail penetration locations.

Figure 4-23: $T_{cell/nail}$ profile for cells with different capacities.

Figure 4-24: $T_{cell/nail}$ rise during penetration as a function of cell capacity.

Chapter 5

Modeling of internal short-circuit process in large-format Li-ion cells

5.1 Introduction

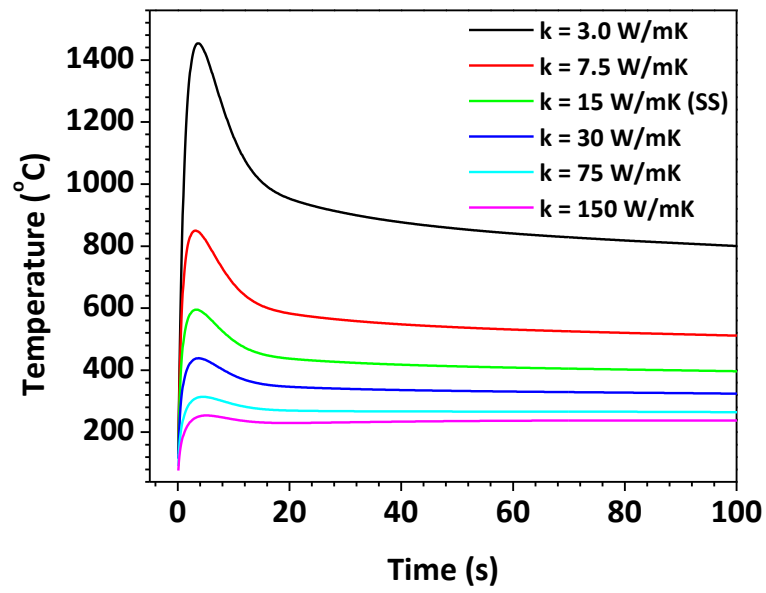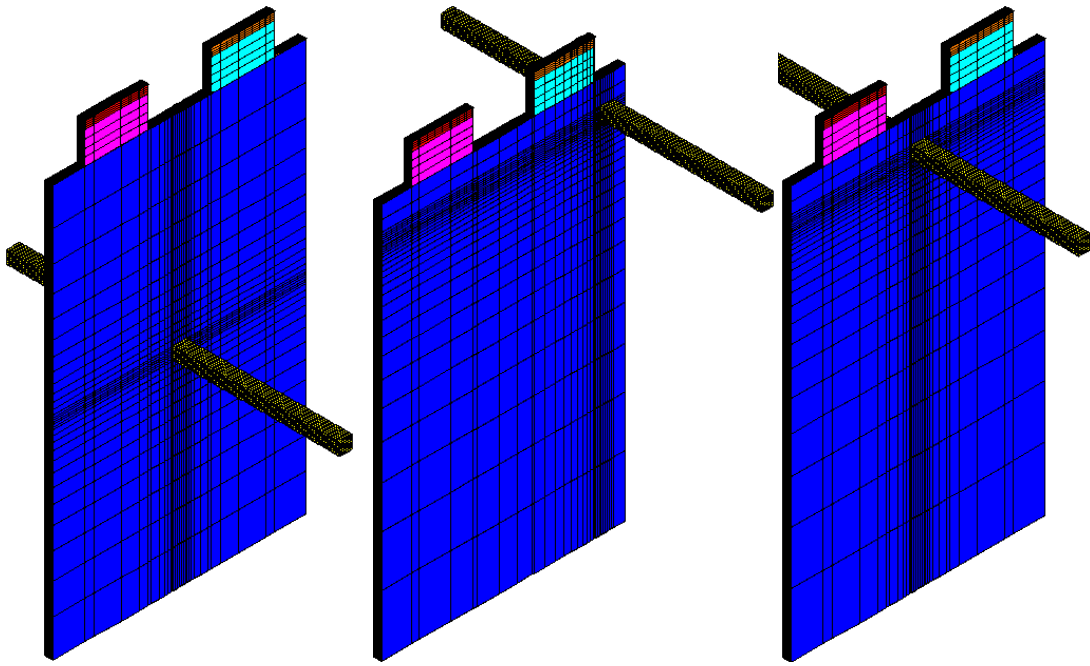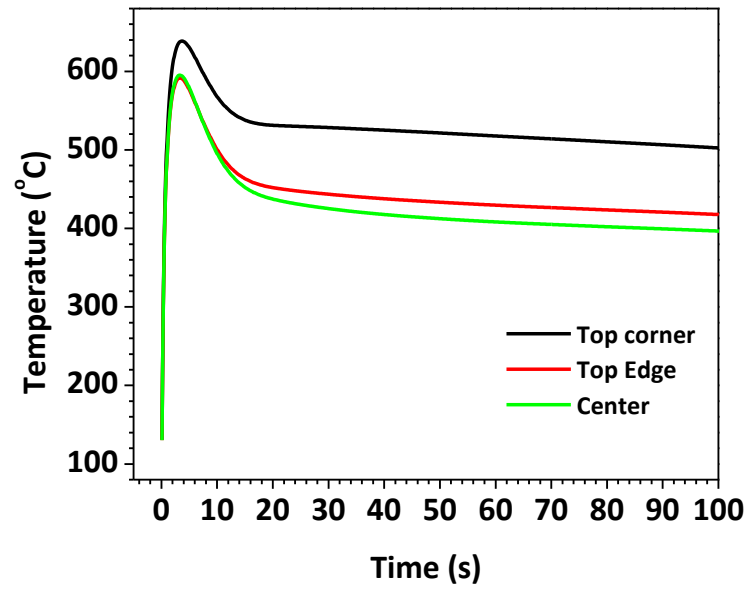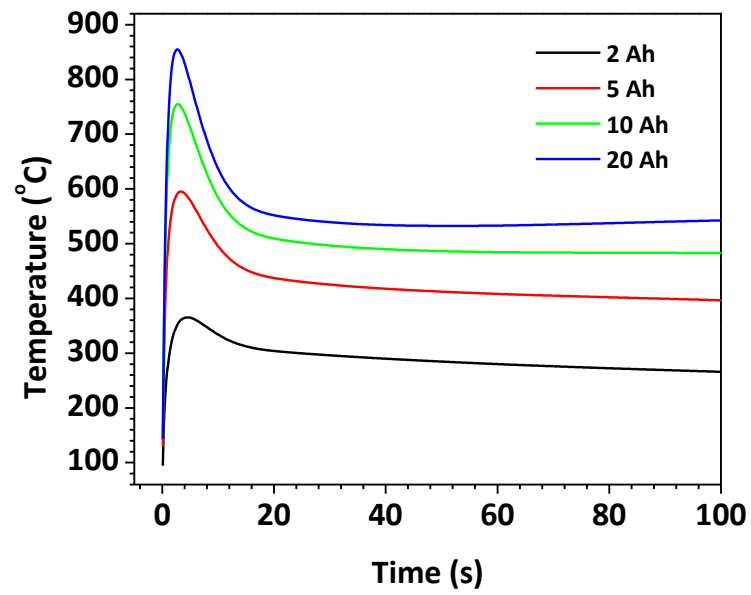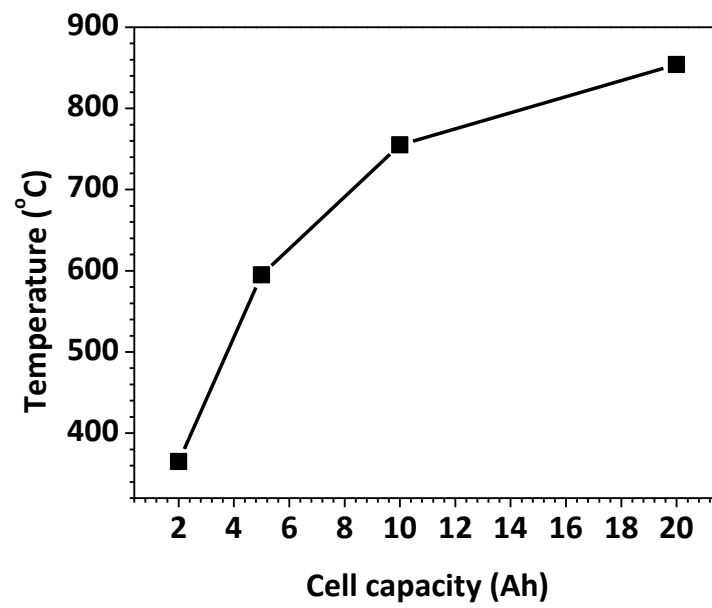Although nail penetration is widely used to test the Li-ion battery safety in industry, it has several disadvantages to truly emulate the internal short-circuit process as seen in a field-failure. First of all, the cooling effect through the penetration nail could be very significant. The test procedure can be manipulated to generate a "safe" result by using nails that will facilitate the heat transfer. Secondly, the nail penetration process often breaches the cell closure and causes electrolyte leak and pressure release, which is not often seen in a field-failure involving internal short-circuit. Thirdly, the nail penetration speed is usually around 40~ 80 mm/s, which means all electrode plates of the battery are instantaneously penetrated. The total heat generation is then distributed equally to each of the electrode plates, leading to a relatively global heating of the cell.

On the other hand, the internal short-circuit usually occurs within one or a few electrode plates depending on the size of the object causing the short-circuit. As a result, the current flow path and heat generation distribution are very different from the nail penetration process. Fig. **5-1** illustrates the current flow path for both cases. Fig. **5-1(b)** illustrates the nail penetration process. Since the nail always pierces through the cell completely, it creates a short-circuit and closed current loop in each of the electrode plate. There is no current flowing through the tabs from one electrode plate to another. Each of the multiple electrode plates discharges and consumes its energy within itself. There is no energy exchange between different plates. Fig. **5-1(a)** shows the scenario of internal

short-circuit process, where a short-circuit object (SCO) is embedded within one electrode plate of the cell. The SCO could be a metal particle introduced during the cell manufacturing process. It can also be Li dendrite formed by Li plating due to overcharge or degradation. The SCO creates a short-circuit and current loop within the electrode plate where the SCO is located. This electrode plate not only discharges its energy to itself, it also serves as a load to the other un-shorted electrode plates. Because different electrode plates are connected by tabs, large amount of current will be generated from un-shorted layers, flow through the tabs, and converge to the shorted electrode plates and SCO. Therefore it can be deduced that not only a hot spot will exist around the SCO, the temperature rise on the tabs will also be significant due to large current flow and small thermal mass of the tabs.

Some test procedures have been developed such as crush test to simulate the internal short-circuit of Li-ion cells. However, the test methods have common problems in terms of reproducibility and reliability of the results. The reason is that it is very difficult to precisely control the key parameters, such as short-circuit location, resistance, and size, which have significant impact on the cell behavior during the internal short-circuit. More importantly, the results from the experimental studies provide few insights into the fundamental mechanisms, particularly the electrochemical and thermal coupling that governs the cell behavior during the internal short-circuit process.

Therefore there is a need to utilize modeling tool to investigate the detailed electrochemical and thermal behaviors of Li-ion cells during internal short-circuit process. In this chapter, we will be using the multidimensional multiscale battery model

developed in Chapter 2 to study an internal short-circuit process in a large-format Li-ion cell.

5.2 Approach

The present chapter studies the same prismatic stack-electrode cell used for the nail penetration study in Chapter 4. In the nail penetration study, all the electrode plates are assumed to be identical in terms of electrochemical behavior. Only one electrode plate is used for solving the electrochemical equations. For the internal short-circuit study, however, due to the above mentioned reasons, all electrode plates including the tabs, must be used for solving the electrochemical equations. Therefore, the full 3D electrochemical and thermal coupled model is used for the problem.

Fig. **5-2(a)** shows the geometry and computational mesh of the 5 Ah cell under study. Note that the cell design and geometry is the same as those used in Chapter 4. For all simulation cases, the SCO has an area of 4mm x 4mm and is embedded inside of the cell at the center of y-z plane. The SCO may short only one electrode plate, or it may cause several plates to be shorted, depending on the length of the SCO. Due to the possible large potential and temperature gradient, the mesh for the tabs and the cell region around the tabs is refined, as shown in Fig **5-2(b)**. The total mesh number is 595488, about 40% more than the mesh for the nail penetration study. The Al tab temperature is monitored in the simulation. The cell surface temperature and the temperature of the SCO are also monitored, as illustrated in Fig. **5-3**.

5.3 Results and discussion

5.3.1 Effect of shorting resistance

The shorting resistance has a significant influence on the cell electrochemical and thermal behavior during short-circuit process. Its value, however, is determined complicatedly by several parameters, including the intrinsic resistance of the SCO, the contact resistance between the SCO and cell, and the short-circuit scenarios. According to several studies[28, 83], there are four possible internal short-circuit scenarios: (i) the short between two current foils, (ii) the short between Al foil and anode active material, (iii) the short between Cu foil and cathode active material, (iv) the short between anode and cathode active material. To date accurate value of the short-circuit resistance under various short-circuit scenarios cannot be measured in-situ due to the limitation of experimental techniques. In the present study, two estimated values of short-circuit resistance are chosen to represent two different short-circuit scenarios. As shown in Fig. **5-4**, in the first scenario, the short-circuit is caused by the SCO connecting the anode active material and Al foil. The estimated resistance is 4 Ω per electrode plate. In the second scenario, Cu foil and Al foil are connected by the SCO. The estimated resistance is 5.2 mΩ per electrode plate. The shorted electrode plate is the 13$^{\text{th}}$ plate, counting from the bottom of the cell. Hence, the SCO is located approximately at the center of the cell thickness direction.

Fig. **5-5** shows the calculated temperature profile for the large short-circuit resistance case (R_s = 4.0 Ω/plate). The SCO temperature rises from the initial temperature of 25 $^{\text{o}}$C to above 60 $^{\text{o}}$C in about 20 s. On the other hand, the tab temperature and cell

surface temperature remain low and increase slowly throughout the short-circuit period. The large difference between the SCO temperature and cell surface temperature implies localized heating on the SCO. Fig. **5-6** illustrates contours of the surface temperature and the temperature at the center plane of the cell thickness direction. It can be seen that a hot spot is formed and confined in the small region around the SCO. The temperature in the majority part of the cell, including the cell surface and tabs, remains low throughout the simulation period. This highly non-uniform temperature distribution is a result of localized heating on the SCO. The hot spot embedded deeply inside the cell brings difficulty for the battery management systems (BMS) to early detect the occurrence of short-circuit since only the cell surface temperature is measured in a battery system.

The cell thermal response during the short-circuit process is governed by the electrochemical behavior of the cell. Fig. **5-7** illustrates the current and voltage response during the short-circuit period. The short-circuit current is small and remains almost constant during the short-circuit process. The cell voltage decreases only slightly from the open-circuit voltage (OCV). Because the SCO resistance is much larger than cell internal resistance, the short-circuit current is controlled by the SCO resistance and the SCO draws most of the voltage drop. As a result, the total heat generation in cell is mainly contributed from the Joule heating on the SCO. The heat generation from the various internal processes of the cell, on the other hand, is negligible. The Li+ concentration distribution in the electrolyte (Fig. **5-8**) and solid particles (Fig. **5-9**) only varies slightly from the initial conditions during the short-circuit period and hence has negligible effect on the thermal behavior.

Fig. **5-10** illustrates the temperature profile of the small SCO resistance case ($R_s =$ 5.2 mΩ/plate). The temperature behavior is significantly different from that of the large resistance case. The temperatures in both SCO and Al tab jump to above 500 ^{o}C immediately following the short-circuit. Therefore, in contrast to the large resistance case, two hot spots are formed, one on the tabs and the other on the SCO. Because only the 13th plate is shorted by the SCO, current supplied from the other 25 plates will converge and pass through the Al and Cu tabs on the 13th plate. The small SCO resistance results in a large shorting current that in turn results in a large Ohmic heating on the tabs. Also because the tabs are very small (their thickness is the same as the foils), a sharp temperature rise is caused due to their small thermal mass.

From the cell temperature contour shown in Fig. **5-11**, it can be seen that the heating is localized around the SCO, and on the two current collecting tabs of the 13th electrode plate as well. The temperature in these areas rises to ~600 ^{o}C in only 1 s after the short-circuit. Exothermic reactions are inevitable to occur and may trigger thermal runaway.

The electrochemical behavior of the small resistance case is also vastly different from the large resistance case. As shown in Fig. **5-12**, the cell voltage drops to 2.2V upon the start of short-circuit and decays exponentially thereafter. The inrush current amounts to 29 C-rate and also decays exponentially in the following short-circuit process. The decay of the short-circuit current and cell voltage implies mass transport limitation inside the cell. By checking the Li+ concentration distribution in the electrolyte (Fig. **5-13**) and in the active material particles (Fig. **5-14**), we can find that the solid diffusion process is not the limiting factor since neither anode nor cathode solid particle reaches mass

transport limitation. On the other hand, the Li+ concentration distribution in the electrolyte shows that mass transport limitation occurs in the cathode electrode. The Li+ concentration in the cathode drops quickly and becomes depleted in about 20 s. Because both the exchange current density i_0 and electrolyte conductivity κ^{eff} decrease as the depletion of Li+ concentration in electrolyte, the cell internal resistance will increase significantly when the Li+ depletion occurs. The increased cell resistance is the reason for the rapid decrease of shorting current and cell voltage.

Fig. **5-15** and Fig. **5-16** display the solid potential distribution and current flow vectors on the current collector foils. To better illustrate the result, the Cu and Al foils are spread out in a 2-D plane. The calculation data is then mapped onto the 2-D geometry. From Fig. **5-15(a)** and Fig. **5-16(a)**, it can be seen that the current is distributed from the shorted electrode plate to the un-shorted plates at anode, as shown by the current flow vectors on the Cu foils. On the other hand, the current converges from the un-shorted electrode plates to the shorted electrode plates at cathode, as shown by the current vectors on the Al foils in Fig. **5-15(b)** and Fig. **5-16(b)**. The solid potential distribution of the small shorting resistance case indicates there is a large voltage gradient across the tabs of the shorted electrode plate, which explains the significant heating of tabs. For large shorting resistance case, the voltage drop on foils and tabs is very small; most of the voltage drop is located in the SCO.

The single-plate shorting can best simulate the internal short-circuits seen in field incidents because intern short-circuits are usually caused by small metal particles that can only cause shorting of one single electrode plate. The above simulation shows that local heating will always be caused in single-plate shorting. Besides heating on the SCO,

significant temperature rise could also occur on the tabs. Therefore, in large format Li-ion cells, tabs temperature should be monitored for the detection of internal short-circuit.

5.3.2 Effect of number of shorted electrode plates

The above cases investigate the short-circuit scenario when only one electrode plate among the 26 plates is shorted by the SCO. However, in some cases multiple electrode plates can be shorted. For example, when the cell is crushed or dented by external forces, more than one electrode plate can be shorted as a result of deformation of the cell structure. Lithium metal dendrite caused by lithium plating during overcharge may also grow large enough to penetrate through multiple electrode plates, causing multiple short-circuits. Therefore it is interesting to explore the difference in the behavior between single-plate shorting and multiple-plate shorting. The previous section studies the single-plate shorting where the 13th electrode plate is shorted by the SCO. In this section, the number of shorted electrode plate ranges from 2 to 26 and each shorted plate has identical shorting resistance. Because the 26 electrode plates are connected in parallel, the total resistance of N-plate shorting should equals 1/N of the shoring resistance for single-plate shorting, i.e.

$$R_{s,N-plate} = \frac{R_{s,1-plate}}{N} \tag{5-1}$$

Fig. **5-17** and Fig. **5-18** display the calculated temperature rise of Al tab and SCO during the simulated internal short-circuit period. For the small resistance case, as shown in Fig. **5-17(a)**, the temperature rise of both Al tab and SCO reduces as the increase of the number of shorted electrode plates. The reason is that for small shorting resistance, the

shorting current is mostly determined by the cell internal processes. When multiple

electrode plates are shorted, the total heat generation will be distributed to multiple tabs

and SCOs, leading to a reduced volumetric heat generation. Fig. **5-17(b)** shows that the

volumetric heat generation in the SCO decreases significantly as the increase of shorted

plate numbers. The significantly reduced volumetric heat generation is the reason for the

lower temperature rise for multiple-plate shorting. Also noted from Fig. **5-17(a)** is the

fact that the temperature rise of the tab reduces more rapidly than that of the SCO. This is

because the tab has a much smaller thermal mass which makes its temperature more

sensitive to the change of the heat generation.

Also, when more electrode plates are shorted, the shorting current will be more

uniformly distributed. For example, as shown in Fig. **5-19**, when only one electrode

plates is shorted, the shorting current contributed from the other 25 plates will all flow

through the shorted plate. When three electrode plates are shorted, the shorting current

coming from the other 23 plates will be evenly distributed to the three plates, each of

which carries 1/3 of the current. When all 26 plates are shorted, each plate will carry the

current generated in its own electrode. No current will be flowing among different

electrode plates. Therefore, as the increase of shorted plate number, the heating mode will

transition from local heating to global heating, as illustrated by the temperature contour in

Fig. **5-20**.

For the large resistance case, the temperature rise as a function of shorted plate

number exhibits the complete opposite trend. As shown in Fig. **5-18(a)**, the temperature

rise of SCO increases with the number of shorted plate. The increasing rate is significant.

For single-plate shorting, the temperature rise is only 39 ^{o}C. But when all 26 plates are

shorted, the temperature rise amounts to above 800 $^{\circ}$C, which will definitely trigger

thermal runaway. This is because that when the shorting resistance is large, the shorting

current is controlled by the shorting resistance rather than cell internal resistance.

Increasing the number of shorted plates doesn't change the volumetric heat generation in

SCO, as shown in Fig. **5-18(b)**. Instead, it creates heat generation spots in more electrode

plates inside the cell. Because the heat dissipation area does not change and remains

constant, the end result is the significantly increased temperature rise. The temperature

contour in Fig. **5-22** shows that regardless of the number of shorted plates, the heating is

always localized in the SCO. The tab temperature rise in Fig. **5-18(a)** is very small

compared with SCO temperature rise because of the very small heat generation on tabs.

The current flow path is similar to that of small resistance case as shown in Fig. **5-21**,

except that the voltage loss in the foils is much smaller than that of small resistance case,

which indicates that most of the voltage drop and heat generation are concentrated in the

SCO.

5.4 Conclusion

Internal short-circuit represents the most dangerous abusive condition for Li-ion

batteries. Most of the field incidents involving Li-ion batteries were caused by internal

short-circuits. In this chapter, a computational effort has been carried out to study the

fundamental electrochemical and thermal mechanisms underlying the internal short-

circuit process of a large-format Li-ion cell. The key conclusions derived from the

simulation results are as follows.

Internal short-circuit process is very different from the nail penetration process. Internal short-circuit is usually caused by metal particle contamination during the manufacturing process or Li metal dendrite growth due to overcharge or degradation. The SCO causing the short-circuit is often very small so that only one or a few electrode plates are shorted. In the nail penetration process, however, all the electrode plates are shorted simultaneously due to the high penetration speed.

In the internal short circuit process, the shorted electrode plates where the SCO is located serve as the load to the other un-shorted electrode plates. The current produced from the un-shorted plates converges and flows through the tabs of the un-shorted electrode plates. When the SCO resistance is small compared with the cell internal resistance, this will cause significant heating on the tabs. For large SCO resistance scenario, tab heating is negligible as the majority of heat generation is concentrated on the SCO. Therefore, for large format Li-ion cell, it is necessary to monitor the tab temperature in order to detect the occurrence of internal short-circuit.

Depending on the size of the SCO, one or multiple electrode plates can be shorted. The number of shorted electrode plates has a significant effect on the cell thermal response. For small SCO resistance, the temperature rise reduces dramatically as the increase of shorted electrode plate. For large SCO resistance case, however, the opposite trend is observed. The contradictory trends explain the poor reproducibility of the internal short-circuit experimental tests such as crush test. In those tests, it is impossible to precisely control the shorting resistance and the number of shorted plates. The experimental results therefore vary significantly from test to test.
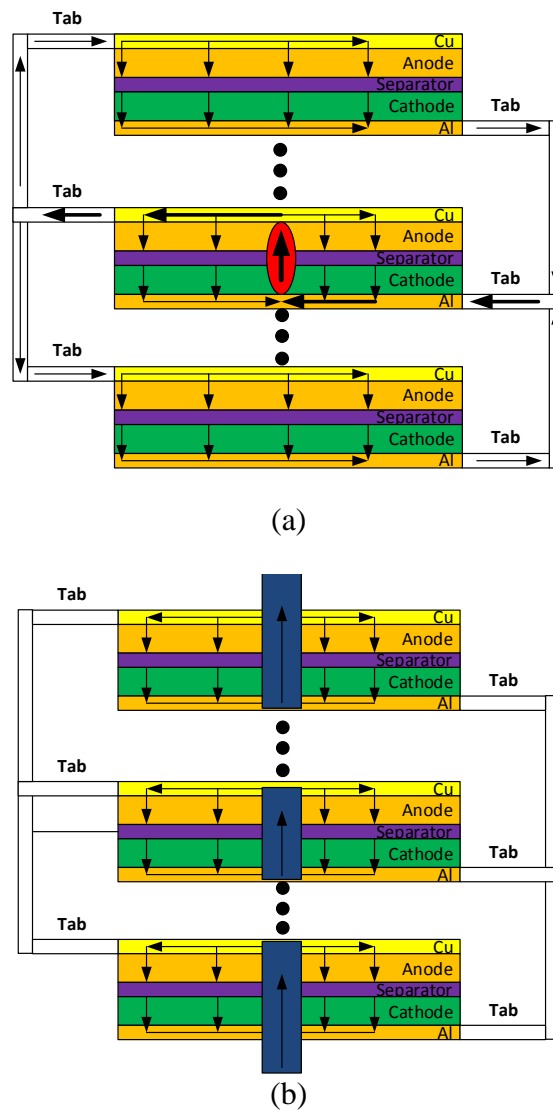
(a)

(b)

Figure 5-1: Difference of current flow path between (a) internal short-circuit process and (b) nail penetration process
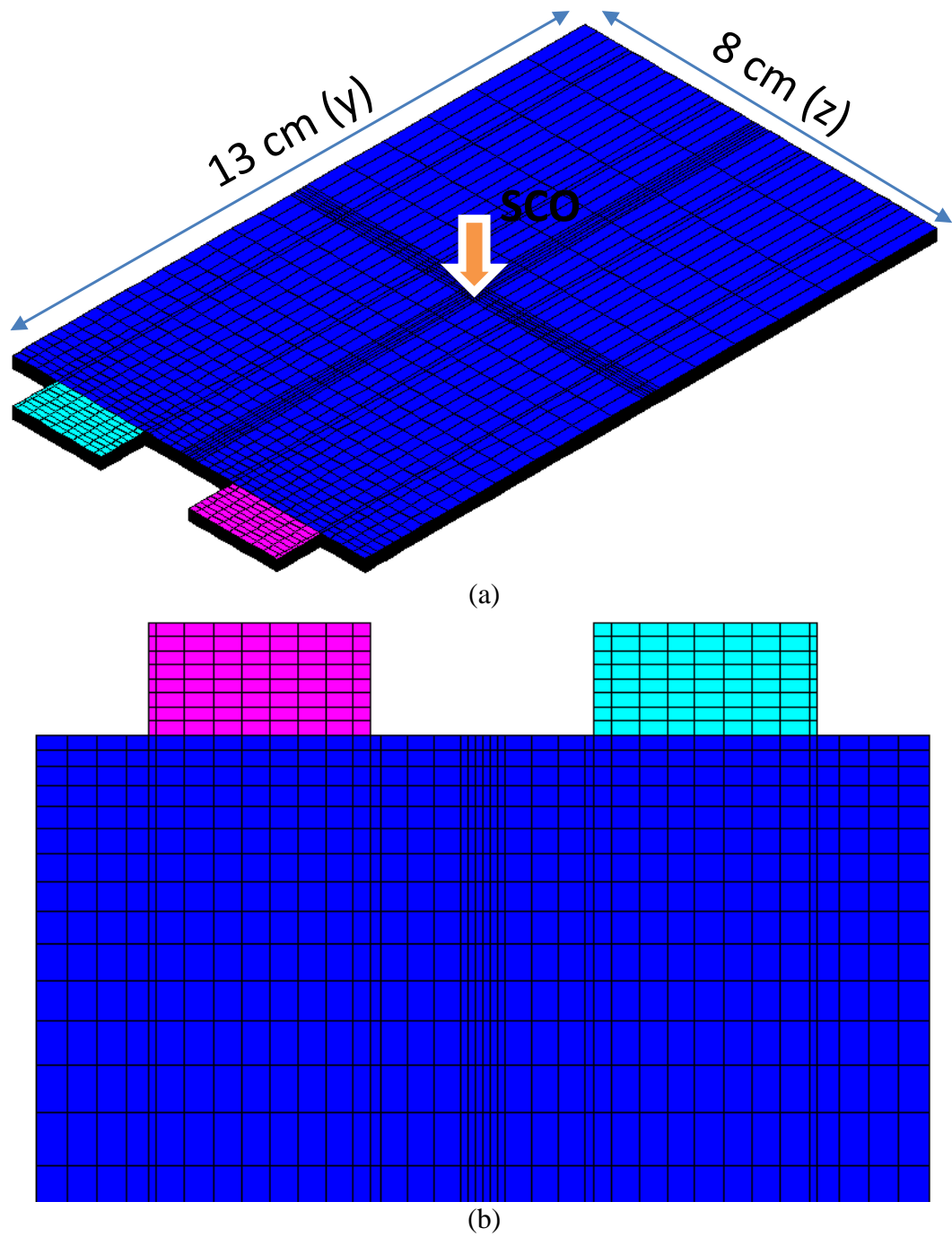
(a)

(b)

Figure 5-2: Geometry and computational mesh of the 5 Ah cell (a) overall mesh; (b) mesh around the tabs region.
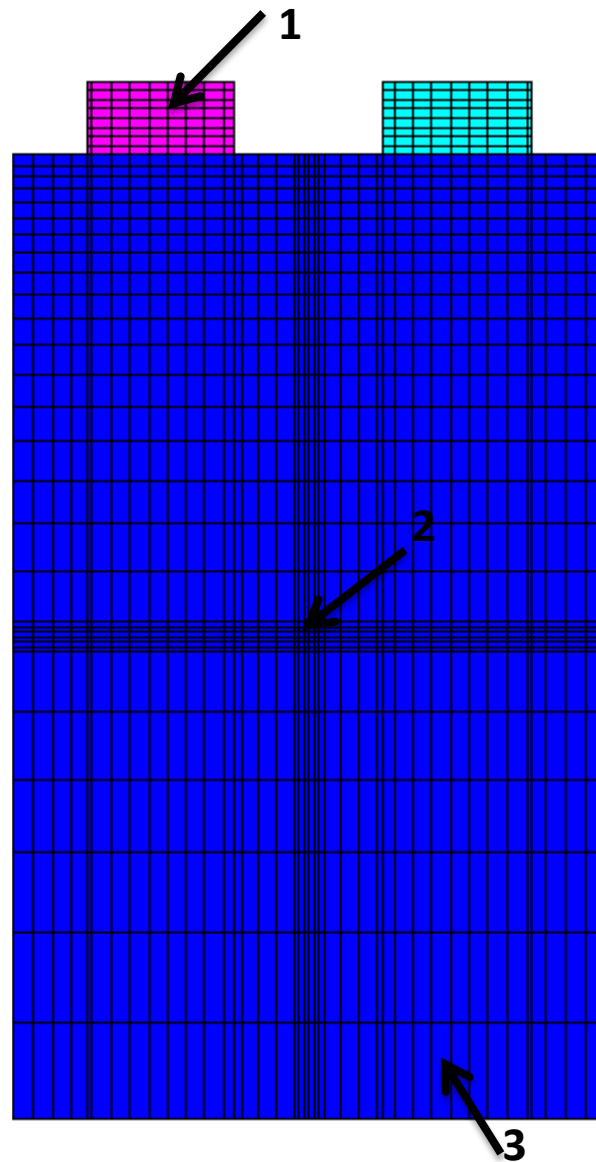
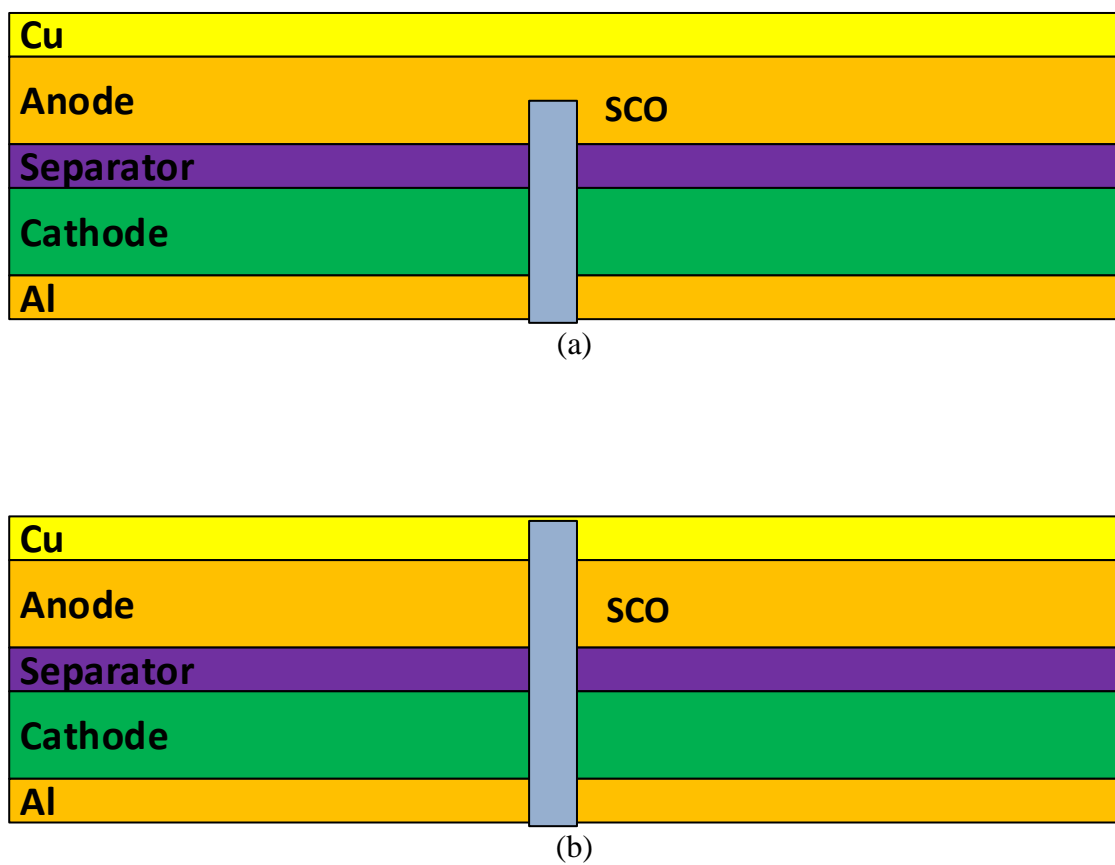**Figure 5-3**: Temperature monitoring locations (1) Al tab; (2) SCO-cell interface; (3) cell surface

Figure 5-4: Two typical internal short-circuit scenarios (a) short between anode material and Al foil (Rs = 4 Ω/plate); (b) short between Cu foil and Al foil (R_s = 5.2 mΩ/plate).
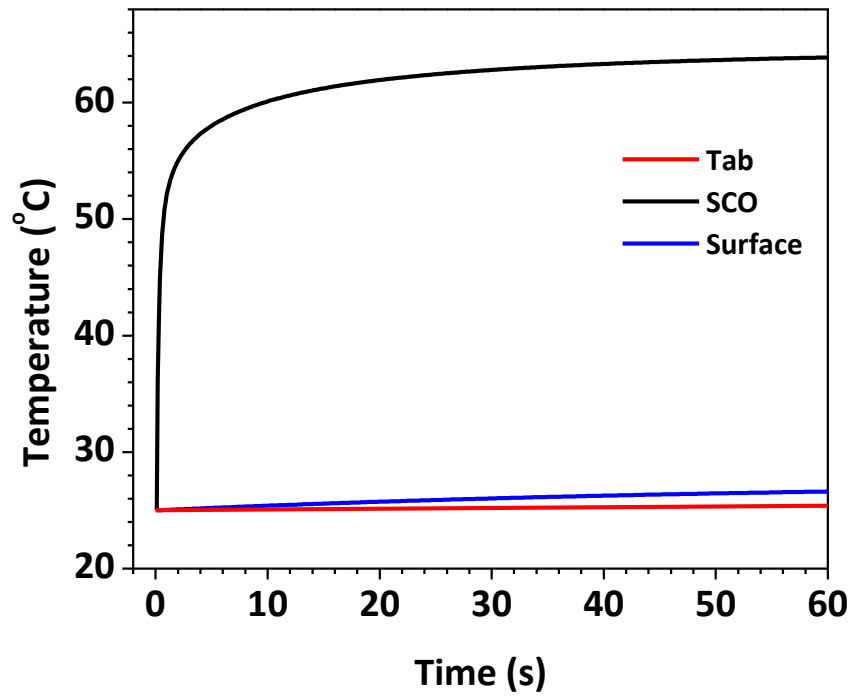
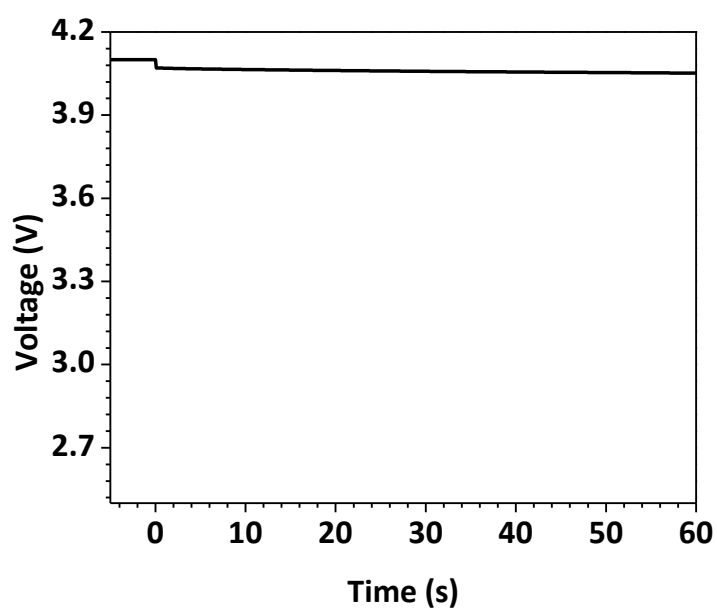**Figure 5-5**: Temperature response (shorted plate = 13th plate, R_s = 4 Ω/plate)
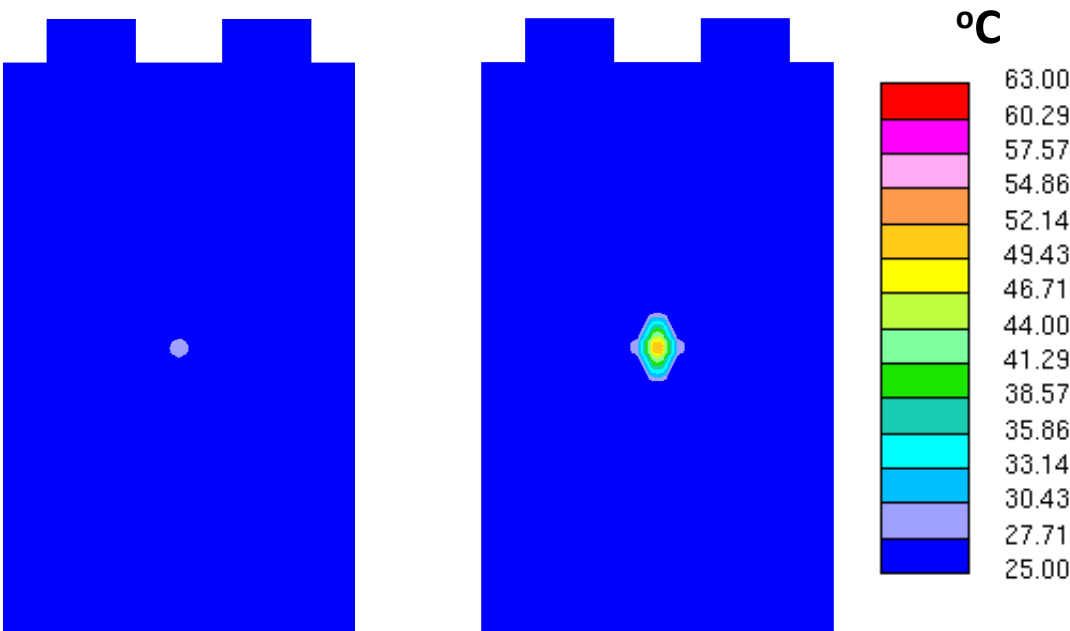
(a)
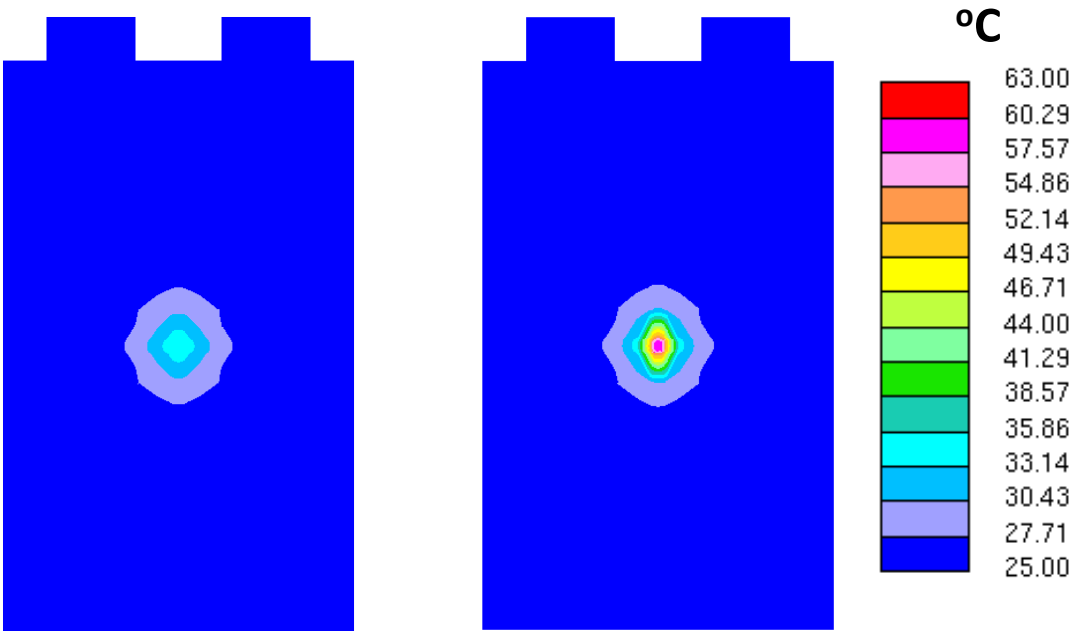
(b)
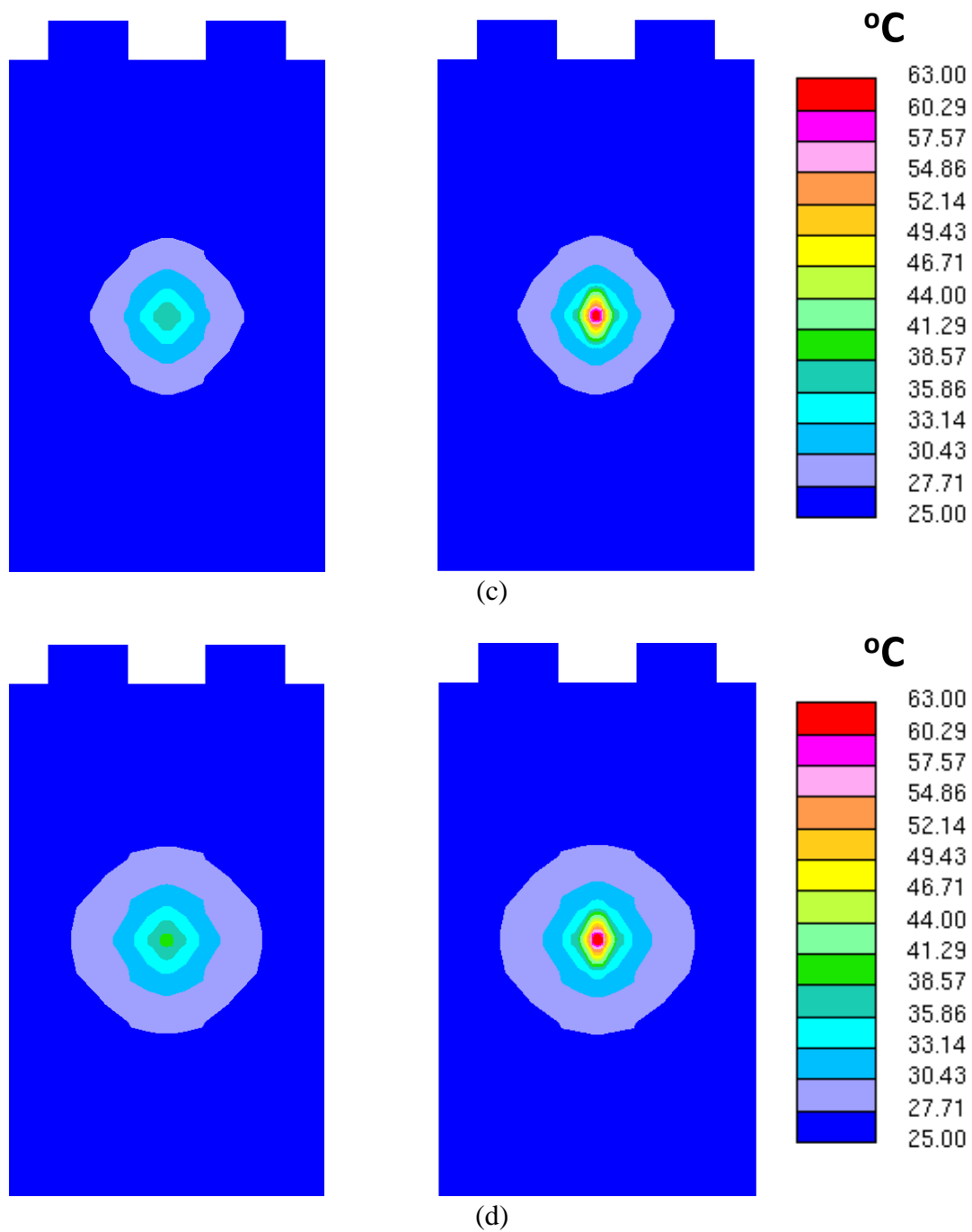
Figure 5-6: 2D temperature contour (shorted plate = 13th plate, R$_s$ = 4 Ω/plate, left: cell surface, right: cell center plane) (a) 1s; (b) 10s; (c) 30s; (d) 60s
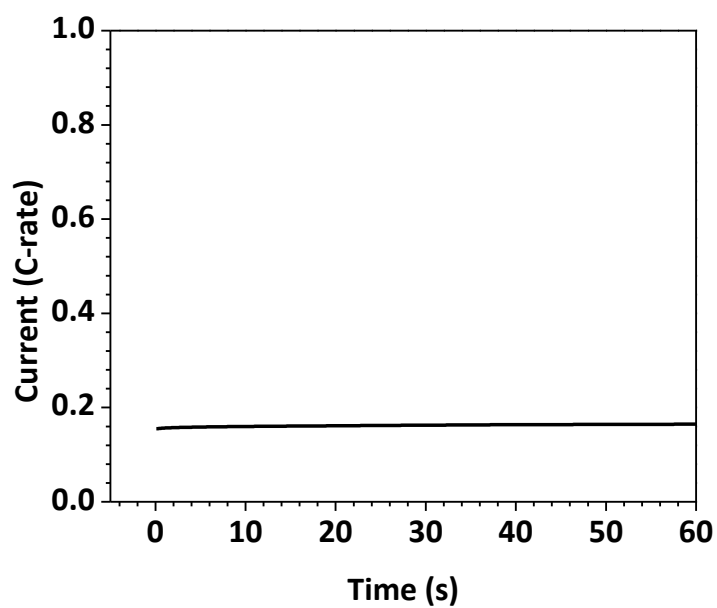
(a)

(b)

Figure 5-7: Current and voltage response (shorted plate = 13th plate, R$_s$ = 4 Ω/plate) (a) current; (b) voltage.
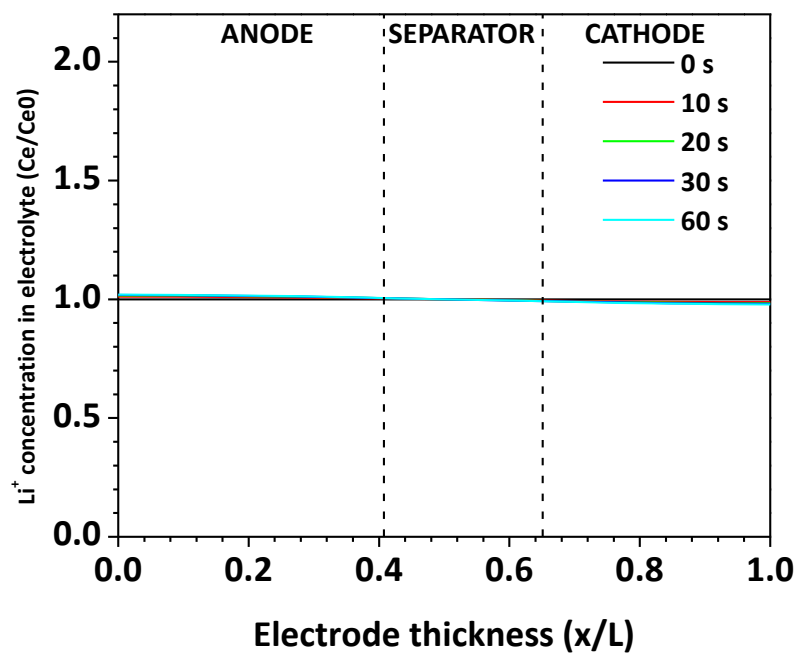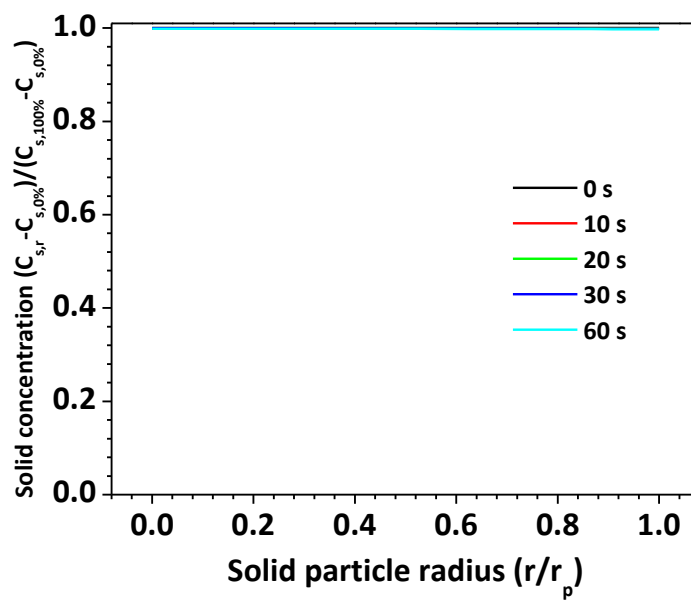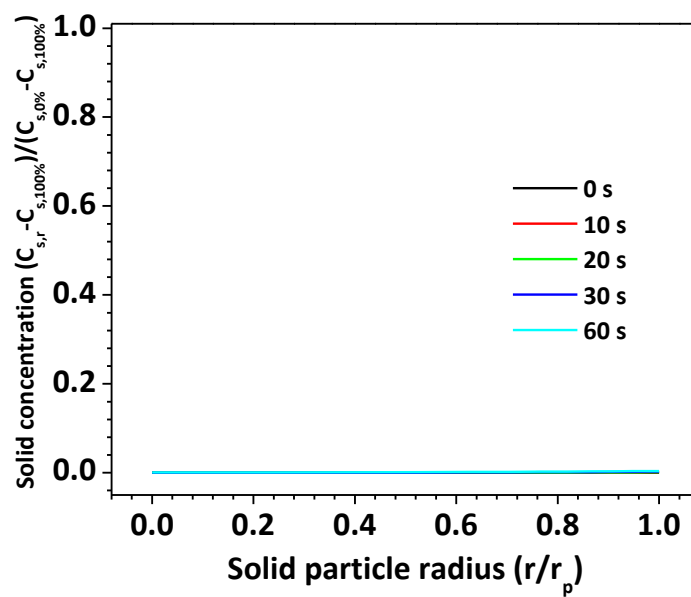
Figure 5-8: Li+ concentration in electrolyte (shorted plate = 13th plate, R_s = 4 Ω/plate)

(a)

(b)

Figure 5-9: Li+ concentration in active material particles (shorted plate = 13th plate, R_s = 4 Ω/plate) (a) anode particle; (b) cathode particle.
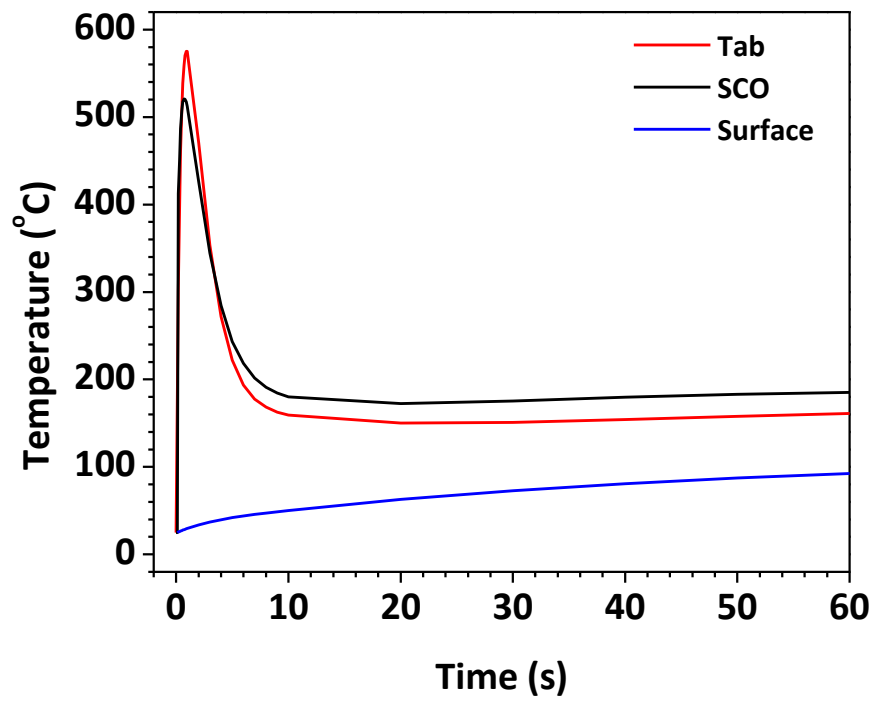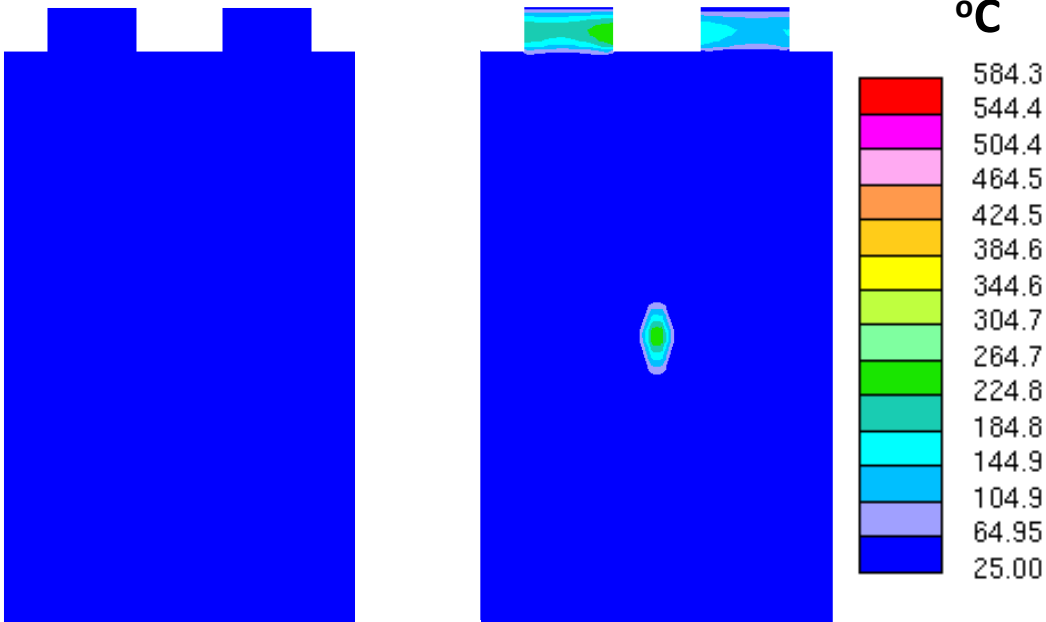
Figure 5-10: Temperature response (shorted plate = 13th plate, R_s = 5.2 mΩ/plate)

(a)

(b)

(c)

(d)
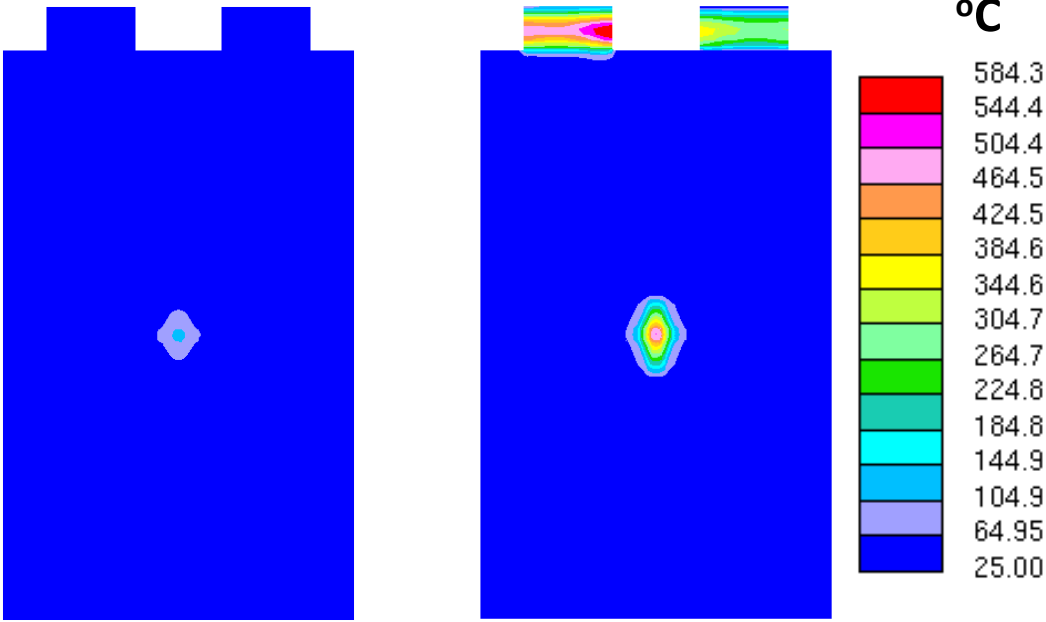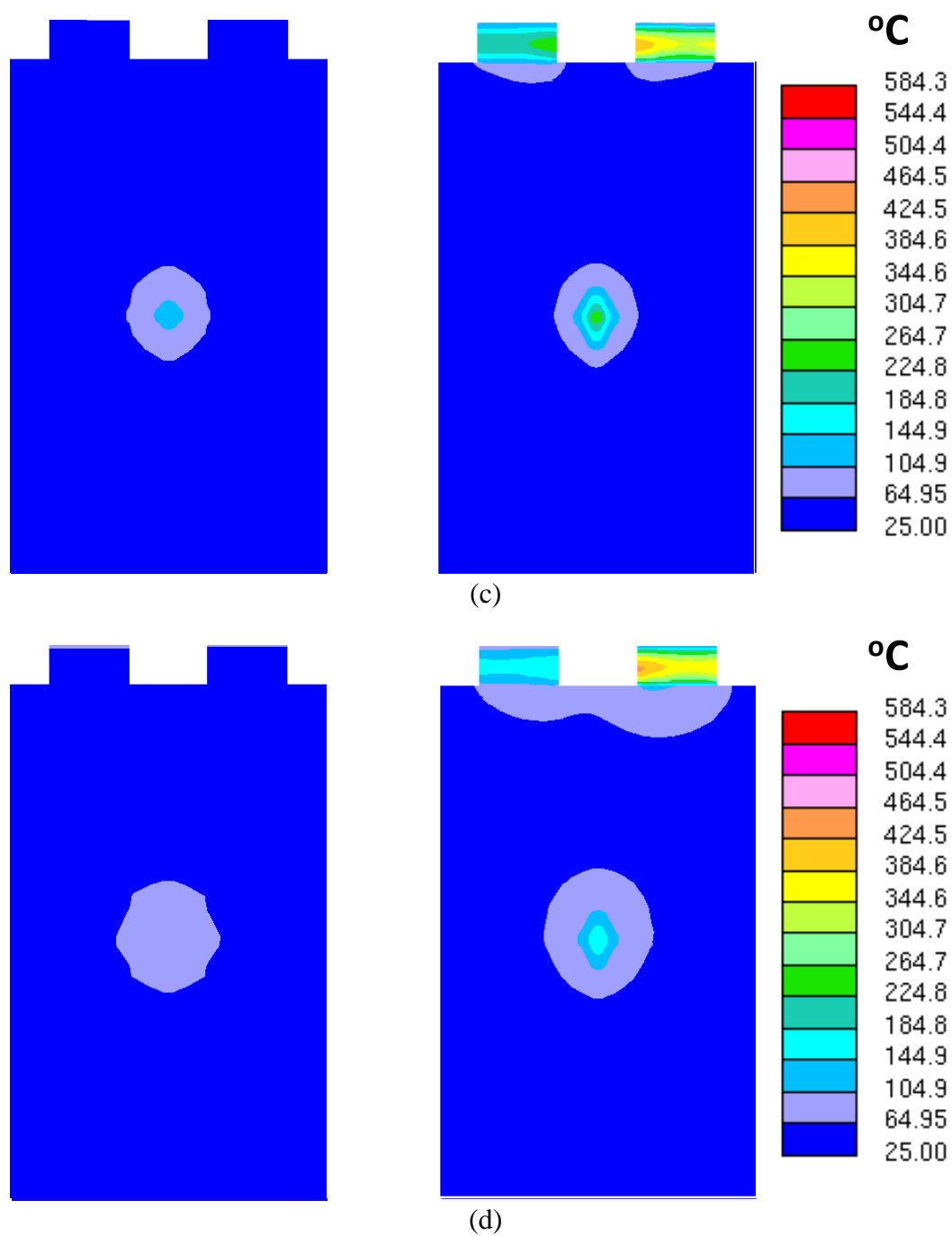
Figure 5-11: 2D temperature contour (shorted plate = 13th plate, R_s = 5.2 mΩ/plate, left: cell surface, right: cell center plane) (a) 0.1s; (b) 1s; (c) 5s; (d) 10s.
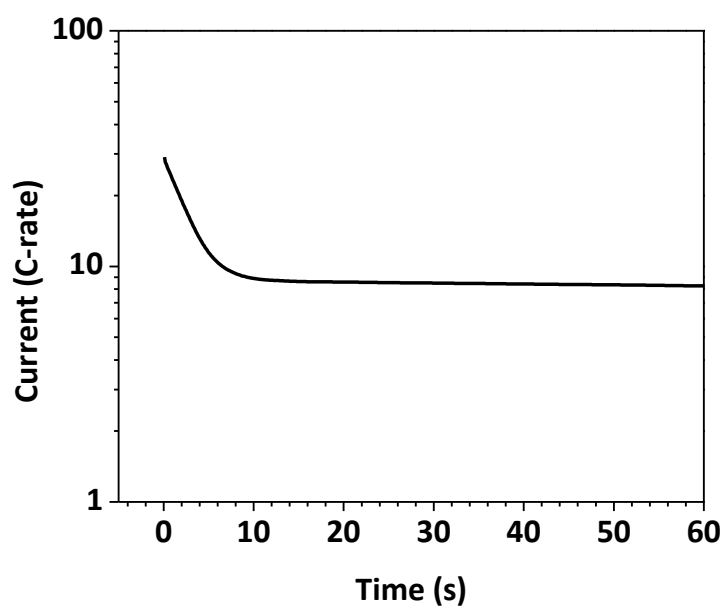
(a)
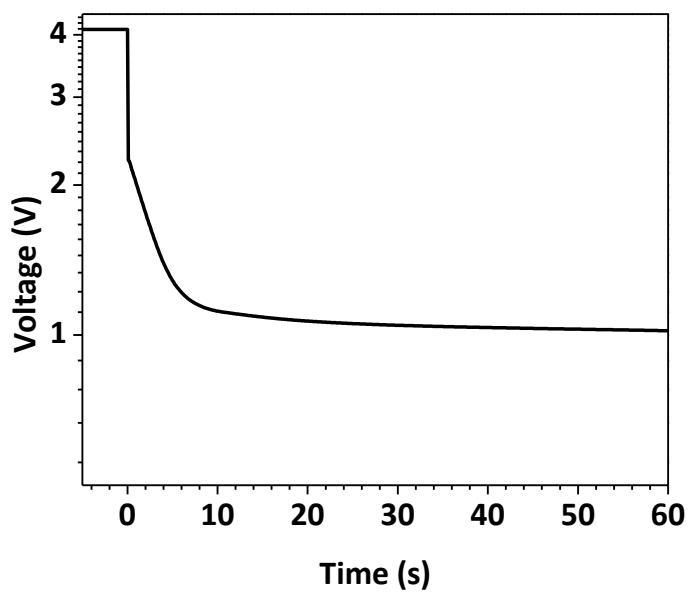
(b)

Figure 5-12: Current and voltage response (shorted plate = 13th plate, R$_s$ = 5.2 mΩ/plate) (a) current; (b) voltage.
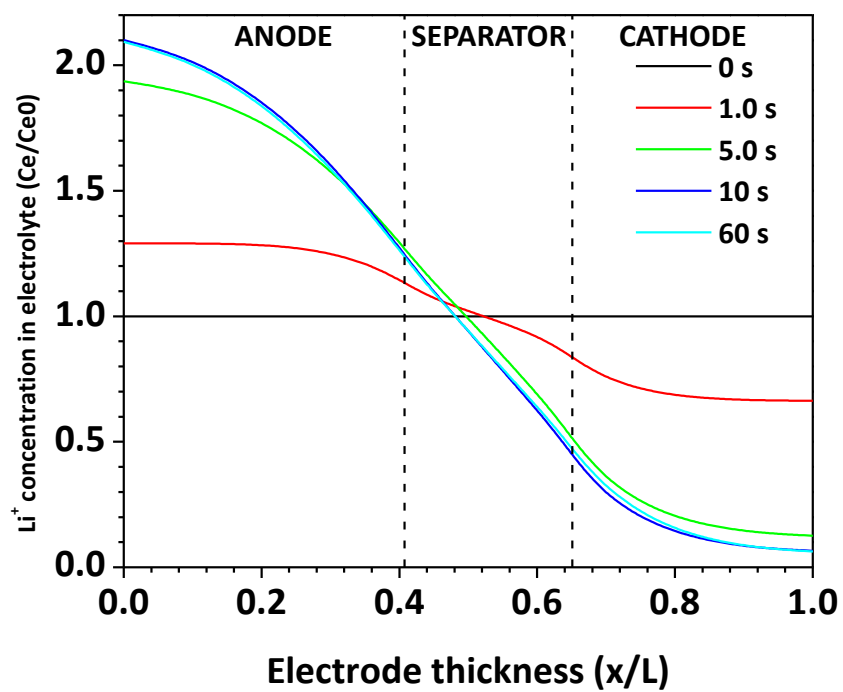
Figure 5-13: Li+ concentration in electrolyte (shorted plate = 13th plate, R_s = 5.2 mΩ/plate)
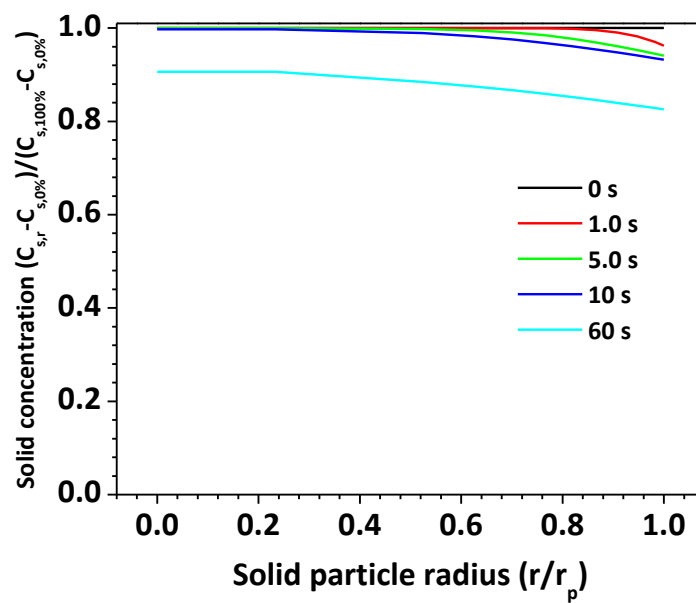
(a)
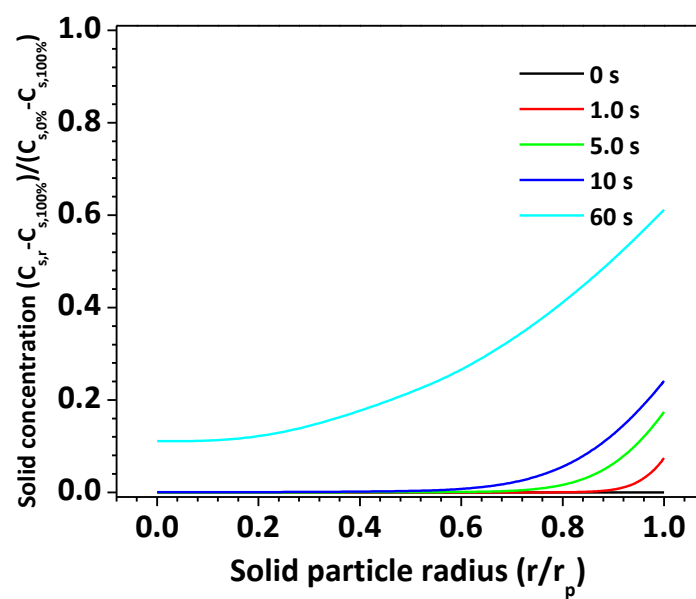
(b)

Figure 5-14: Li+ concentration in active material particles (shorted plate = 13th plate, R_s = 5.2 mΩ/plate) (a) anode particle; (b) cathode particle.
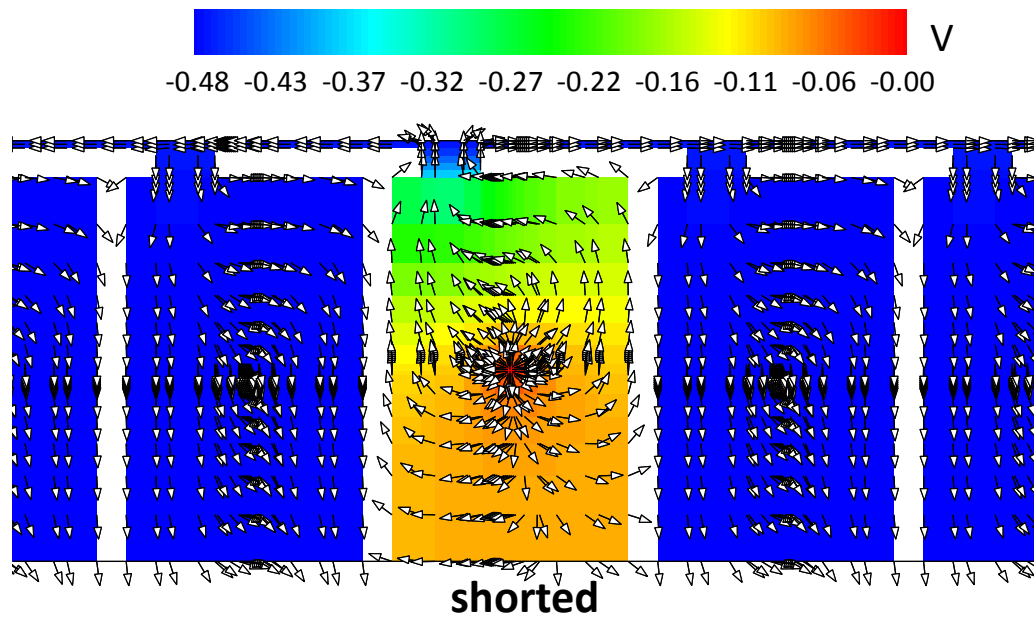
(a)
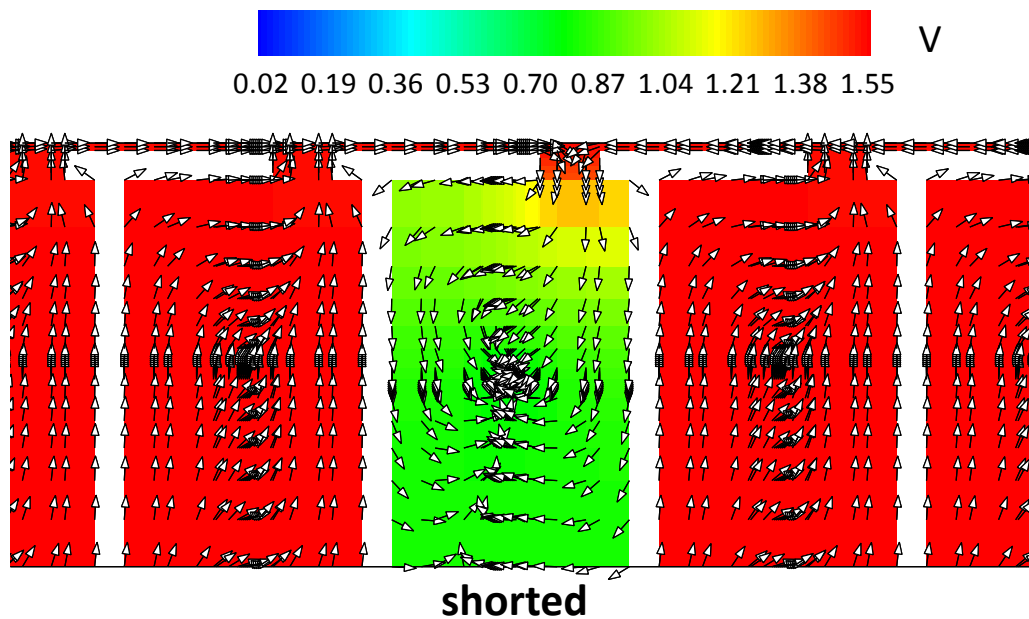
(b)

Figure 5-15: Solid potential and current flow vectors on the foils (shorted plate = 13th plate, R_s = 5.2 mΩ/plate) (a) Cu foil; (b) Al foil.

shorted

(a)
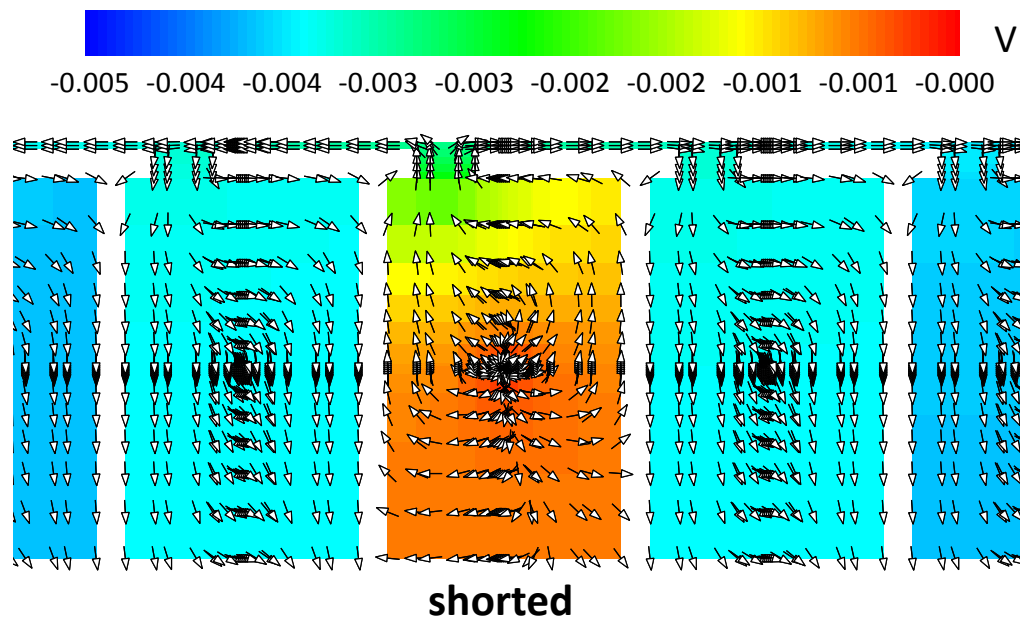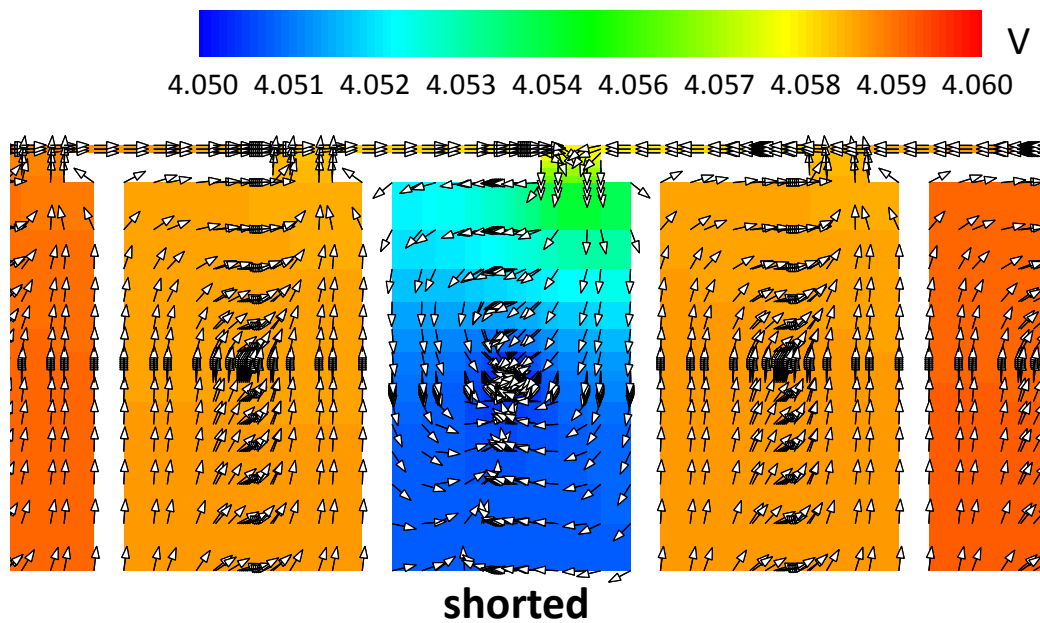
shorted

(b)

Figure 5-16: Solid potential and current flow vectors on the foils (shorted plate = 13th plate, R_s = 4 Ω/plate) (a) Cu foil; (b) Al foil.
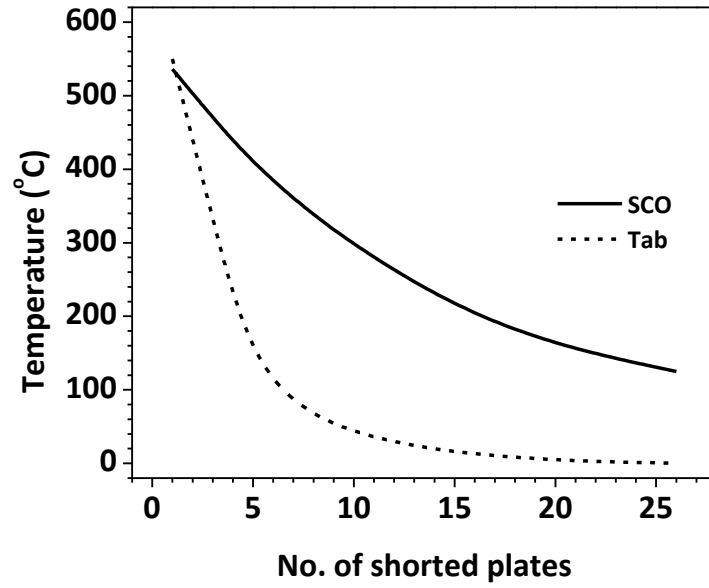
(a)
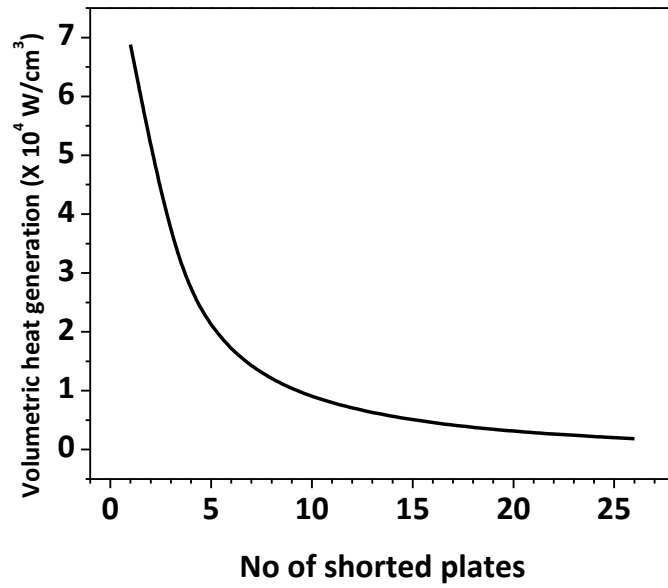
(b)

Figure 5-17: Effect of number of shorted plates (R_s = 5.2 mΩ/plate) (a) temperature rise of SCO and tab (b) volumetric heat generation on SCO.
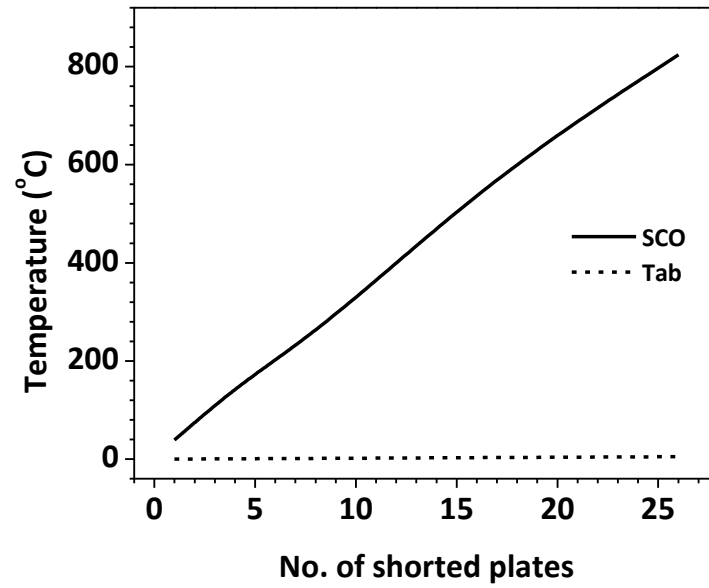
(a)
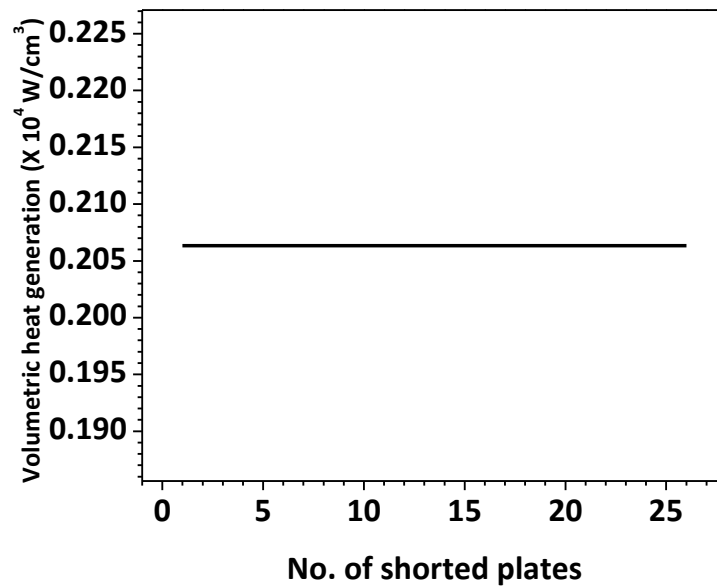
(b)

Figure 5-18: Effect of number of shorted plates (R_s = 4 Ω/plate) (a) temperature rise of SCO and tab (b) volumetric heat generation on SCO.

(a)
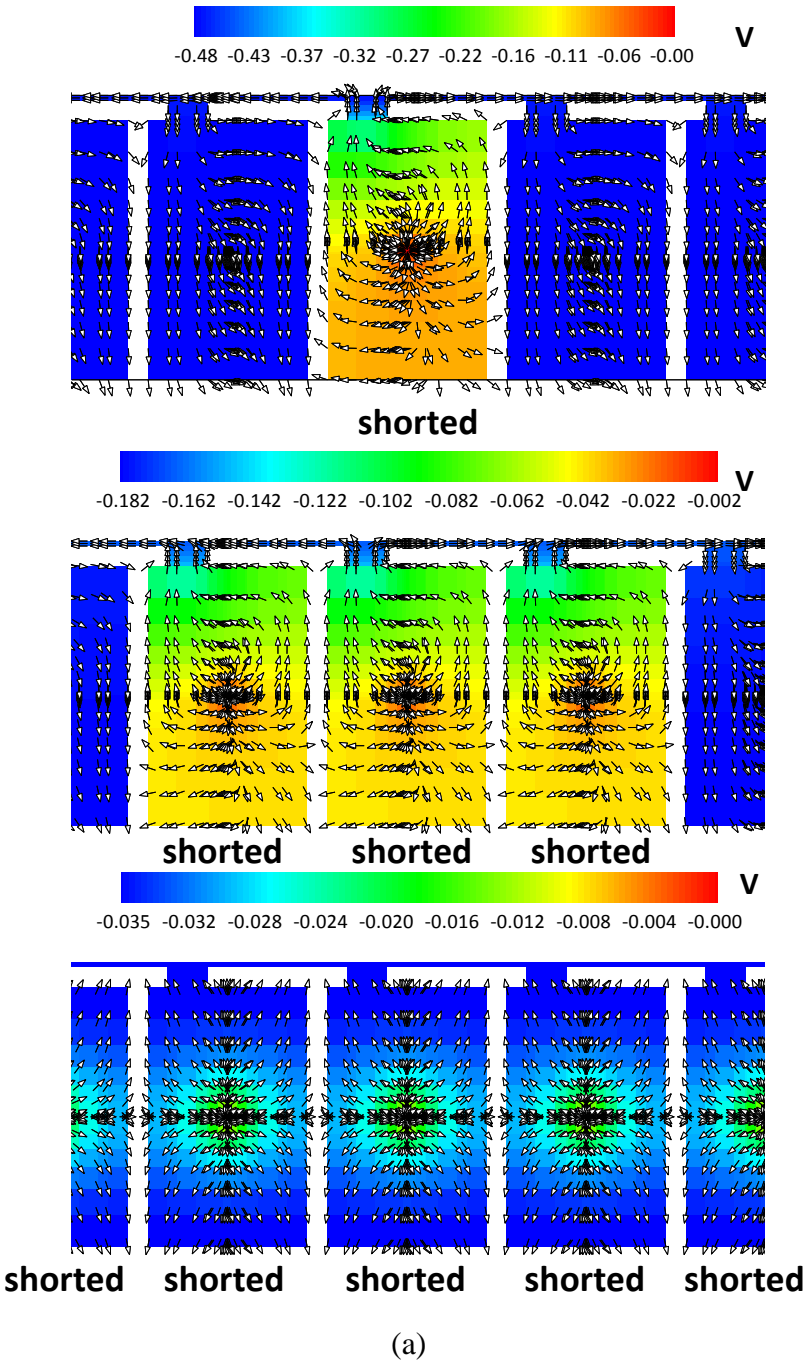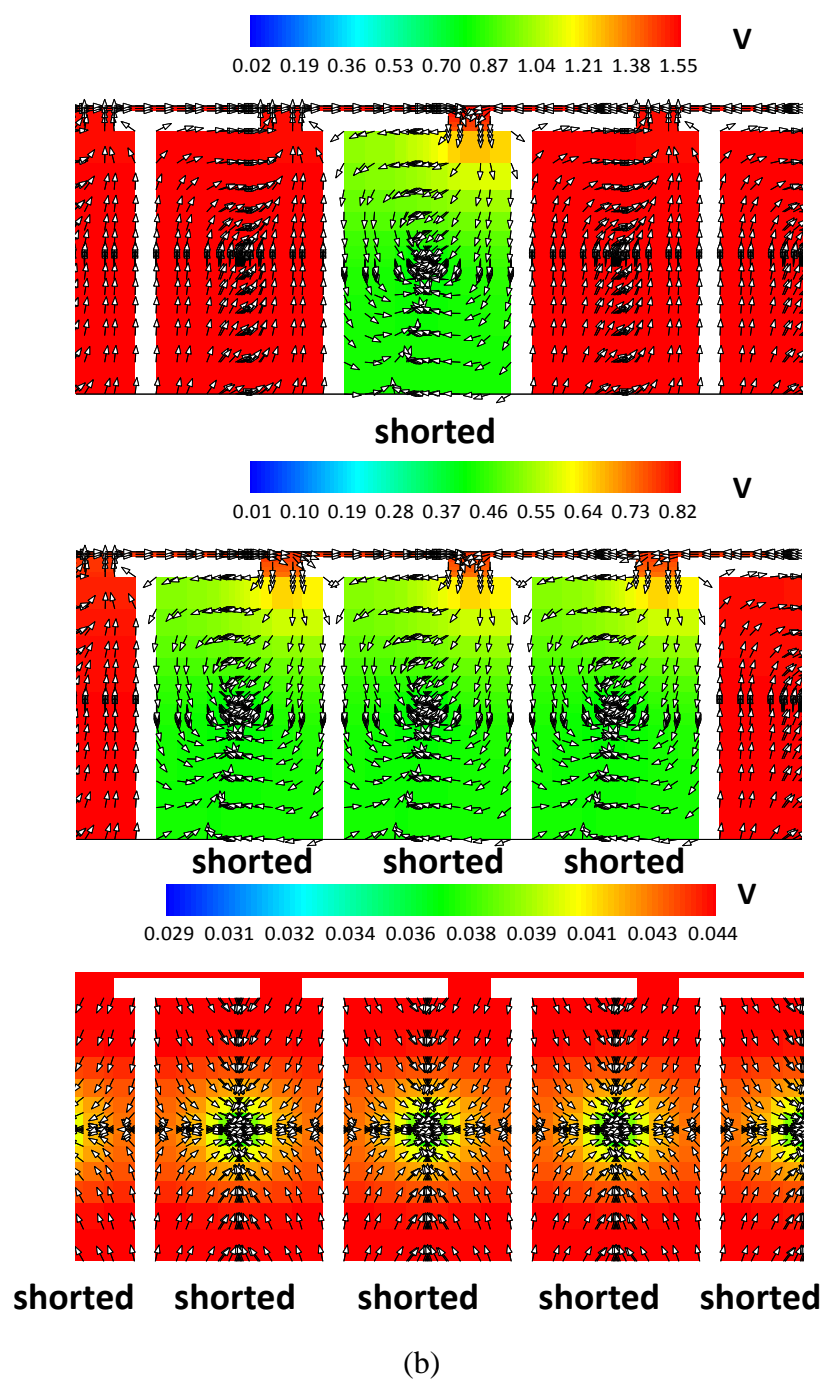
Figure 5-19: Solid potential and current flow vectors on the foils (R_s = 5.2 mΩ/plate) (a) Cu foil; (b) Al foil.

(a)

(b)

(c)

(d)
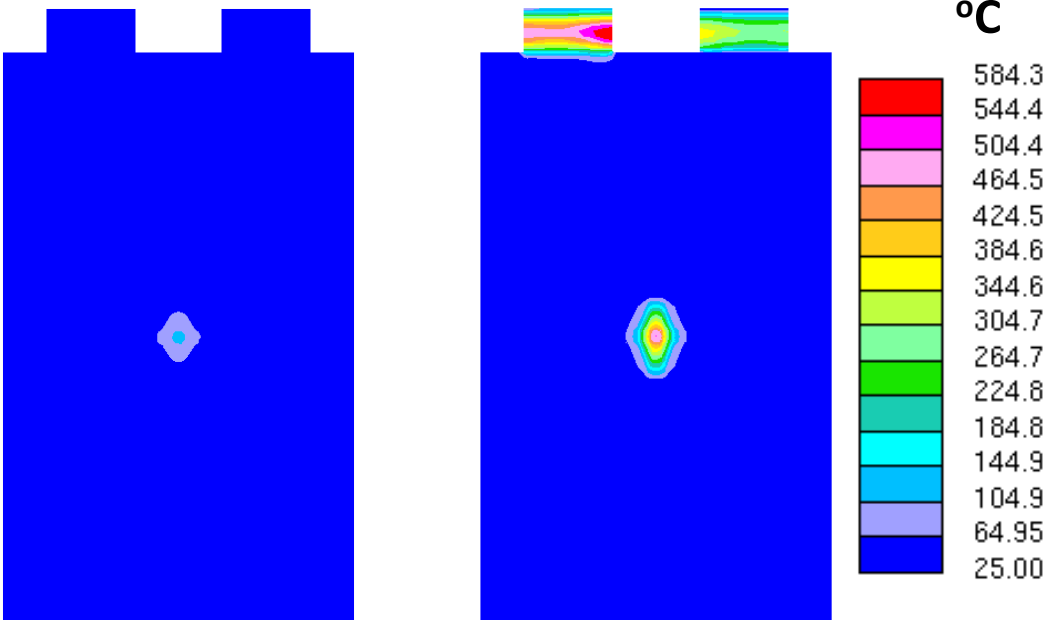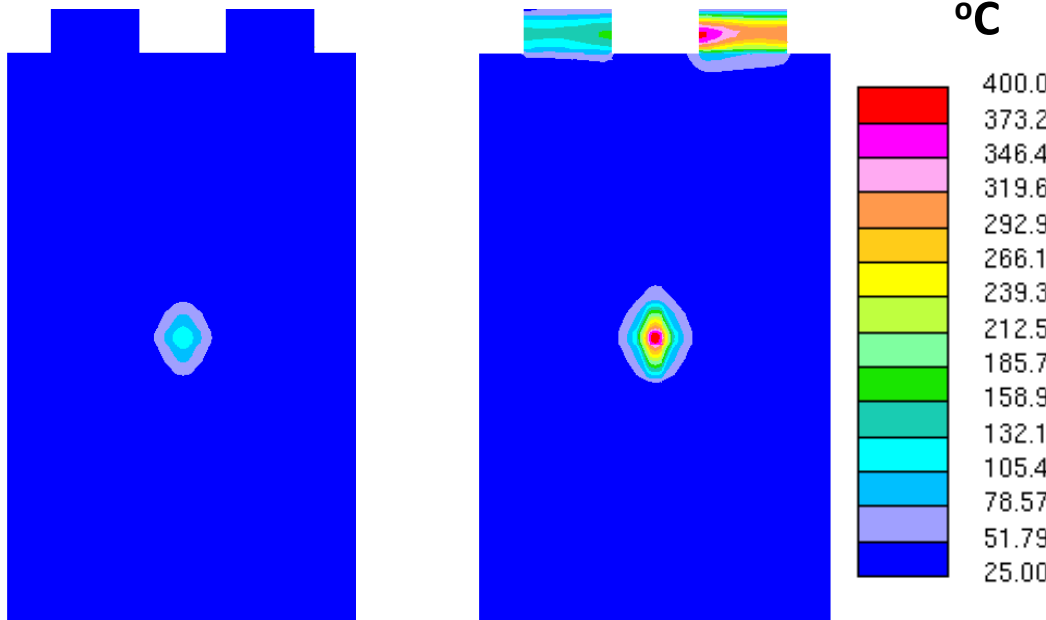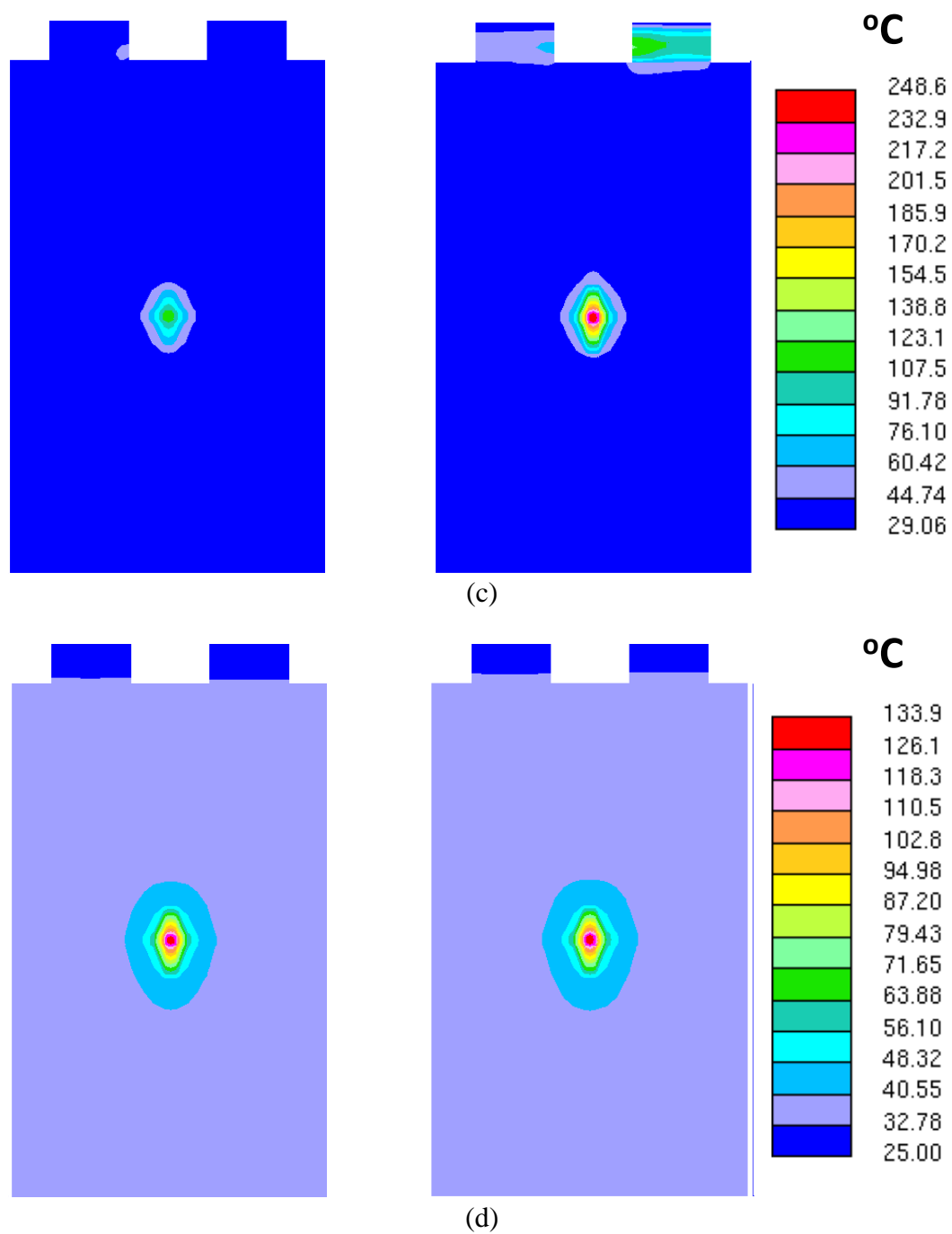
Figure 5-20: 2D temperature contour (R_s = 5.2 mΩ/plate, left: cell surface, right: cell center plane, t = 1 s) (a) 1 plate; (b) 5 plates; (c) 9 plates; (d) 26 plates

shorted

shorted **shorted** **shorted**

shorted **shorted** **shorted** **shorted** **shorted**

(a)
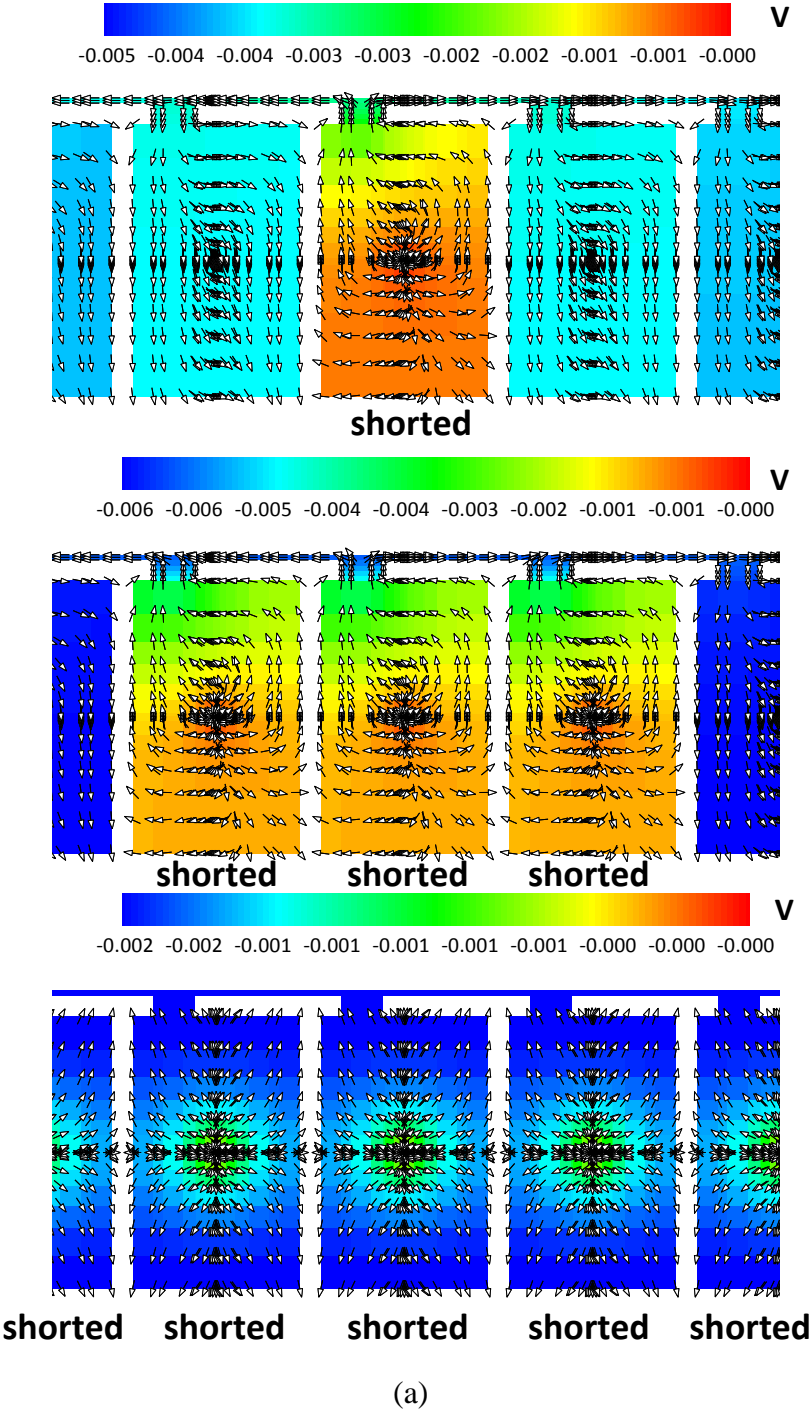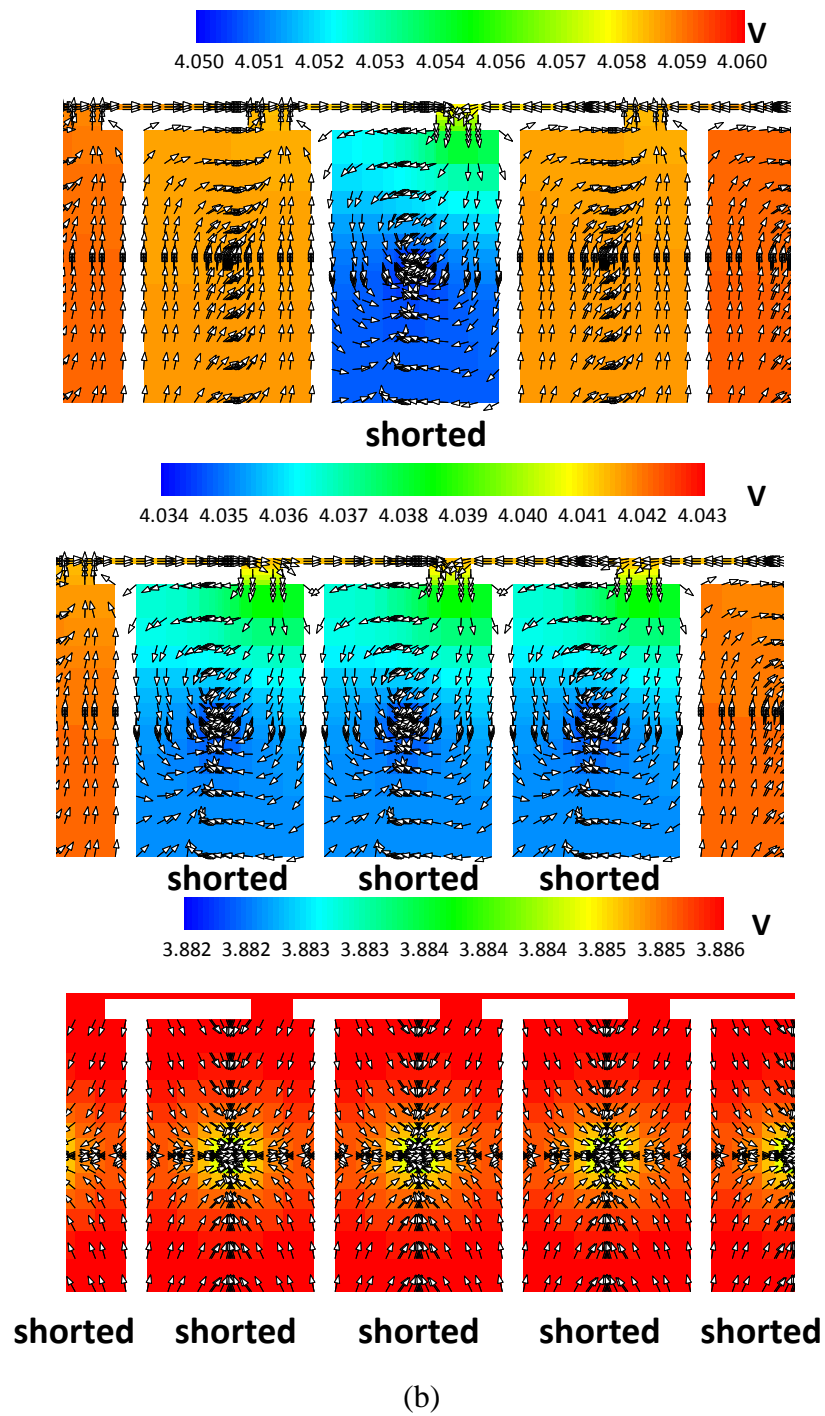
Figure 5-21: Solid potential and current flow vectors on the foils (R_s = 4 Ω/plate) (a) Cu foil; (b) Al foil.
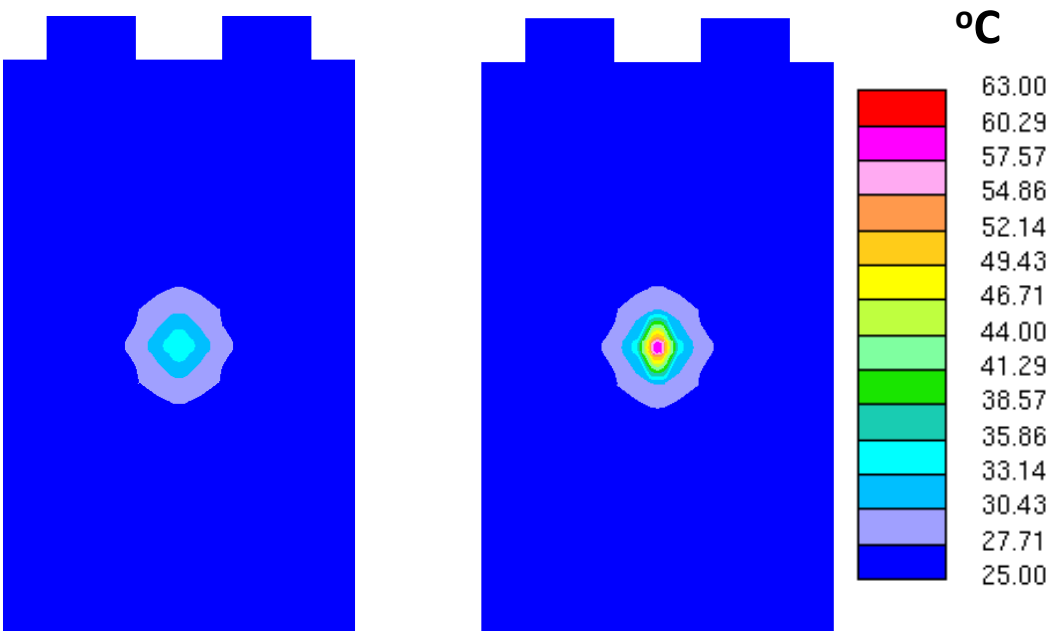
(a)
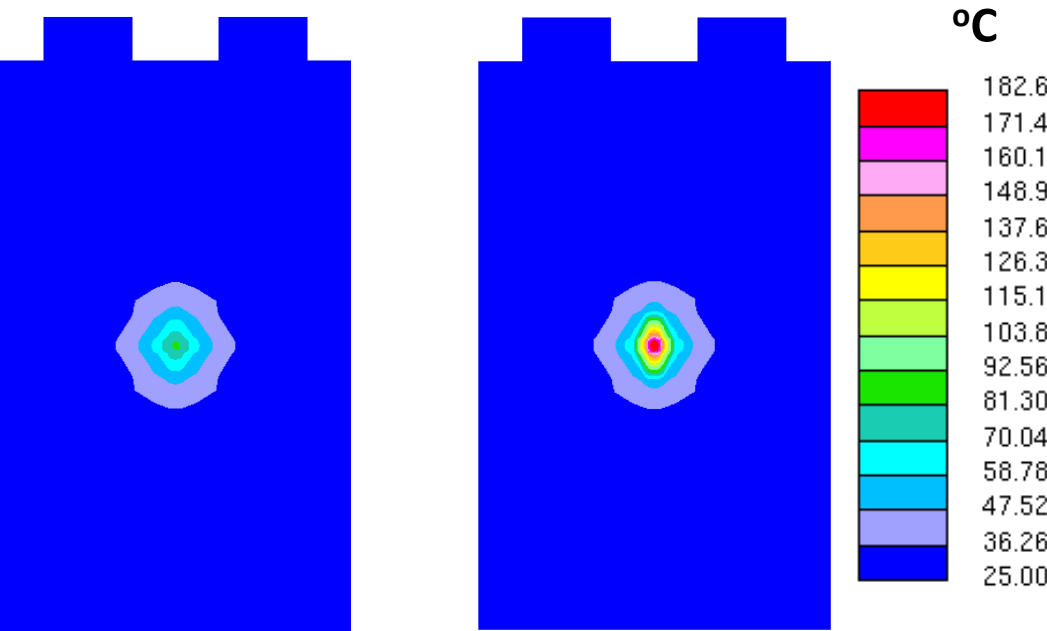
(b)
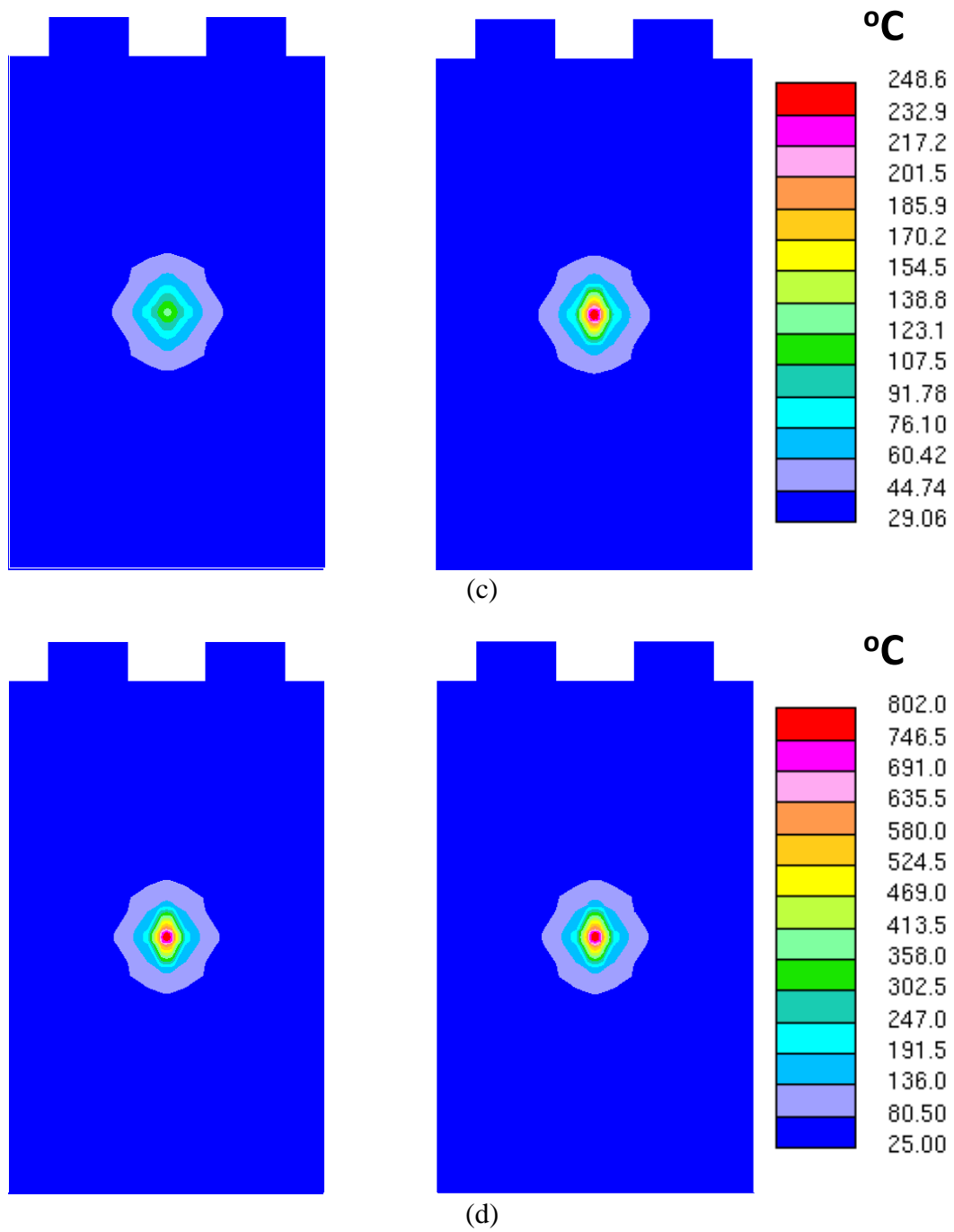
Figure 5-22: 2D temperature contour ($R_s = 4$ Ω/plate, left: cell surface, right: cell center plane, t = 10 s) (a) 1 plate; (b) 5 plates; (c) 9 plates; (d) 26 plates.

Chapter 6

Conclusion and future work

6.1 Conclusion

The present thesis documents a comprehensive study on the modeling of large-format Li-ion battery cells. Specific interest has been focused on using modeling tool to investigate performance and safety issues of large-format Li-ion cells.

In order to study the unique issues in large-format cells, a multidimensional, multiscale, and electrochemical-thermal coupled model is introduced in Chapter 2. The model is able to deal with the electrons transport in the long current collecting foils, multiple-tab configurations, and the coupling of electrochemical and thermal mechanisms, which are essential for studying large-format Li-ion cells. The general purpose battery model is also extended to simulate the safety events, specifically nail penetration and internal short-circuit processes of Li-ion cells.

Engineering optimization is imperative to boost performance of large-format Li-ion cells in order to achieve the full potential of existing battery materials. In Chapter 3, it is shown that for a large-format cell with spirally wound structure, significant performance loss is induced compared with the coin cell having the same active materials and electrode formulation. It is found that the performance loss results from the electrons transport through long current collectors, which not only causes large Ohmic resistance, but also creates non-uniform utilization of active materials. It is further shown that

utilization of multiple-tab design can mitigate the Ohmic loss, thereby significantly improving the cell performance.

Among various abusive conditions of Li-ion cells, internal short-circuit is the most dangerous one and has been the main cause for several high profile accidents involving Li-ion batteries in recent years. Nail penetration and crush test are widely used methods to emulate the internal short-circuits process in Li-ion cells. A common problem of the experimental methods is the poor reproducibility of the test results. The experimental observations also provide few insights into the fundamental mechanisms that govern the cell behavior during the nail penetration process. In Chapter 4 and 5, modeling effort is carried out to review the detailed internal electrochemical and thermal mechanisms of cell during internal short-circuit process.

In Chapter 4, nail penetration process of Li-ion cells is studied. The electrochemical and thermal behaviors of a Li-ion cell during nail penetration are simulated by the battery model. Comprehensive parametric studies are carried out. It is found that the shorting resistance, nail diameter and material properties have significant effect on the cell discharge behavior during nail penetration. The different discharge behaviors result in different heating modes of the cell. When the shorting resistance is small or nails with large diameter are used, global heating is caused, which makes the cell heated up uniformly. On the other hand, if the shorting resistance is large or using large diameter nails, the heating is localized in the vicinity of shorting spot. The present experimental methods are not able to precisely control the key parameters of nail penetration, which is the main reason for the irreproducibility of the experimental results.

Chapter 5 studies the internal short-circuit caused by a metal particle in Li-ion cells. The modeling result shows that, unlike the nail penetration process, tab heating becomes an important issue in internal short-circuit process. For large format Li-ion cell, it is necessary to monitor the tab temperature in order to detect the occurrence of internal short-circuit. The size of the metal particle also has a significant effect on the shorting behavior. When the metal particle size is small, only one or a few electrode plates are shorted, leading to non-uniform current distribution and significant tab heating. When the metal particle size is large enough to penetrate more electrode plates, the current distribution is more uniform, alleviating the tab heating.

6.2 Future work

The present work conducts modeling study of large-format Li-ion cells, for the first time, using multidimensional and multiscale electrochemical-thermal coupled models. Although a number of critical performance and safety issues have been addressed, there are many potential works that could be done in the future.

Li-ion cells suffer substantial energy and power loss operating at low temperatures. How the cell structure design would affect the low temperature performance of large-format Li-ion cells remains unknown. At low temperatures, the current density uniformity should have a more significant effect on the cell performance. The work of Chapter 3 can be extended to explore the tabs effect on cell performance at low temperatures.

The nail penetration and internal short-circuit process usually causes thermal runaway of Li-ion cells. In the present work, heat generation from the various exothermic reactions of battery materials that could lead to thermal runaway is ignored. The reason is largely due to that the detailed mechanisms of the exothermic reactions are not well understood by experimental studies. In the future, with the advances of experimental study on exothermic reactions, a more complete battery model should be developed incorporating the exothermic reaction mechanisms. The model can be used to more accurately study the safety event of Li-ion cells.

Bibliography

1. Linden, D. and T.B. Reddy, *Handbook of batteries.* New York, 2002.
2. Buiel, E. and J. Dahn, *Li-insertion in hard carbon anode materials for Li-ion batteries.* Electrochimica Acta, 1999. 45(1): p. 121-130.
3. Nazri, G.-A. and G. Pistoia, *Lithium batteries: science and technology*. 2004: Springer.
4. Takami, N., et al., *Electrochemical kinetics and safety of 2-volt class Li-ion battery system using lithium titanium oxide anode.* Journal of The Electrochemical Society, 2009. 156(2): p. A128-A132.
5. Li, J., Z. Tang, and Z. Zhang, *Preparation and novel lithium intercalation properties of titanium oxide nanotubes.* Electrochemical and Solid-State Letters, 2005. 8(6): p. A316-A319.
6. Chan, C.K., et al., *High-performance lithium battery anodes using silicon nanowires.* Nature nanotechnology, 2007. 3(1): p. 31-35.
7. Ellis, B.L., K.T. Lee, and L.F. Nazar, *Positive Electrode Materials for Li-Ion and Li-Batteries†.* Chemistry of Materials, 2010. 22(3): p. 691-714.
8. Nagaura, T. and K. Tozawa, *Lithium ion rechargeable battery.* Prog. Batteries Solar Cells, 1990. 9: p. 209.
9. Girishkumar, G., et al., *Lithium− air battery: Promise and challenges.* The Journal of Physical Chemistry Letters, 2010. 1(14): p. 2193-2203.
10. *Fire aboard empty 787 Dreamliner prompts investigation*. 2013; Available from: http://edition.cnn.com/2013/01/07/travel/dreamliner-fire/index.html.
11. *Top Japan airlines ground Boeing 787s after emergency*. 2013; Available from: http://www.bbc.co.uk/news/business-21038128.
12. Ostrower, J. *Microscopic 'Dendrites' a Focus in Boeing Dreamliner Probe - WSJ.com*. 2013; Available from: http://online.wsj.com/article/SB10001424127887324880504578298673566960476.html.
13. Associated, P. *Signs of runaway heat seen in Boeing 787 Dreamliner batteries*. 2013; Available from: http://www.foxnews.com/world/2013/02/05/signs-runaway-heat-seen-in-boeing-787-dreamliner-batteries/.
14. Doughty, D.H., *Li Ion Battery Abuse Tolerance Testing-An Overview.* Sandia National Laboratories, Präsentation auf der AQMD, 2006. 12.
15. Doughty, D.H. and A.A. Pesaran, *Vehicle Battery Safety Roadmap Guidance*. 2012, National Renewable Energy Laboratory.
16. Arora, P. and Z. Zhang, *Battery separators.* Chemical Reviews, 2004. 104(10): p. 4419-4462.
17. Richard, M. and J. Dahn, *Accelerating rate calorimetry study on the thermal stability of lithium intercalated graphite in electrolyte. I. Experimental.* Journal of The Electrochemical Society, 1999. 146(6): p. 2068-2077.

18. Richard, M. and J. Dahn, *Accelerating rate calorimetry study on the thermal stability of lithium intercalated graphite in electrolyte. II. Modeling the results and predicting differential scanning calorimeter curves.* Journal of The Electrochemical Society, 1999. 146(6): p. 2078-2084.

19. Hatchard, T., et al., *Thermal model of cylindrical and prismatic lithium-ion cells.* Journal of The Electrochemical Society, 2001. 148(7): p. A755-A761.

20. Roth, E.P., *Abuse Response of 18650 Li-Ion Cells with Different Cathodes Using EC: EMC/LiPF6 and EC: PC: DMC/LiPF6 Electrolytes.* ECS Transactions, 2008. 11(19): p. 19-41.

21. Tobishima, S.-i. and J.-i. Yamaki, *A consideration of lithium cell safety.* Journal of Power Sources, 1999. 81: p. 882-886.

22. Ozawa, K., *Lithium-ion rechargeable batteries with LiCoO< sub> 2</sub> and carbon electrodes: the LiCoO< sub> 2</sub>/C system.* Solid State Ionics, 1994. 69(3): p. 212-221.

23. Wu, M.-S., et al., *Correlation between electrochemical characteristics and thermal stability of advanced lithium-ion batteries in abuse tests—short-circuit tests.* Electrochimica Acta, 2004. 49(11): p. 1803-1812.

24. Tobishima, S.-i., et al., *Lithium ion cell safety.* Journal of Power Sources, 2000. 90(2): p. 188-195.

25. Nguyen, J. and C. Taylor. *Safety performance for phosphate based large format lithium-ion battery*. in *Telecommunications Energy Conference, 2004. INTELEC 2004. 26th Annual International*. 2004: IEEE.

26. Maleki, H. and J.N. Howard, *Internal short circuit in Li-ion cells.* Journal of Power Sources, 2009. 191(2): p. 568-574.

27. Ichimura, M. *The safety characteristics of lithium-ion batteries for mobile phones and the nail penetration test*. in *Telecommunications Energy Conference, 2007. INTELEC 2007. 29th International*. 2007: IEEE.

28. Santhanagopalan, S., P. Ramadass, and J.Z. Zhang, *Analysis of internal short-circuit in a lithium ion cell.* Journal of Power Sources, 2009. 194(1): p. 550-557.

29. Thele, M., et al., *Development of a voltage-behavior model for NiMH batteries using an impedance-based modeling concept.* Journal of Power Sources, 2008. 175(1): p. 635-643.

30. Lee, S., et al., *State-of-charge and capacity estimation of lithium-ion battery using a new open-circuit voltage versus state-of-charge.* Journal of Power Sources, 2008. 185(2): p. 1367-1373.

31. Johnson, V., *Battery performance models in ADVISOR.* Journal of Power Sources, 2002. 110(2): p. 321-329.

32. He, H., R. Xiong, and J. Fan, *Evaluation of lithium-ion battery equivalent circuit models for state of charge estimation by an experimental approach.* Energies, 2011. 4(4): p. 582-598.

33. Fuller, T.F., M. Doyle, and J. Newman, *Relaxation Phenomena in Lithium‐Ion‐Insertion Cells.* Journal of The Electrochemical Society, 1994. 141(4): p. 982-990.

34. Doyle, M., T.F. Fuller, and J. Newman, *Modeling of galvanostatic charge and discharge of the lithium/polymer/insertion cell.* Journal of The Electrochemical Society, 1993. 140(6): p. 1526-1533.

35. Doyle, M., et al., *Comparison of modeling predictions with experimental data from plastic lithium ion cells.* Journal of The Electrochemical Society, 1996. 143(6): p. 1890-1903.

36. Arora, P., et al., *Comparison between computer simulations and experimental data for high-rate discharges of plastic lithium-ion batteries.* Journal of Power Sources, 2000. 88(2): p. 219-231.

37. Botte, G.G., V.R. Subramanian, and R.E. White, *Mathematical modeling of secondary lithium batteries.* Electrochimica Acta, 2000. 45(15): p. 2595-2609.

38. Gomadam, P.M., et al., *Mathematical modeling of lithium-ion and nickel battery systems.* Journal of Power Sources, 2002. 110(2): p. 267-284.

39. Ning, G., R.E. White, and B.N. Popov, *A generalized cycle life model of rechargeable Li-ion batteries.* Electrochimica Acta, 2006. 51(10): p. 2012-2022.

40. Ramadass, P., et al., *Mathematical modeling of the capacity fade of Li-ion cells.* Journal of Power Sources, 2003. 123(2): p. 230-240.

41. Ramadass, P., et al., *Development of first principles capacity fade model for Li-ion cells.* Journal of The Electrochemical Society, 2004. 151(2): p. A196-A203.

42. Newman, J., et al., *Modeling of lithium-ion batteries.* Journal of Power Sources, 2003. 119: p. 838-843.

43. Al Hallaj, S., et al., *Thermal modeling and design considerations of lithium-ion batteries.* Journal of Power Sources, 1999. 83(1): p. 1-8.

44. Chen, S.-C., Y.-Y. Wang, and C.-C. Wan, *Thermal analysis of spirally wound lithium batteries.* Journal of The Electrochemical Society, 2006. 153(4): p. A637-A648.

45. Chen, Y. and J.W. Evans, *Heat Transfer Phenomena in Lithium/Polymer-Electrolyte Batteries for Electric Vehicle Application.* Journal of The Electrochemical Society, 1993. 140(7): p. 1833-1838.

46. Chen, Y. and J.W. Evans, *Thermal analysis of lithium polymer electrolyte batteries by a two dimensional model—thermal behaviour and design optimization.* Electrochimica Acta, 1994. 39(4): p. 517-526.

47. Chen, Y. and J.W. Evans, *Three-Dimensional Thermal Modeling of Lithium-Polymer Batteries under Galvanostatic Discharge and Dynamic Power Profile.* Journal of The Electrochemical Society, 1994. 141(11): p. 2947-2955.

48. Chen, Y. and J.W. Evans, *Thermal Analysis of Lithium-Ion Batteries.* Journal of The Electrochemical Society, 1996. 143(9): p. 2708-2712.

49. Chen, S., C. Wan, and Y. Wang, *Thermal analysis of lithium-ion batteries.* Journal of Power Sources, 2005. 140(1): p. 111-124.

50. Onda, K., et al., *Thermal behavior of small lithium-ion battery during rapid charge and discharge cycles.* Journal of Power Sources, 2006. 158(1): p. 535-542.

51. Pals, C.R. and J. Newman, *Thermal Modeling of the Lithium/Polymer Battery: I. Discharge Behavior of a Single Cell.* Journal of The Electrochemical Society, 1995. 142(10): p. 3274-3281.

52. Pals, C.R. and J. Newman, *Thermal modeling of the lithium/polymer battery II. Temperature profiles in a cell stack.* Journal of The Electrochemical Society, 1995. 142(10): p. 3282-3288.

53. Verbrugge, M.W., *Three‑dimensionai temperature and current distribution in a battery module.* Aiche Journal, 1995. 41(6): p. 1550-1562.

54. Botte, G.G., B.A. Johnson, and R.E. White, *Influence of Some Design Variables on the Thermal Behavior of a Lithium‑Ion Cell.* Journal of The Electrochemical Society, 1999. 146(3): p. 914-923.

55. Song, L. and J.W. Evans, *Electrochemical‑Thermal Model of Lithium Polymer Batteries.* Journal of The Electrochemical Society, 2000. 147(6): p. 2086-2095.

56. Srinivasan, V. and C. Wang, *Analysis of electrochemical and thermal behavior of Li-ion cells.* Journal of The Electrochemical Society, 2003. 150(1): p. A98-A106.

57. Thomas, K.E. and J. Newman, *Thermal modeling of porous insertion electrodes.* Journal of The Electrochemical Society, 2003. 150(2): p. A176-A192.

58. Smith, K. and C.-Y. Wang, *Power and thermal characterization of a lithium-ion battery pack for hybrid-electric vehicles.* Journal of Power Sources, 2006. 160(1): p. 662-673.

59. Kumaresan, K., G. Sikha, and R.E. White, *Thermal model for a Li-ion cell.* Journal of The Electrochemical Society, 2008. 155(2): p. A164-A171.

60. Fang, W., O.J. Kwon, and C.Y. Wang, *Electrochemical–thermal modeling of automotive Li‑ion batteries and experimental validation using a three‑electrode cell.* International Journal of Energy Research, 2010. 34(2): p. 107-115.

61. Gerver, R.E. and J.P. Meyers, *Three-dimensional modeling of electrochemical performance and heat generation of lithium-ion batteries in tabbed planar configurations.* Journal of The Electrochemical Society, 2011. 158(7): p. A835-A843.

62. Guo, M. and R.E. White, *A distributed thermal model for a Li-ion electrode plate pair.* Journal of Power Sources, 2012.

63. Guo, M., G.-H. Kim, and R.E. White, *A three-dimensional multi-physics model for a Li-ion battery.* Journal of Power Sources, 2013.

64. Kim, G.-H., et al., *Multi-Domain Modeling of Lithium-Ion Batteries Encompassing Multi-Physics in Varied Length Scales.* Journal of The Electrochemical Society, 2011. 158(8): p. A955-A969.

65. Luo, G. and C.-Y. Wang, *A Multidimensional, Electrochemical-Thermal Coupled Lithium-Ion Battery Model.* Lithium-ion Batteries: Advanced Materials and Technologies, 2012: p. 303.

66. Spotnitz, R. and J. Franklin, *Abuse behavior of high-power, lithium-ion cells.* Journal of Power Sources, 2003. 113(1): p. 81-100.

67. Spotnitz, R.M., et al., *Simulation of abuse tolerance of lithium-ion battery packs.* Journal of Power Sources, 2007. 163(2): p. 1080-1086.

68. Kim, G.-H., A. Pesaran, and R. Spotnitz, *A three-dimensional thermal abuse model for lithium-ion cells.* Journal of Power Sources, 2007. 170(2): p. 476-489.

69. Yamauchi, T., et al., *Development of a simulator for both property and safety of a lithium secondary battery.* Journal of Power Sources, 2004. 136(1): p. 99-107.

70.   Gu, W. and C. Wang, *Thermal-Electrochemical Modeling of Battery Systems.* Journal of The Electrochemical Society, 2000. 147(8): p. 2910-2922.

71.   Verbrugge, M.W. and B.J. Koch, *Electrochemical analysis of lithiated graphite anodes.* Journal of The Electrochemical Society, 2003. 150(3): p. A374-A384.

72.   Yabuuchi, N., Y. Makimura, and T. Ohzuku, *Solid-State Chemistry and Electrochemistry of LiCo1/3Ni1/3Mn1/3O2 for Advanced Lithium-Ion Batteries III. Rechargeable Capacity and Cycleability.* Journal of The Electrochemical Society, 2007. 154(4): p. A314-A321.

73.   Valøen, L.O. and J.N. Reimers, *Transport properties of LiPF6-based Li-ion battery electrolytes.* Journal of The Electrochemical Society, 2005. 152(5): p. A882-A891.

74.   Reynier, Y.F., R. Yazami, and B. Fultz, *Thermodynamics of lithium intercalation into graphites and disordered carbons.* Journal of The Electrochemical Society, 2004. 151(3): p. A422-A426.

75.   Lu, W., et al., *In Situ Thermal Study of Li1+x [Ni1/3Co1/3Mn1/3] 1−x O2 Using Isothermal Micro-clorimetric Techniques.* Journal of The Electrochemical Society, 2006. 153(11): p. A2147-A2151.

76.   Zhang, G., et al., *In-Situ Measurement of Current Distribution in a Li-Ion Cell.* Journal of The Electrochemical Society, 2013. 160(4): p. A610-A615.

77.   Guangsheng Zhang, C.E.S., Chao-Yang Wang, Christopher D. Rahn, *Effects of Non-uniform Current Distribution on Energy Density of Li-ion Cells.* Journal of The Electrochemical Society, 2013: p. accepted for publication.

78.   Dinger, A., et al., *Batteries for electric cars: Challenges, opportunities, and the outlook to 2020.* Boston Consulting Group, 2010.

79.   Doughty, D.H., *SAE J2464 "EV & HEV Rechargeable Energy Storage System (RESS) Safety and Abuse Testing Procedure"*, in *SAE Technical Paper 2010-01-1077*. 2010.

80.   Sawlsville, J., *Battery safety : a systematic study of battery performance under extreme conditions* in *Mechanical Engineering*. 2013, The Pennsylvania State University: University Park.

81.   Edwards, A., *Abuse testing of lithium ion cells : internal short circuit, accelerated rate calorimetry and nail penetration in large cells (1 -20 Ah)*, in *Battery safety 2011*. 2011.

82.   Eom, S.-W., et al., *Life prediction and reliability assessment of lithium secondary batteries.* Journal of Power Sources, 2007. 174(2): p. 954-958.

83.   Orendorff, C.J., E.P. Roth, and G. Nagasubramanian, *Experimental triggers for internal short circuits in lithium-ion cells.* Journal of Power Sources, 2011. 196(15): p. 6554-6558.

VITA

EDUCATION

Aug. 2008 – May. 2014	THE PENNSYLVANIA STATE UNIVERSITY
	Mechanical Engineering, Ph.D.
Sep. 2005 – Jul. 2008	XI'AN JIAOTONG UNIVERSITY
	Fluid Machinery Engineering, M.S.
Sep. 2005 – Jul. 2008	XI'AN JIAOTONG UNIVERSITY
	Thermal and Power Engineering, B.S.

RESEARCH AND WORK EXPERIENCE

Sep. 2013 – Dec. 2013	EC POWER LLC
	Intern for CFD Application Engineer
Jan. 2009 – Dec. 2013	ELECTROCHEMICAL ENGINE CENTER,
	THE PENNSYLVANIA STATE UNIVERSITY
	Research Assistant
Aug. 2008 – Dec. 2008	DEPARTMENT OF MECHANICAL ENGINEERING,
	THE PENNSYLVANIA STATE UNIVERSITY
	Teaching Assistant
Sep. 2005 – Jul. 2008	NATIONAL FLUID MACHINE AND COMPRESSOR RESEARCH CENTER,
	XI'AN JIAOTONG UNIVERSITY
	Research Assistant